Structure-function study on FIP200 reveals mechanistic insights into selective autophagy

Inaugural-Dissertation

to obtain the academic degree

Doctor rerum naturalium (Dr. rer. nat.)

submitted to the Department of Biology, Chemistry and Pharmacy

of Freie Universität Berlin

by

Marie Witt

2019

Examiners: Prof. Dr. Oliver Daumke
Prof. Dr. Udo Heinemann

Date of defense: August 8th, 2019

This thesis has been completed from October 2014 through March 2019 under the supervision of Oliver Daumke in the department of structural biology at the Max Delbrück Center in Berlin, Germany.

Publication

Parts of this thesis have been published online in *Molecular Cell* on March 7, 2019:

"FIP200 Claw domain binding to p62 promotes autophagosome formation at ubiquitin condensates."

Eleonora Turco*, Marie Witt*, Christine Abert*, Tobias Bock-Bierbaum*, Ming-Yuan Su*, Riccardo Trapannone, Martin Sztacho, Alberto Danieli, Xiaoshan Shi, Gabriele Zaffagnini, Annamaria Gamper, Martina Schuschnig, Dorotea Fracchiolla, Daniel Bernklau, Julia Romanov, Markus Hartl, James H. Hurley#, Oliver Daumke#, Sascha Martens#

* equal contribution

senior authors

Coordinates and diffraction data have been deposited in the Protein Data Bank (PDB) with accession code 6GMA.

Table of Contents

I. List of Figures XI

II. List of Tables XIII

III. Abstract / Zusammenfassung 1

1. Introduction 5

1.1 General principles of autophagy 5

1.2 Autophagy and disease 6

1.3 The autophagy core machinery 7

1.4 Selective autophagy 11

1.4.1 Cargo recognition 12

1.4.2 The LC3-interacting region (LIR) motif 13

1.4.3 The role of cargo receptor p62 in autophagy 15

1.5 Selective autophagy initiation in yeast 17

1.6 FIP200 - the counterpart of yeast Atg11 and Atg17 18

1.7 Direct interaction of FIP200 C-terminal region (CTR) and p62 22

2. Scope of this thesis 25

3. Materials and methods 27

3.1 Materials 27

3.1.1 Chemicals 27

3.1.2 Instruments 27

3.1.3 Enzymes 27

3.1.4 Kits 28

3.1.5 Plasmids 28

3.1.6 Bacteria Strains 28

3.1.7 Media and antibiotics 28

3.1.8 Buffers and solutions 29

3.1.9 Antibodies 30

3.1.10 Crystallization screens 30

3.1.11 Software and algorithms 31

3.2 Molecular biology methods 32

3.2.1 Agarose gel electrophoresis 32

3.2.2 DNA purification 32
3.2.3 Polymerase chain reaction (PCR) 32
3.2.4 Restriction digest 32
3.2.5 Ligation 32
3.2.6 Preparation of chemically competent *E. coli* cells 33
3.2.7 Transformation of chemically competent *E. coli* cells 33
3.2.8 Bacteria Storage 33
3.2.9 Site-directed mutagenesis 33
3.2.10 DNA sequencing 33
3.2.11 Constructs 34
3.3 Biochemical methods 34
3.3.1 Sequence alignment 34
3.3.2 Sodium dodecyl sulfate polyacrylamide gel electrophoresis (SDS-PAGE) 34
3.3.3 Protein expression 34
3.3.4 Purification of His_6-tagged proteins 34
3.3.5 Purification of GST fusion proteins 35
3.3.6 Expression and purification of seleno-L-methionine labelled protein for crystallization 35
3.3.7 Determination of protein concentration 36
3.3.8 Right-angle light scattering 36
3.3.9 Isothermal titration calorimetry (ITC) 36
3.3.10 Surface plasmon resonance spectroscopy (SPR) 36
3.3.11 Liposome preparation 37
3.3.12 Liposome co-sedimentation assay 37
3.3.13 Peptide array 38
3.3.14 Microscopy-based protein-protein interaction assays 38
3.3.15 p62 aggregation assay 39
3.4 Protein crystallization and structure determination 39
3.4.1 Crystallization of FIP200 CTR 39
3.4.2 Data collection and processing 40
3.4.3 Phase determination and refinement 40
3.4.4 Structure analysis and figure preparation 40

3.5 Cell biology methods 41
3.5.1 Pull-downs from HeLa and HAP1 cell lysates 41
3.5.2 Co-immunoprecipitation from HeLa cells 42
3.5.3 Generation of HeLa FIP200ΔClaw cell line 42
3.5.4 Immunocytochemistry 42
4. Results 45
4.1 Protein expression and purification 45
4.1.1 Expression and purification of FIP200 CTR 45
4.1.2 Expression and purification of GST-p62 FIR variants 46
4.2 Crystallization and structure determination of FIP200 CTR 46
4.2.1 Crystallization of FIP200 CTR 46
4.2.2 Data collection and phasing 48
4.2.3 Model building and refinement 50
4.3 The crystal structure of FIP200-CTR 52
4.3.1 Overall structure of FIP200 CTR 52
4.3.2 FIP200 CTR assembly in the crystal lattice 53
4.3.3 FIP200 CTR dimerization is mediated via a conserved and hydrophobic interface 55
4.4 The FIP200 Claw domain adopts an oligonucleotide/ oligosaccharide binding fold 56
4.5 Structure-guided identification of a p62 binding site in the FIP200 Claw domain 59
4.6 Affinity determination of FIP200 CTR and p62 FIR 62
4.6.1 Isothermal titration calorimetry (ITC) 62
4.6.2 Surface plasmon resonance spectroscopy (SPR) 63
4.7 FIP200 interacts with p62 via the Claw domain pocket *in vivo* 66
4.8 FIP200 CTR binds to liposomes through its p62 binding pocket 67
4.9 Towards the structure of a FIP200 - p62 complex 70
4.9.1 Crystallization attempts of FIP200 CTR - p62 complex 70
4.9.2 Identification of key interaction residues by a peptide SPOT array 71
5. Discussion 75
5.1 Physiological relevance of the FIP200 CTR crystal structure 75

5.2 Functional versatility of the OB-fold ... 77
5.3 FIP200 Claw pocket as a binding interface for phosphorylated receptors ... 78
5.4 Interaction of FIP200 with other cargo receptors ... 81
5.5 Regulatory role of receptor oligomerization ... 82
5.6 Structural model of full-length FIP200 suggests role as a tethering factor ... 84
5.6.1 Developing a model for full-length FIP200 ... 84
5.6.2 FIP200 - a membrane tethering factor? ... 86
5.7 Mechanism for FIP200-mediated selective autophagy cargo sequestration ... 88
5.8 Concluding remarks ... 89
6. References ... 91
IV. Appendix ... 105
V. Acknowledgement ... 115
VI. Erklärung ... 116

I. List of Figures

Figure 1. Formation of the autophagosome 6
Figure 2. Machinery of mammalian autophagosome formation 9
Figure 3. Electron micrograph of a HeLa cell showing double-membrane enclosed vesicles 11
Figure 4. Principles of selective autophagy cargo recognition 13
Figure 5. The LC3-interacting region (LIR) 14
Figure 6. Cargo receptor p62 – a structural perspective 15
Figure 7. Cryo-electron microscopy data of p62 PB1 domain 17
Figure 8. Mechanism of autophagy initiation in yeast 18
Figure 9. Schematic view of FIP200, Atg11 and Atg17 sequences 19
Figure 10. Phylogenetic distribution of Atg11- and Atg17-like domains among proteins in eukaryotes 20
Figure 11. Crystal structure of Atg17-Atg29-Atg31 complex 21
Figure 12. Direct interaction of p62 and FIP200 CTR 23
Figure 13. p62 FIR phosphorylation enhances interaction with FIP200 24
Figure 14. Purification of FIP200 CTR 45
Figure 15. Size exclusion chromatography of GST-p62 FIR 4P 46
Figure 16. FIP200 CTR crystals and selected diffraction images 47
Figure 17. Electron density map of Se-Met FIP200 CTR 50
Figure 18. Ramachandran plot of the FIP200 CTR structure 51
Figure 19. Structure of monomeric FIP200 CTR 52
Figure 20. Organization of FIP200 CTR within the crystal 54
Figure 21. Determination of helix-Claw connectivity 55
Figure 22. Dimerization of FIP200 CTR 56
Figure 23. Comparison of FIP200 Claw domain with functionally or structurally similar proteins 58
Figure 24. Isothermal titration calorimetry of FIP200 CTR and polythymidines 59
Figure 25. Structure-guided identification of the p62 binding site on FIP200 CTR 60
Figure 26. Isothermal titration calorimetry of FIP200 CTR and GST-p62 FIR 4P 63

Figure 27. Interaction of FIP200 CTR and GST-p62 FIR variants monitored by surface plasmon resonance 64
Figure 28. High-density immobilization of p62 required for generation of surface plasmon resonance signal 65
Figure 29. FIP200 – p62 interaction in cells 67
Figure 30. FIP200 interaction with liposomes 69
Figure 31. Scheme of FIP200 – p62 fusion constructs designed for crystallization trials 71
Figure 32. Peptide array 72
Figure 33. Comparison of FIP200 CTR with FIP200 Claw structure 76
Figure 34. Binding site comparison of FIP200 CTR with Atg8 family proteins. 78
Figure 35. Interaction of phosphorylated p62 KIR motif with Keap1 79
Figure 36. Developing a structural model for full-length FIP200 85
Figure 37. Model for FIP200-mediated selective autophagy initiation. 89
Figure 38. Sequence alignment of Atg11 homology regions 107

II. List of Tables

Table 1. The six functional groups of the ATG core machinery 10
Table 2. Crystallization conditions 48
Table 3. Data collection and processing statistics 49
Table 4. Refinement statistics 51

III. Abstract / Zusammenfassung

Abstract

Selective autophagy serves a role in maintaining cellular homeostasis by degradation of aggregated proteins, damaged organelles or pathogens. A double membrane engulfs cargo destined for degradation and thereby forms an enclosed compartment called the autophagosome. Fusion with lysosomes leads to cargo digestion and recycling. In this process, cargo is specifically recognized by dedicated cargo receptors. An unresolved question is how cargo recognition and initiation of autophagy are connected. In yeast, the scaffold protein Atg11 mediates the interaction of cargo receptors with the Atg1 complex required for autophagy initiation. In mammals however, this link has not been established. Interestingly, FIP200, a key player in mammalian autophagy initiation, harbors a C-terminal Atg11 homology domain and has recently been shown to bind to cargo receptor p62.

To gain insights into the mechanistic details of this interaction, the crystal structure of the dimeric FIP200 C-terminal region (CTR) was determined in this work. Both the extended N-terminal helix and the compact C-terminal 'Claw' domain of the CTR contribute to dimer formation. Structure-based mutagenesis allowed the identification of the p62 binding site as a positively charged pocket in the Claw. A point mutant in this pocket was defective for p62-condensate processing, demonstrating the significance of the FIP200 CTR – p62 interaction for selective autophagy. Surface plasmon resonance experiments showed that p62 phosphorylation enhances the weak interaction with FIP200 CTR, therefore identifying receptor phosphorylation as a key regulatory principle. Strikingly, FIP200 CTR also bound to liposomes, suggesting a direct function in membrane recruitment.

Thus, this work describes a missing link between cargo recognition and the initiation of selective autophagy. Further insights into this fundamental process will ultimately help to design therapies against diseases caused by malfunctioning of cellular homeostasis.

Zusammenfassung

Selektive Autophagie ist ein zellulärer Abbauprozess, bei dem toxische Proteinaggregate, defekte Organellen oder eingedrungene Bakterien von einer Doppelmembran umschlossen und nach Fusion mit Lysosomen verdaut werden. Während dieses Prozesses erkennen Rezeptoren spezifisch die Substrate, die abgebaut werden sollen. Wie die Substrat-Rezeptorkomplexe dann die Autophagie-Maschinerie rekrutieren, ist weitgehend unklar. In Hefe vermittelt das Gerüstprotein Atg11 die Interaktion zwischen verschiedenen Rezeptoren und der Kinase Atg1, die essenziell für die Aktivierung der Autophagie ist. Interessanterweise besitzt das humane Protein FIP200, das als Teil des Initiationskomplexes unerlässlich für Autophagie ist, eine C-terminale Domäne, die homolog zu Atg11 ist und die an den Rezeptor p62 bindet.

Um detailliertere Einblicke in den Mechanismus dieser Interaktion zu erhalten, habe ich im Rahmen dieser Arbeit die Kristallstruktur der dimeren FIP200 C-terminalen Region (CTR) bestimmt. Eine N-terminale Helix und eine C-terminale kompakte ‚Claw'-Domäne tragen zur Dimerisierung der CTR bei. Eine Struktur-Funktions-Analyse führte zur Identifizierung einer positiv geladenen p62 Bindetasche. Eine Punktmutante in dieser Tasche verdeutlichte die Relevanz der Bindung von FIP200 und p62 für die selektive Autophagie. Oberflächenplasmonresonanz Messungen demonstrierten, dass die schwache FIP200-p62 Interaktion durch Phosphorylierung von p62 verstärkt wird. Dies deutet auf eine Regulation der FIP200-p62 Bindung durch Phosphorylierung hin. Außerdem konnte eine direkte Bindung der FIP200 CTR an Liposomen nachgewiesen werden.

Durch die Struktur-Funktions-Analyse konnte ich mechanistische Einblicke in die Rekrutierung der Autophagie-Maschinerie durch Autophagie-Substrate erhalten. Weitere Einsichten in selektive Autophagie werden letztlich dabei helfen, neue Therapien gegen Krankheiten mit gestörter Zell-Homöostase zu entwickeln.

1. Introduction

1.1 General principles of autophagy

Autophagy is an evolutionary conserved degradation mechanism for maintaining cellular homeostasis and coping with stress and nutrient deprivation (Mizushima, 2007; Till et al., 2015). In contrast to the proteasomal system, large structures like damaged organelles, pathogens, or toxic protein aggregates can be processed by autophagy (Dikic 2017). During this process, double membranes engulf autophagic cargo, thereby forming autophagosomes that fuse with hydrolases-containing lysosomes to degrade their contents (Mizushima, 2007). Autophagy was first described in the 1960s (Ashford and Porter, 1962; de Duve and Wattiaux, 1966). In the last decades it has been studied intensively (Bento et al. 2016; Farré and Subramani 2016), culminating in a Nobel Prize award for the identification of genes involved in autophagy to Yoshinori Ohsumi in 2016.

In a first step, the autophagy initiation complex is activated, and a membrane precursor is formed (initiation, Figure 1). In yeast, this occurs at the phagophore assembly site (PAS) located closely to vacuoles, whereas in mammals the so-called omegasome, an expansion of the endoplasmic reticulum (ER) membrane, serves as an initiation site. After the core autophagy machinery has been recruited to the initiation site, the isolation membrane is formed - an autophagosomal membrane precursor (nucleation). Cargo material is subsequently sequestered in a growing cup-shaped membrane, called the phagophore (elongation). Eventually, the double-membrane closes and forms the autophagosome. Upon fusion with the lysosome, the cargo material is degraded by hydrolyzing enzymes and building blocks like amino acids or lipids are recycled to the cytoplasm (Dikic and Elazar, 2018; Nakamura and Yoshimori, 2017). Autophagy can be induced by starvation, leading to bulk degradation of cellular contents for nutrient supply (Kuma et al. 2004; Mortimore and Schworer 1977). In non-starved cells, however, autophagy has been described as a constitutive housekeeping process (Dikic 2017).

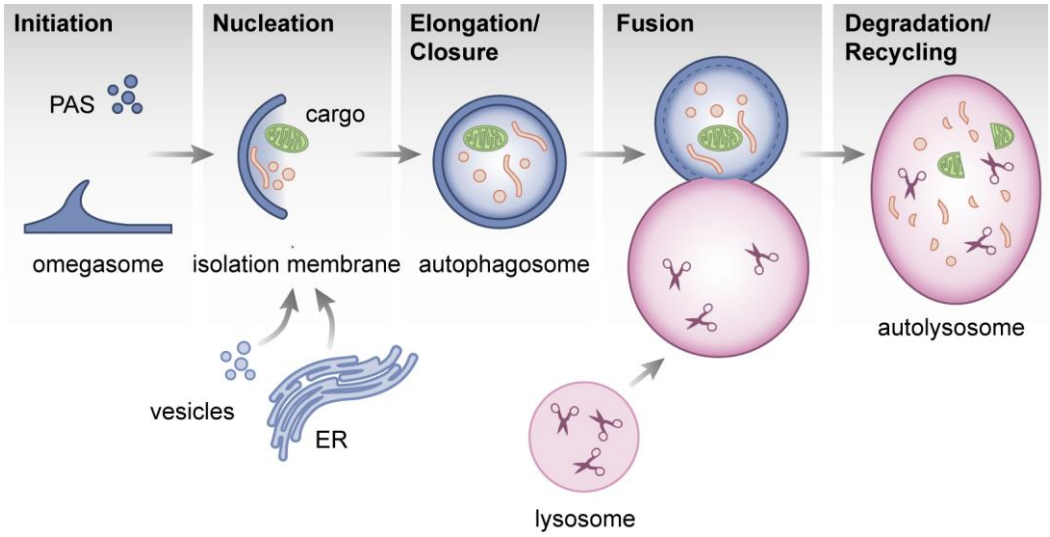

Figure 1. Formation of the autophagosome. During initiation, the autophagic core machinery assembles at the phagophore assembly site (fungi) or the omegasome (metazoa). Activation of a set of protein complexes leads to nucleation of a double-membrane and its elongation. Thereby, cargo material is sequestered within a double membrane compartment called the phagophore. Finally, a closed autophagosome is formed that fuses with the lysosome. In the autolysosome, cargo material is degraded by hydrolases and recycled to the cell. Figure adapted with permission from Subramani and Malhotra 2013.

1.2 Autophagy and disease

Autophagy has been well described in yeast, and substantial knowledge about the mammalian system has been gathered in the last decade (Bento et al. 2016; Farré and Subramani 2016). However, many mechanistic details of the mammalian system are still lacking due to its higher complexity compared to yeast. Since defective autophagy is involved in a plethora of diseases, mammalian autophagy has become a major research interest in the recent years (Dikic and Elazar 2018).

Malfunctioning of aggregate clearance, for example, can lead to neurodegenerative diseases in mice (Hara et al., 2006; Komatsu et al., 2006). Defective autophagy has been linked to metabolic diseases and inflammation (Levine and Kroemer 2019) and bacterial infections (Ogawa et al. 2005). In cancer, autophagy can have positive as well as negative implications: It has been shown that expression of autophagic components has a protective role in cancer development by, for example, enhancing tumor suppression (Liang et al., 1999) or promoting genomic stability (Wang et al., 2016). Fast-growing tumors, on the other hand, profit from increased nutrient supply and toxic waste removal via autophagy stimulation

(Apel et al., 2008; Guo et al., 2011; Lock et al., 2011). Autophagy emerges to be crucial for a healthy interplay between catabolic and anabolic processes (Kaur and Debnath, 2015; Singh and Cuervo, 2011). Moreover, studies on calorie restriction showed that autophagy is an important factor in ageing and lifespan (López-Otín et al. 2016).

Due to the numerous links of autophagy and disease, a thorough understanding of its molecular mechanisms is essential for designing appropriate therapies.

1.3 The autophagy core machinery

A complex network of proteins is involved in autophagy, following a hierarchic mode of action (Suzuki 2007). Over 40 of those so-called ATG (autophagy related gene) proteins have been described until today (Klionsky et al., 2016). The proteins belonging to the core autophagic machinery can be grouped according to their function, as listed in Table 1 and are required for starvation-induced autophagy. In brief, these comprise the Unc-51-like autophagy activating kinase 1 complex (ULK1)/Atg1 complex in yeast, responsible for autophagy initiation; the class III phosphatidylinositol 3-kinase complex (PI3K), important for autophagosomal membrane signature; two ubiquitin-like conjugation systems, responsible for lipidation of ubiquitin-like proteins and membrane elongation; the ATG2-ATG18 system for maturation and closure; and the ATG9-associated proteins important for membrane supply by vesicle trafficking from the Golgi.

The universal energy sensor of the cell, mammalian target of rapamycin complex 1 (mTORC1/TOR in yeast) is inactivated upon stimuli like low cellular energy levels, stress or hypoxia (Boutouja et al., 2019; Høyer-Hansen and Jäättelä, 2007). This results in autophagy initiation at the ER membrane by activation of the ULK1 complex which is composed of the proteins ULK1, ATG101, ATG13 and FAK family kinase-interacting protein of 200 kDa (FIP200) (Figure 2) (Ganley et al., 2009; Jung et al., 2009). ATG13 is a protein crucial for signal transmission from mTORC1 to ULK1 (Kamada et al., 2000). FIP200 and ATG101 are scaffold proteins essential for autophagy (Hara et al., 2008; Hosokawa et al., 2009). However, their functions have not yet been entirely understood. Active ULK1 stimulates the PI3K complex by phosphorylation (Russell et al. 2013) leading to generation of the

autophagosomal membrane signature lipid phosphatidylinositol 3-phosphate (PI(3)P) at the emerging isolation membrane (Backer, 2008; Nascimbeni et al., 2017). In yeast, Atg1 also phosphorylates Atg9, the only membrane protein essential in autophagy initiation (Papinski et al., 2014). Atg9 resides in small vesicles (30 – 60 nm) originating from the Golgi apparatus and early endosomes (Yamamoto et al., 2012). Recruitment of these vesicles to the isolation membrane provides lipids for isolation membrane elongation (Mari et al., 2010). Once PI(3)P has been generated at the membrane, it is recognized by FYVE and WD40 domain containing proteins (WIPI2, DFCP1) that ultimately recruit two ubiquitin-like protein conjugation systems required for anchoring the ubiquitin-like protein microtubule-associated protein 1 light chain 3B (MAP1LC3B, hereafter LC3B) to phosphatidylethanolamine (PE) on the autophagosomal membrane (Dooley et al., 2014; Kabeya, 2004; Krick et al., 2006; Mizushima et al., 1998). This process has been termed LC3B lipidation. LC3B belongs to the Atg8 protein family that is conserved among eukaryotes and plays a role in intracellular trafficking and autophagy. The mammalian subfamilies comprise MAP1LC3, γ-amino-butyric acid receptor-associate protein (GABARAP), and GABARAP-like (GABARAPL) (Shpilka et al., 2011; Wild et al., 2014). Expansion of the membrane results in cargo loading and eventually closure of the autophagosomal membrane (Turco & Martens, 2016).

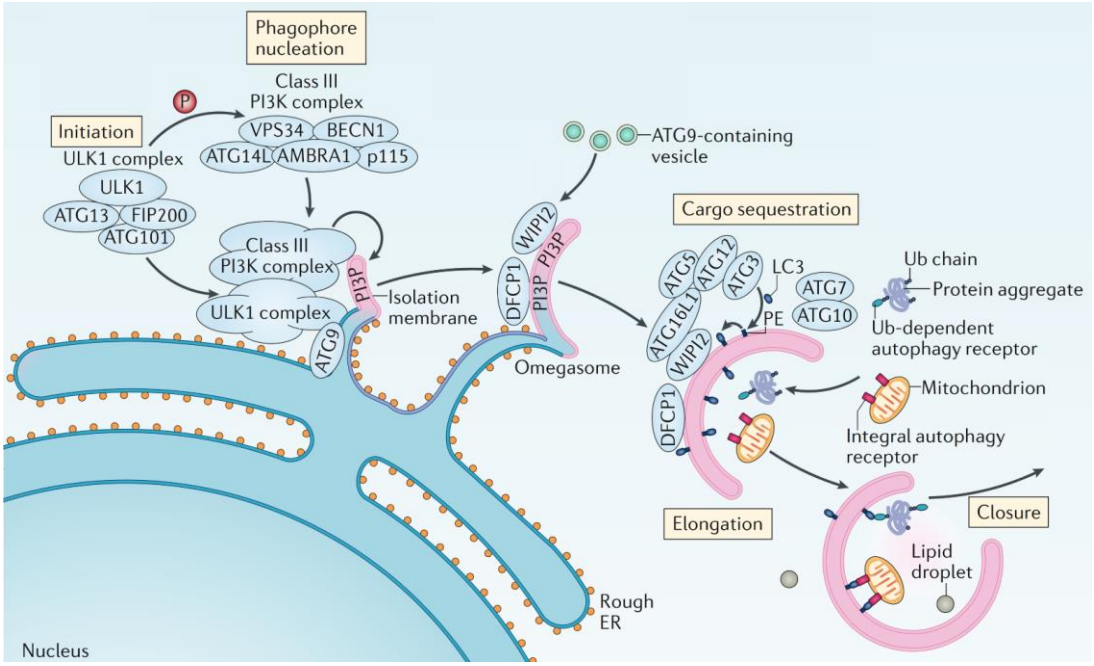

Figure 2. Machinery of mammalian autophagosome formation. Activation of the ULK1 complex by stress or nutrient deprivation leads to phosphorylation and activation of the PI3K complex. Both complexes localize to the rough ER membrane, where PI3K generates PI(3)P. Upon binding of the PI(3)P recognizing adapter proteins DFCP1 and WIPI2, the ubituitin-like conjugation system (ATG16L1, ATG5, ATG12, ATG3, ATG7 and ATG10) is recruited to the phagophore and catalyzes the covalent attachment of LC3B to PE. Subsequently, the double membrane is elongated around cargo destined for degradation. Figure adapted with permission from Clarke and Simon 2018.

Table 1. The six functional groups of the ATG core machinery. Adapted from Stanley, Ragusa, and Hurley 2014

Complex	Yeast	Mammals	Molecular function
Atg1/ULK1 complex	Atg1 Atg13 Atg17 Atg29 Atg31	ULK1 ATG13 FIP200 ATG101	Atg1, which is a Ser/Thr kinase, forms a transient autophagy-specific complex with Atg13, Atg17, Atg29, and Atg31. Atg17, Atg29, and Atg31 form a stable 2:2:2 complex regardless of cellular nutrient status and serve as a scaffold that is important for protein localization to the PAS. ULK1, ATG13, FIP200 and Atg101 form a stable complex in mammals.
class III PI3-kinase complex	Vps34 Vps15 Vps30/Atg6 Atg14	VPS34 VPS15 Beclin1 Atg14/BARKOR	The class III PI3-kinase complex is responsible for the production of PI(3)P at the PAS. Atg14 specifically targets the complex to the PAS.
Atg2-Atg18 complex	Atg2 Atg18	ATG2 WIPI1-4	Atg18 is a PI(3)P sensor that forms a complex with Atg2 and Atg9.
Atg12 conjugation system	Atg12 Atg7 Atg10 Atg5 Atg16	ATG12 ATG7 ATG10 ATG5 ATG16L1/2	Atg7 (E1-like enzyme) and Atg10 (E2-like enzyme) conjugate Atg12 to Atg5. Atg16 is a homodimer that forms a complex with Atg5 and Atg12 and is important for Atg8 conjugation to PE.
Atg8 conjugation system	Atg8 Atg4 Atg7 Atg3	LC3A/B/C GABARAP GABARAPL1/2/3 ATG4-D ATG7 ATG3	Atg4 is a hydrolase that activates Atg8/LC3. Atg8 is conjugated to PE through Atg7 (E1-like enzyme), the Atg12–Atg5–Atg16 complex, and Atg3 (E2-like enzyme).
Atg9 associated	Atg9 Atg23 Atg27	ATG9	Integral membrane protein involved in autophagy. Atg23 is a peripheral membrane protein required for Atg9 trafficking from the Golgi. Atg27 is a type I integral membrane protein required for Atg9 trafficking from the Golgi.

1.4 Selective autophagy

Autophagy has been studied extensively in yeast cells and is thought of as a mechanism for random bulk degradation of cytosolic material during starvation (Tsukada and Ohsumi, 1993). The previous section described the well-known core machinery required for starvation-induced autophagy. However, autophagy also occurs under basal conditions and cargo material is selected in a highly specific manner. Selective autophagy applies to a variety of cargos, for example malfunctioning organelles like mitochondria (mitophagy), ER (ER-phagy), peroxisomes (pexophagy), or even parts of the nucleus (nucleophagy) (reviewed in Farré and Subramani 2016). Selective autophagy also recognizes pathogens (xenophagy) (Méresse et al., 1999; Rich et al., 2003) or protein aggregates (aggrephagy, Figure 3) (Lamark and Johansen, 2012). Accordingly, an additional set of ATG proteins is required for providing selective autophagy specificity.

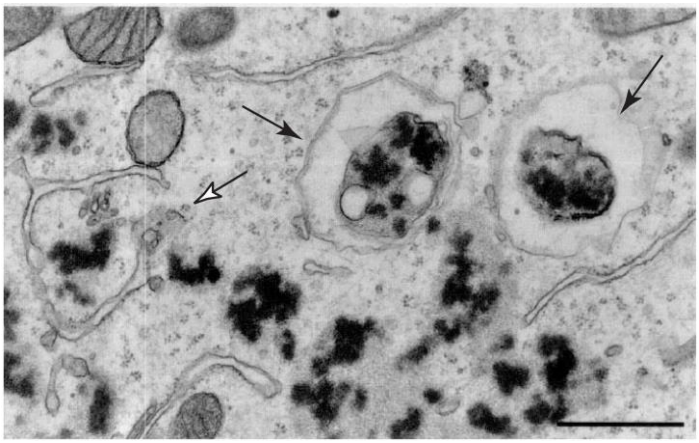

Figure 3. Electron micrograph of a HeLa cell showing double-membrane enclosed vesicles containing electron-dense protein aggregates (black arrows) and an immature phagophore (white arrow). Scale bar = 1 μm. Figure from Wojcik et al. 1996.

1.4.1 Cargo recognition

Specificity of selective autophagy types is ensured by cargo receptors that recognize substrates marked for degradation. Cargo receptors function as adaptors by binding simultaneously to the cargo and to the autophagosomal membranes via interaction with Atg8 family proteins (Shintani et al., 2002).

Cargo recognition can be mediated in several ways. Firstly, organelle- or cargo-specific markers can directly interact with Atg8 family proteins as membrane-bound receptors or via cargo receptors (Figure 4A, left). These include mitophagy receptors NIX, FUNDC1, or Atg32 (yeast) (Kanki et al., 2009; Liu et al., 2012; Novak et al., 2010), ER-phagy receptors FAM134B or Atg40 (yeast) (Khaminets et al., 2015; Mochida et al., 2015), or pexophagy receptors NBR1 or Atg30 (yeast) (Deosaran et al., 2013; Farré et al., 2008). Secondly, cargo recognition is often dependent on ubiquitination of the target (Figure 4A, right). A dedicated set of receptors recognizes ubiquitinated protein aggregates, organelles, bacteria, and the proteasome, among other targets (Kirkin et al., 2009a). For aggrephagy, the following ubiquitin-binding receptors have been described: p62/sequestosome 1 (SQSTM1) (hereafter p62), NBR1, NDP52 and TOLLIP (Figure 4B) (Kirkin et al., 2009b; Lu et al., 2014; Pankiv et al., 2007; Zhou et al., 2013). All these receptors harbor an LC3 interacting region (LIR) and a ubiquitin-associated domain (UBA), that bind to the autophagosomal membrane and ubiquitinated cargo, respectively (Figure 4C). Khaminets, Behl, and Dikic 2016 have reviewed autophagy receptors in detail. Interestingly, different cargo receptors are often found in the same autophagic pathway – suggesting cooperativity among the receptors.

Cargo ubiquitination adds a level of complexity to autophagy which is necessary for its tight regulation and important for the crosstalk between by the ubiquitin-proteasome system (UPS) and autophagy (Dikic, 2017). In contrast to the proteasomal degradation system, autophagy cargo receptors preferentially recognize monoubiquitin and polyubiquitin chains linked via K63 instead of K48 (Long et al., 2008). Also, autophagosomes are able to sequester large substrates, that might not be applicable for proteasomal degradation (Verhoef et al., 2002).

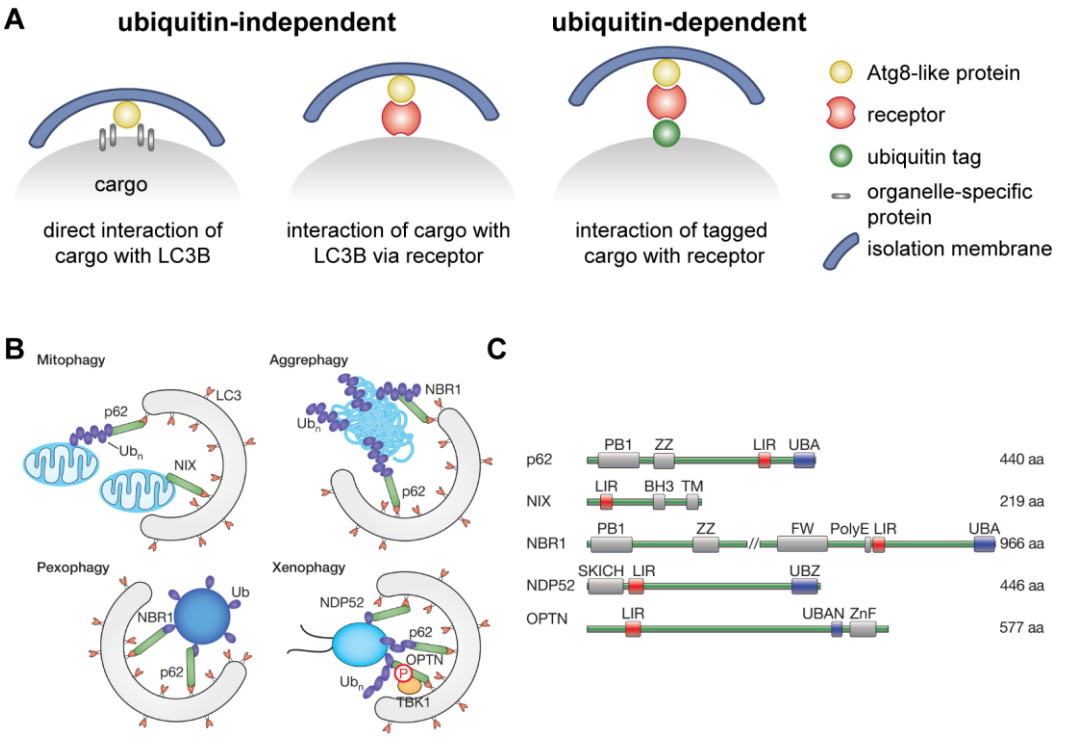

Figure 4. Principles of selective autophagy cargo recognition. A) Cargo recognition is mediated by different means and can be ubiquitin-dependent or -independent. B) Examples of cargo recognition in different selective autophagy processes. C) Schematic representation of cargo receptor domain architecture. Figure A) adapted from Levine and Kroemer 2019; Figure B) and C) from Stolz, Ernst, and Dikic 2014 (with permissions).

1.4.2 The LC3-interacting region (LIR) motif

Cargo receptors serve as adaptors by linking cargo with the autophagosomal membrane through interaction with Atg8 family proteins. To this end, receptors contain a conserved binding motif termed Atg8-interacting motif (AIM) in yeast and LC3 interacting region (LIR) in mammals (Birgisdottir et al., 2013). The two aromatic and hydrophobic residues of the LIR consensus sequence [W/F/Y]xx[L/I/V] bind to distinct hydrophobic pockets on Atg8 family proteins (Figure 5A) (Alemu et al., 2012; Noda et al., 2008). The backbone atoms of the residues sandwiched between the hydrophobic amino acids engage in ß-sheet interactions. Often, the core consensus sequence is flanked by negatively charged amino acids that mediate additional interactions with the overall positively charged binding grooves on Atg8 family proteins (Figure 5B) (Ichimura et al., 2008a; Noda et al., 2008; Pankiv et al., 2007). This interaction mode is well conserved from yeast to humans. Interestingly, LIR

motifs are found among many autophagy-related proteins that do not serve as cargo receptors, displaying the complexity of the LC3 interactome (Figure 5C) (Birgisdottir et al., 2013; Wild et al., 2014).

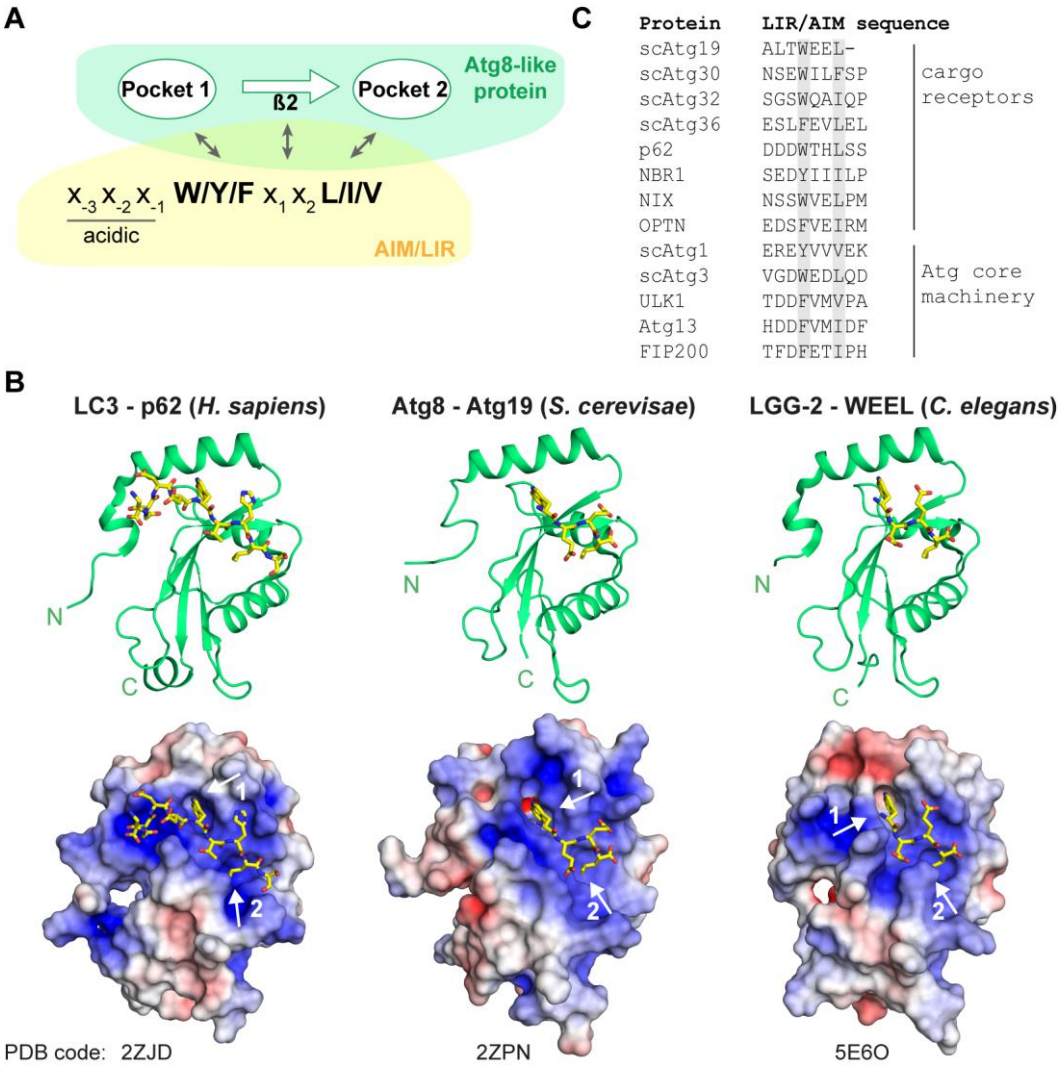

Figure 5. The LC3-interacting region (LIR). A) Schematic representation of AIM/LIR interaction with Atg8 family proteins. The two signature hydrophobic residues of the LIR motif interact with two distinct hydrophobic pockets on Atg8 family proteins. The residues in between engage in ß-sheet interactions. Flanking acidic residues mediate auxiliary interactions. B) Structures of LC3B in complex with the p62 LIR (left), Atg8 in complex with Atg19 LIR (middle) and LGG-2 in complex with WEEL peptide. Atg8 family proteins in green ribbon representation (top) or electrostatic surface potential (bottom) with ligands shown as yellow sticks. Hydrophobic binding pockets are indicated by white arrows in the bottom panels. Electrostatic surface potential range: - 5 keV (red) to + 5 keV (blue). C) Examples of proteins involved in selective autophagy and their LIR/AIM motifs.

1.4.3 The role of cargo receptor p62 in autophagy

The well-described cargo receptor p62 is involved in different selective autophagy processes, and especially its role in aggrephagy has been studied intensively (Gruss et al., 2013; Komatsu et al., 2007; Pankiv et al., 2007). p62 is composed of an N-terminal Phox and Bem1p domain (PB1), a C-terminal ubiquitin binding domain (UBA), a ZZ-type zinc-finger domain (ZZ) and several interaction motifs (Figure 6) that will be shortly introduced in this section.

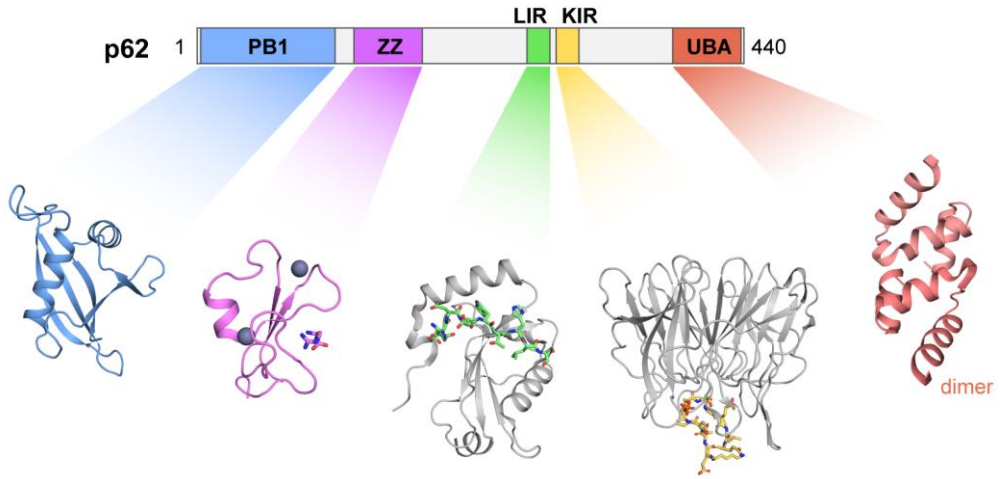

Figure 6. Cargo receptor p62 – a structural perspective. Schematic representation of p62 domain organization with macromolecular structures of p62 domains or interacting motifs known to date. PDB entries: PB1 (2KKC), ZZ (6MJ7), LIR (2ZJD), KIR (3WDZ), UBA (3B0F).

As an autophagy receptor, p62 binds ubiquitinated cargo through its UBA domain. It preferentially recognizes monoubiquitin and K63-linked polyubiquitin chains (Seibenhener and Babu, 2004). p62 stays associated with the cargo throughout the autophagy process and is eventually degraded by the autolysosome (Bjørkøy et al., 2005). Accordingly, defective autophagy leads to accumulation of so-called p62-bodies or condensates (Komatsu et al., 2007) that also form upon p62 overexpression (Paine et al., 2005). Protein condensates have been described as cellular compartments without bounding membrane. They are generated by dynamic and reversible phase separation of proteins and exhibit a liquid character (Hyman et al., 2014).

PB1 domains are known to mediate heterodimerization (Lamark et al., 2003). In p62, however, the PB1 domain forms front-to-back homodimers. Accordingly, the PB1 domain has the ability to assemble in oligomeric arrays (Wilson et al., 2003). Flexible helical scaffolds of up to 0.1 μm in length were monitored for the p62 PB1 domain by cryo-electron microscopy (Figure 7, Ciuffa et al. 2015). p62 oligomerization is crucial for its localization to the phagophore and autophagic clearance of protein aggregates (Horos et al., 2019; Itakura and Mizushima, 2011).

Recent studies have shown that the ZZ domain is required for binding to N-terminally arginylated substrates (Cha-Molstad et al., 2017; Yoo et al., 2018; Zhang et al., 2018). N-terminal arginylation is known as an important marker for proteasomal protein degradation (Tasaki et al., 2012) and has now been linked to autophagy as well. Interaction with N-terminally arginylated substrates enhanced p62 aggregation and its turnover by autophagy. Furthermore, the ZZ-domain was suggested to exert an autoinhibitory function on p62 by binding to a regulatory linker region (Zhang et al., 2018).

The p62 LIR motif (DDDWTHL) is required for interaction with LC3B (Noda et al., 2008) and links the p62-cargo complex to the phagophore. Mutation of one of the core hydrophobic residues or the aspartates impairs selective degradation of p62 and leads to increased formation of p62 and ubiquitin-rich condensates (Ichimura et al., 2008b; Johansen and Lamark, 2011)

Apart from its role in autophagy, p62 functions as a signaling hub (Moscat et al., 2016). The PB1 domain mediates heterodimerization with PKCζ, MEK5, and ERK1. These interactions, as well as binding to the TNF receptor associated factor 6 (TRAF6) are required for NF-κB signaling. (Moscat et al., 2007; Nakamura et al., 2010; Sanchez et al., 1998). Binding to Keap1 via the Keap1 interacting region (KIR) mediates oxidative stress response by modulating Nrf2 signaling (Komatsu et al., 2010). Furthermore, p62 harbors nuclear import and export signals (Pankiv et al., 2010).

Results from this thesis will reveal an interaction partner of p62 that links cargo recognition to selective autophagy initiation. The current understanding of the initiation process in yeast will be outlined in the next section.

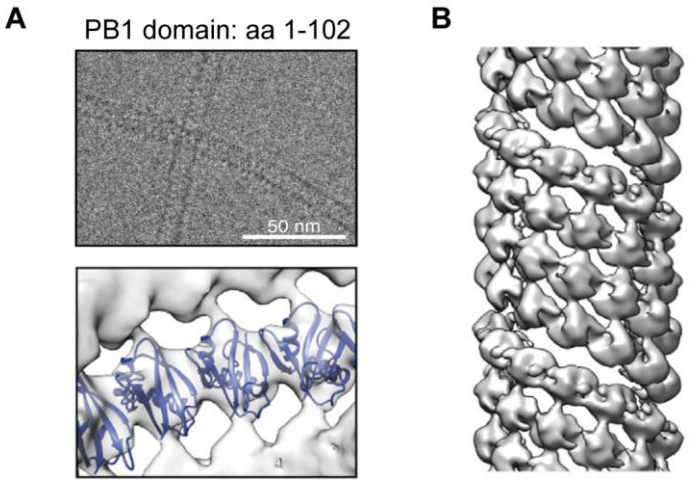

Figure 7. Cryo-electron microscopy data of p62 PB1 domain. A) Micrograph showing long PB1 filaments (top) and surface EM density representation of helical filament with fitted PB1 crystal structure, inside view (bottom) B) 3D structure of the helix formed by PB1 domains. Figures from Ciuffa et al. 2015.

1.5 Selective autophagy initiation in yeast

As described above, selective autophagy receptors link cargo material to the phagophore by interaction with Atg8 family proteins. But how does autophagosomal membrane formation come into play during selective autophagy? Several studies indicate that the cargo itself constitutes a signal for autophagy initiation. In the well-studied cytoplasm to vacuole (Cvt) pathway in yeast, the cargo receptor Atg19 is essential for delivering large complexes of aminopeptidase I (Ape1) to the vacuole (Umekawa and Klionsky, 2012). Although being a biosynthetic mechanism, the Cvt pathway has been proposed as a model for selective autophagy due to mechanistic similarities (Lynch-Day and Klionsky, 2010). Interestingly, Atg19 does not only establish the interaction with Atg8 in order to link the Ape1 protein complexes to an enwrapping membrane. Prior to Atg8 engagement, Atg19 binds to Atg11, a scaffold protein associated with the Atg1 complex (Figure 8, left panel) (Shintani et al., 2002; Suzuki et al., 2002). Under nutrient-rich conditions, Atg11 interacts with Atg19 upon receptor phosphorylation (Pfaffenwimmer et al., 2014), resulting in activation of the Atg1 complex (ULK1 yeast homologue) through Atg1 autophosphorylation (Kamber et al., 2015). The active Atg1 complex subsequently initiates isolation membrane formation via a cascade of events described in section 1.3. Additionally to its function in the Cvt pathway, Atg11 is implicated in various selective autophagy processes in

yeast (Farré et al. 2008; Kanki and Klionsky 2008; Okamoto, Noriko, and Ohsumi 2009).

During starvation-induced bulk autophagy, Atg1 assembles with Atg13 as well as the Atg17-Atg29-Atg31 subcomplex to drive autophagy initiation (Figure 8, right panel) (Cheong et al., 2008; Klionsky et al., 2016). Atg17 is another scaffold protein that modulates Atg1 kinase activity, just like Atg11 (Kamada et al., 2000). Both proteins also recruit small membrane vesicles via Atg9 to the PAS (He et al., 2006; Sekito et al., 2009). Strikingly, Atg11 and Atg17 share a common structural architecture, e.g. they both contain several coiled-coil domains (Yorimitsu and Klionsky, 2005). This suggests that the scaffold proteins Atg11 and Atg17 serve similar roles in starvation-induced and constitutive autophagy in yeast.

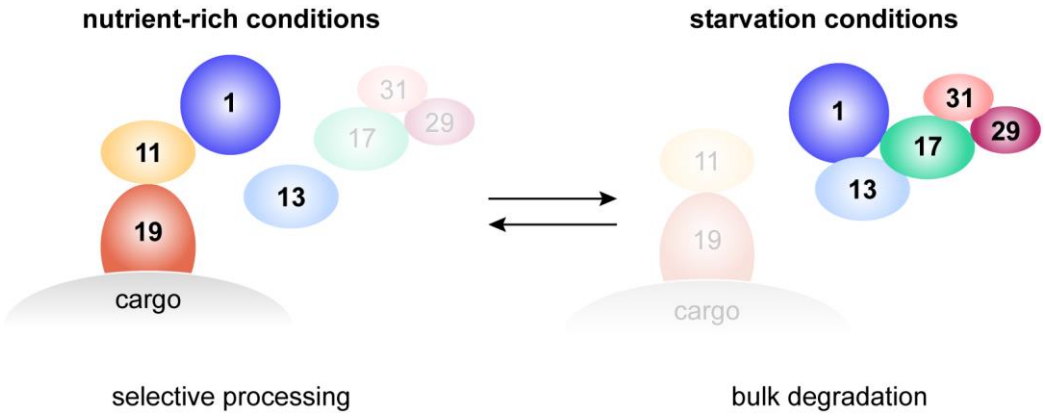

Figure 8. Mechanism of autophagy initiation in yeast. Selective processing of cargo occurs under nutrient-rich conditions and involves recruitment of the Atg1 kinase via the scaffold protein Atg11 to cargo receptor Atg19. In this case, the subcomplex composed of Atg17-Atg29-Atg31 is dispensable for selective autophagy (left). Under starvation conditions, Atg1 assembles with Atg13 and the subcomplex Atg17-Atg29-Atg31 to initiate bulk degradation (right). Adapted with permission from Nakatogawa et al., 2009.

1.6 FIP200 - the counterpart of yeast Atg11 and Atg17

In metazoan, understanding of Atg11- or Atg17-like scaffolds is incomplete. Although candidates have been suggested for *C. elegans* and *D. melanogaster* (Lin et al., 2013; Rui et al., 2015), studies on mammalian scaffolds are lacking. FIP200, a component of the ULK1 complex, has been proposed to be the functional counterpart of Atg17 in mammals (Hara and Mizushima, 2009).

FIP200, also known as RB1-inducible coiled-coil protein 1 (RB1CC1), is a multifunctional protein linked to cell survival, cell proliferation, cell adhesion, and cell growth (Abbi et al., 2002; Gan and Guan, 2008; Gan et al., 2005; Melkoumian et al., 2005; Ueda et al., 2000; Watanabe et al., 2005). Moreover, FIP200 is a key player in autophagy initiation as it is a central component of the ULK1 complex. LC3B lipidation is decreased and autophagy impaired upon FIP200 deletion (Hara et al., 2008). FIP200 also binds to ATG16L1, a component of the E3 ligase complex required for LC3B lipidation. The interaction is necessary for directing ATG16L1 to the isolation membrane (Nishimura et al., 2013) and indispensable for ULK-dependent autophagy (Gammoh et al., 2013). Structural and functional information on FIP200 is still lacking. However, analogies can be drawn from yeast.

FIP200 has been suggested as the functional counterpart of Atg17 because of the following reasons: Both Atg17 and FIP200 (1) contain large coiled-coil regions, (2) bind to the C-terminus of Atg1/ULK1 and (3) are required for Atg1/ULK1 kinase activity (Hara and Mizushima, 2009). FIP200 also shares a short region of weak sequence similarity with Atg17 (Li, Chung, and Vierstra 2014). Nevertheless, FIP200 is about three times larger than Atg17 (1594 vs. 417 amino acids, respectively), suggesting the presence of additional functional modules. Strikingly, the C-terminal region of FIP200 is homologous to the C-terminus of Atg11 and the overall domain architecture seems closer to Atg11 than to Atg17 (Figure 9, sequence alignment: Appendix B, Figure 38). This opens up the exciting possibility that FIP200 integrates the partly redundant roles of yeast Atg11 and Atg17 in one molecule. The fact that the presence of both Atg11- and Atg17-like domains in the same protein is wide-spread among eukaryotes highlights the functional relevance of this combination (Figure 10) (Li et al., 2014).

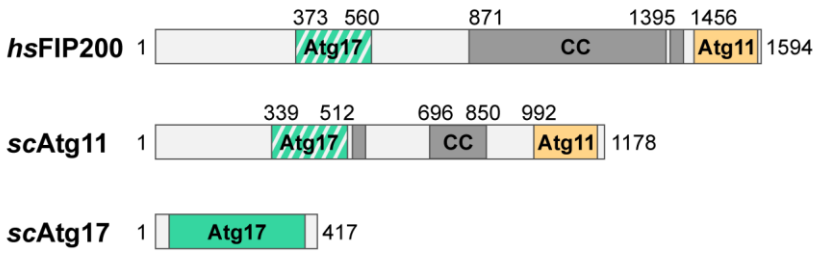

Figure 9. Schematic view of FIP200, Atg11 and Atg17 sequences, indicating conserved regions and structural motifs.

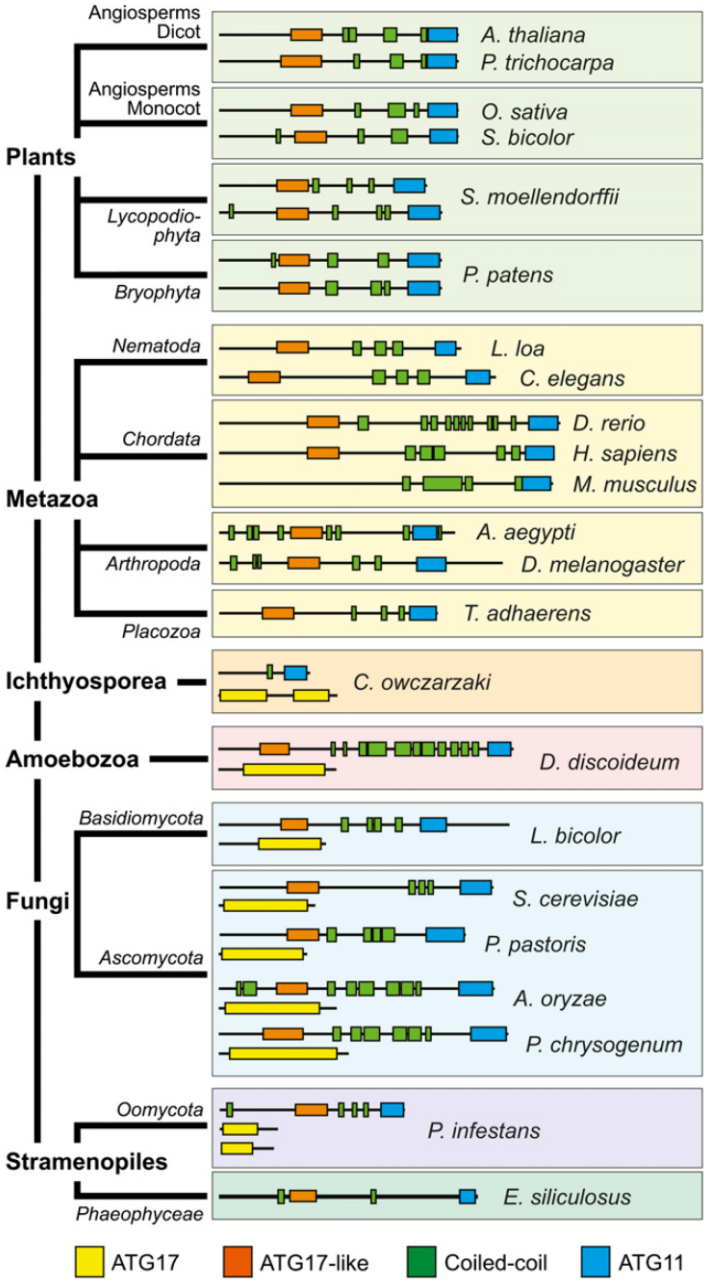

Figure 10. Phylogenetic distribution of Atg11- and Atg17-like domains among proteins in eukaryotes. Figure from Li, Chung, and Vierstra 2014.

Protein function can often be deduced from its macromolecular structure. While no structural information is available on Atg11 yet, the crystal structure of the Atg17-Atg29-Atg31 subcomplex from the yeast species *Lachancea thermotolerans* has been solved (Ragusa et al., 2012). Atg17 forms an S-shaped dimeric coiled-coil with Atg29 and Atg31 bound to the inner side of each Atg17 crescent (Figure 11A). Due to

the shape and diameter of the crescents, Atg17 has been suggested to be a scaffold for small Atg9 vesicles (Figure 11B) (Ragusa et al., 2012). Although a direct interaction of Atg17 with liposomes could not be observed *in vitro* (Ragusa et al., 2012), it was shown that Atg17 is able to indeed bind vesicles through interaction with the membrane protein Atg9 (Rao et al., 2016). In the Atg17-Atg29-Atg31 complex, the Atg9 interaction was not observed, suggesting a sterical block by Atg29 and Atg31 (Figure 11A), (Ragusa et al., 2012; Rao et al., 2016). Notably, the engagement of the Atg1-Atg13 subcomplex with Atg17-Atg29-Atg31 induced vesicle tethering and autophagy initiation, suggesting a conformational change of Atg29 and Atg31 upon complex formation (Figure 11B) (Rao et al., 2016). Moreover, the direct interaction of the Atg1 C-terminal early autophagy targeting/tethering (EAT) domain with liposomes indicates an additional or cooperative binding mechanism of the entire Atg1 complex with Atg9 vesicles (Cheong et al., 2008).

Figure 11. Crystal structure of Atg17-Atg29-Atg31 complex. A) Crystal structure of Atg17-Atg29-Atg31 complex from *L. thermotolerans*. The Atg17 coiled-coils form an S-shaped dimer. PDB code: 4HPQ. B) Model for vesicle tethering of yeast Atg1-Atg17-Atg29-Atg31 complex. Atg1 EAT domain binds to small vesicles. Atg17 interacts with the Atg1-EAT domain and exerts a scaffolding function on membrane vesicles upon displacement of Atg29-Atg31 by Atg9. Figure B) adapted with permission from (Ragusa et al., 2012).

1.7 Direct interaction of FIP200 C-terminal region (CTR) and p62

Based on the similarities of FIP200, Atg17 and Atg11, collaboration partner Sascha Martens (Max F. Perutz Laboratories (MFPL), Vienna) proposed that FIP200 could serve as a selective autophagy scaffold in humans and interact with cargo receptor p62, analogous to the interaction of Atg19 and Atg11 in yeast.

To test if FIP200 directly interacts with p62, *in vitro* binding studies were performed in the group of Sascha Martens. The data shown in this section have been published in Turco et al. 2019. Initial pull-down experiments indeed showed an interaction of p62 and the FIP200 C-terminal region (CTR, amino acids 1458-1594), harboring the Atg11 homology domain (data not shown). A direct interaction was confirmed by monitoring the recruitment of mCherry-tagged p62 to glutathione sepharose beads coated with glutathione S-transferase (GST) tagged FIP200 CTR (Figure 12A). Further mapping of the binding region on p62 led to identification of a FIP200 interacting region (FIR) that comprises 56 amino acids (p62 aa 326-380). The FIR is located in an unstructured region of p62 that also contains the LIR and KIR motifs. A microscopy-based interaction assay using glutathione sepharose beads coated with GST-p62 variants revealed that FIP200 can bind to the LIR motif only and that mutation of the LIR motif ($_{335}$DDDW$_{338}$>AAAA) within p62 FIR leads to loss of the interaction (Figure 12B,C). Strikingly, LC3B is able to displace FIP200 CTR in a concentration-dependent manner from p62 4P immobilized on beads, suggesting a competition of LC3B and FIP200 for the p62 LIR motif (data not shown).

Based on the results of the *in vitro* studies, it was further investigated if the interaction of p62 and FIP200 would also be detectable in cells. To this end, colocalization was monitored in HAP1 cells by immunofluorescence. While there were a few spots of colocalization in untreated cells, blocking of isolation membrane elongation by the Wortmannin inhibitor or blocking of LC3B lipidation in ATG7 knockout cells led to increased colocalization levels (Figure 12D). This implies a transient role for the FIP200 – p62 interaction during an early stage of autophagy.

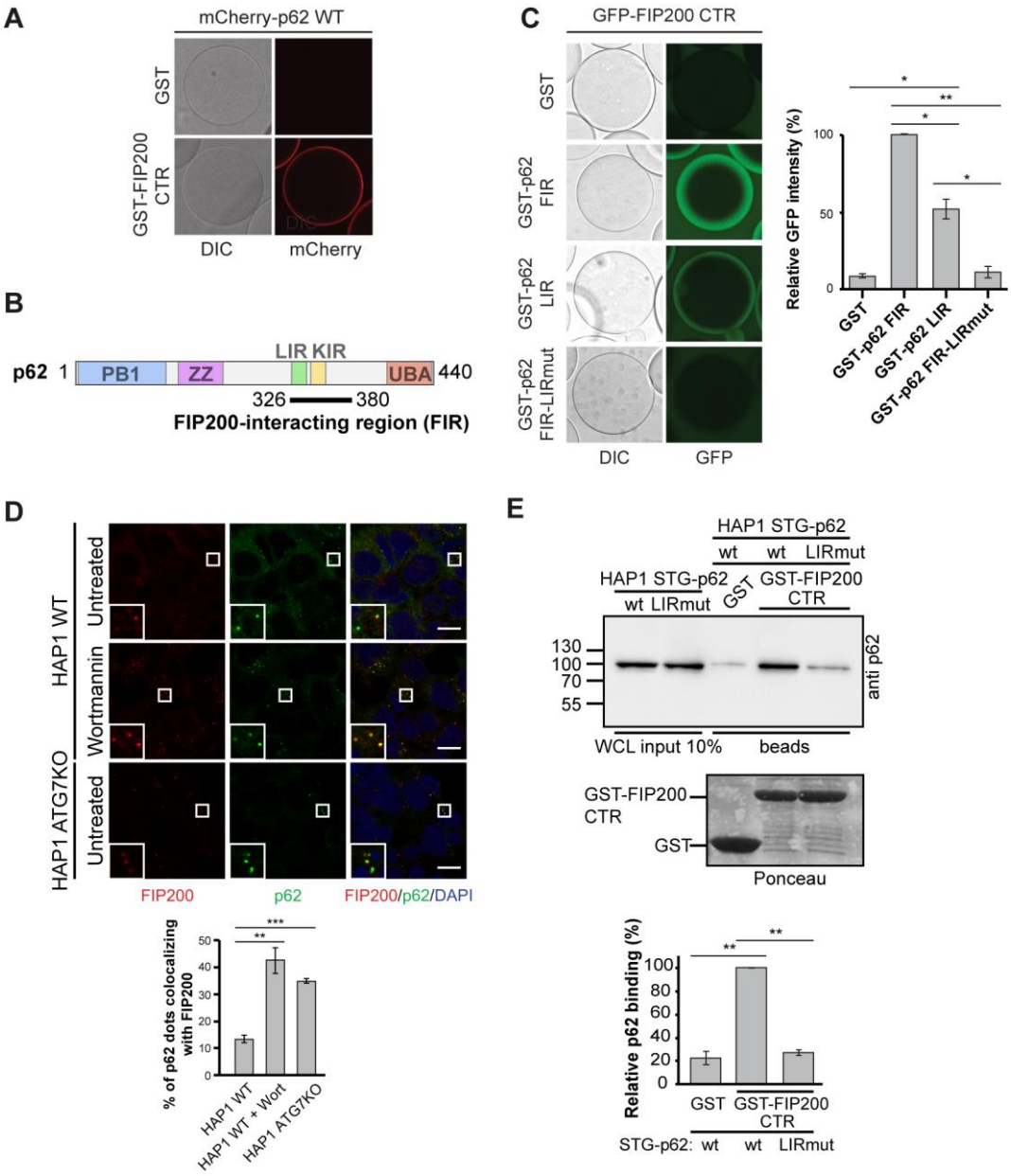

Figure 12. Direct interaction of p62 and FIP200 CTR. A) Recruitment of mCherry-p62 to glutathione beads coated with GST-FIP200 CTR. B) Schematic representation of p62 domains and its FIP200 CTR interacting region (FIR). C) Recruitment of GFP-FIP200 CTR to glutathione beads coated with different GST-p62 variants. Microscopy images of beads at equilibrium (left panel). The GFP signal on the beads was normalized to the signal of GFP-FIP200 CTR bound to GST-p62 FIR coated beads. Average intensity and SEM for n=3 are plotted (right panel). D) Colocalization analysis of p62 and FIP200 in HAP1 cells (wt or ATG7KO) left untreated or treated with Wortmannin. Endogenous p62 and FIP200 were detected by immunofluorescence. Scale bar = 10 µm. Average percentages of colocalization and SEM for n=3 are shown in the bottom panel. E) Pull-down of p62 wt and LIRmut from HAP1 STG-p62 (Strep-TEV-GFP-p62) cell lysates using GST/GST-FIP200 CTR as bait. Loading control of the bait proteins is shown below the blot. Band intensities were measured and normalized to the intensity of p62 wt binding to FIP200 CTR wt. Average band intensities and SEM (n=3) are shown in the bottom panel. Figures from Turco et al. 2019.

Moreover, a pull-down from HAP1 cells confirmed that the p62 LIR motif is required for the interaction, as binding of FIP200 CTR to a p62 LIR mutant engineered by CRISPR/Cas9 was significantly reduced (Figure 12E).

Evidence from mass spectrometry showed that the p62 FIR contains phosphorylation sites at positions S349/T350, S365, S366 and S370/T375 (Figure 13A). Binding of FIP200 CTR to p62 phospho-mimicking variants (serine to aspartate mutation) was indeed enhanced *in vitro*, suggesting a phosphorylation-dependent regulatory mechanism (Figure 13B).

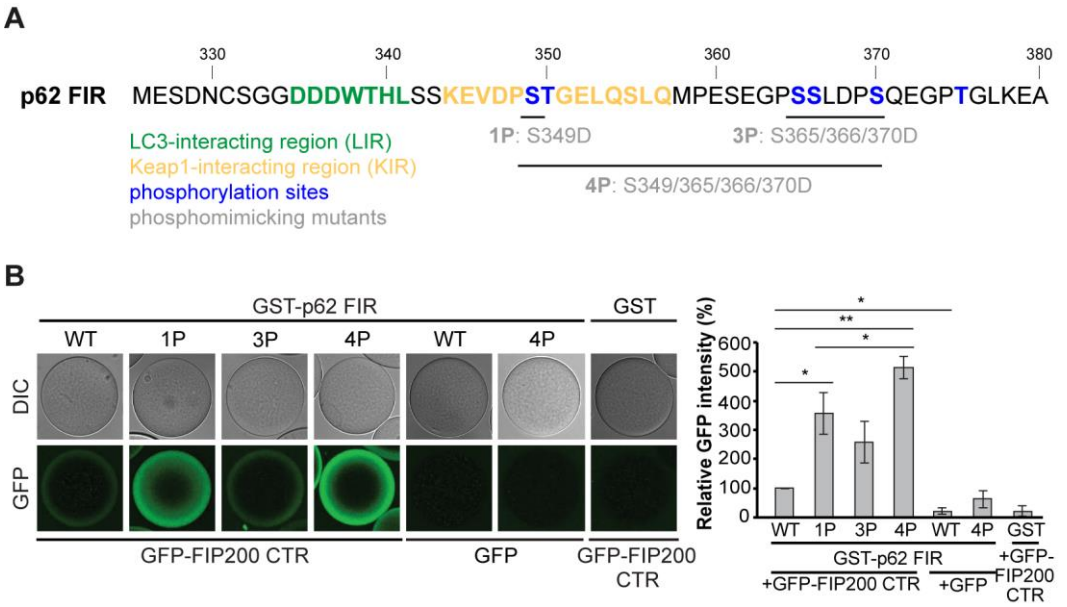

Figure 13. p62 FIR phosphorylation enhances interaction with FIP200. A) p62 FIR sequence with LIR motif marked in green, KIR motif in yellow and phosphorylation sites identified by mass spectrometry in blue. Phospho-mimicking variants designed for further experiments are shown in gray. B) Recruitment of GFP-FIP200 CTR to glutathione beads coated with different GST-p62 FIR phospho-mimicking variants (left panel). GFP signal on the beads was normalized to the signal of GFP-FIP200 CTR bound to GST-p62 FIR 4P. Average intensity and SEM for n=3 are shown. Figure B) from Turco et al. 2019.

2. Scope of this thesis

Selective autophagy is an essential process for maintaining cellular homeostasis by waste removal. Although substantial efforts have been made in the last decade to elucidate the basic principles of selective autophagy, many details are still unclear. An especially urgent question is how initiation of membrane formation is coupled to cargo recognition during cargo-induced autophagy. A direct interaction between FIP200 CTR, a component of the ULK1 complex, and cargo receptor p62 was recently discovered in the group of our collaborator Sascha Martens. This protein-protein interaction is of major importance to the field of selective autophagy because it describes a direct link between cargo and autophagy initiation machinery.

To understand the molecular basis of the FIP200 interaction with p62, I applied biochemical and structural biology methods, in particular X-ray crystallography. In a collaborative approach, structure-based mutagenesis assays allowed for the identification of the p62 binding site on FIP200. Surface plasmon resonance measurements corroborated a regulatory mechanism by p62 phosphorylation. Finally, the obtained structural insights proved to be valuable for designing *in vivo* experiments to further understand how the recruitment of the autophagy machinery and membrane nucleation at p62 condensates is achieved.

Insights on FIP200 CTR structure and function are highly relevant as they can be translated to the many selective autophagy processes in different species that rely on the Atg11 scaffold.

3. Materials and methods

3.1 Materials

This section lists chemicals and materials used in experiments conducted by myself at the Max-Delbrück Center.

3.1.1 Chemicals

If not stated otherwise, chemicals and consumables were obtained from the following companies: Roth, Jena Bioscience, Qiagen, Roche, Sigma-Aldric, Merck, GE Healthcare and Life Technologies. A list of chemicals can be found in Appendix D.

3.1.2 Instruments

Instruments used in this study are listed in Appendix C.

3.1.3 Enzymes

Alkaline Phosphatase, Calf Intestinal (CIP)	New England Biolabs
*Bam*HI HF	New England Biolabs
DNAse-I	Roche
*Dpn*I	New England Biolabs
*Eco*RI	New England Biolabs
KOD polymerase	Merck
*Nde*I	New England Biolabs
PreScission protease	GE Healthcare (produced inhouse)
T4 polynucleotide kinase (PNK)	New England Biolabs
T4 DNA ligase	New England Biolabs
Tobacco etch virus protease (TEV)	produced inhouse
Taq DNA polymerase	New England Biolabs
*Xho*I	New England Biolabs

3.1.4 Kits

Amine Coupling kit	GE Healthcare
GST capture kit	GE Healthcare
innuPREP plasmid mini kit 2.0	Analytic Jena
NuPAGE© Novex 4-12% Bis-Tris Gel 1.5 mm, 10/15 well	LifeTechnologies
QIAquick gel extraction kit	Qiagen
Pierce ECL Western Blot Substrate	Thermo Scientific

3.1.5 Plasmids

pET-Duet-1	two multiple cloning sites, N-terminal His_6-tag/S-tag, Amp^R (Merck)
pGEX-6P-1	N-terminal GST-tag, PreScission cleavage site, Amp^R, (GE Healthcare)
pGEX-4-T3	N-terminal GST-tag, thrombin cleavage site, Amp^R, (GE Healthcare, gift from Sascha Martens)
pSKB_LNB	modified pET28a plasmid (N-terminal His_6-tag; PreScission cleavage site, Kan^R) (cloned by D. Kühlmann)

3.1.6 Bacteria Strains

E. coli DH5a	gift from Stephen Marino
E. coli TG1	Promega
E. coli BL21 (DE3)	Novagen
E. coli Rosetta 2 (DE3)	Novagen

3.1.7 Media and antibiotics

Luria-Bertani (LB)	10 g/l Bactotryptone, 10 g/l NaCl, 5 mM NaOH, 5 g/l yeast extract
Minimal medium	1X M9 salt, 1X trace elements, 1mM $MgSO_4$, 0.3 mM $CaCl_2$, 2g/l glucose, 0.5 g/l NH_4Cl, 1.5 mg/l thiamin, 1.5 mg/l biotin (see 3.1.8 Buffers and solutions for stock composition)

Se-Met expression medium	Minimal medium containing 50 mg/l seleno-L-methionine, 50 mg/l L-valine, 50 mg/l L-leucine, 50 mg/l L-isoleucine, 100 mg/l L-threonine, 100 mg/l L-phenylalanine, 100 mg/l L-lysine
Terrific Broth (TB)	47.6 g TB powder, 4 ml 98% glycerol for 1 liter medium
Ampicillin 1000X	100 mg/ml in ddH_2O
Carbenicillin 1000X	100 mg/ml in ddH_2O
Chloramphenicol 1000X	34 mg/ml in 100 % ethanol
Kanamycin sulfate 1000X	50 mg/ml in ddH_2O

3.1.8 Buffers and solutions

10X TBE buffer	108 g/l TRIS-base, 55 g/l boric acid, 9.3 g/l NaEDTA pH 8.0
Lysis buffer	50 mM HEPES pH 7.5, 300 mM NaCl, 20 mM imidazole
Wash buffer	50 mM HEPES pH 7.5, 500 mM NaCl, 50 mM imidazole, 10 mM $MgCl_2$, 10 mM KCl, 1 mM ATP
Elution buffer 1	50 mM HEPES pH 7.5, 300 mM NaCl, 500 mM imidazole
Elution buffer 2	25 mM HEPES pH 7.5, 150 mM NaCl, 75 mM imidazole
Elution buffer 3	25 mM HEPES pH 7.5, 150 mM NaCl, 125 mM imidazole
Dialysis buffer	25 mM HEPES pH 7.5, 150 mM NaCl, 1 mM DTT
Size exclusion chromatography buffer	25 mM HEPES pH 7.5, 150 mM NaCl
NuPAGE MES SDS Buffer (20X)	Life Technologies
SDS-PAGE staining buffer	45 % ethanol, 10 % acetic acid
SDS-PAGE destaining buffer	45 % ethanol, 10 % acetic acid, 0.3 % (w/v) Coomassie R250

SPR protein dilution buffer	10 mM acetate buffer pH 3.8, 10 mM NaCl
SPR immobilization buffer	50 mM HEPES pH 7.5, 150 mM NaCl
SPR running buffer	50 mM Tris HCl pH 7.5, 150 mM NaCl
SPR regeneration buffer	10 mM glycine pH 2.1
100X trace elements	EDTA 5 g/l, $FeSO_4$ 0.5 g/l, $ZnCl_2$ 0.05 g/l, $CoSO_4$ 0.01 g/l, $CuCl_2$ 0.01g/l, H_3BO_3 0.01 g/l, $MnCl_2$ x $4H_2O$ 1.6 g/l, pH 7.0
Tris-buffered saline (TBS)	50 mM Tris HCl pH 7.5, 150 mM NaCl
Tris-buffered saline with Tween (TBS-T)	50 mM Tris HCl pH 7.5, 150 mM NaCl, 0.05 % (v/v) Tween20

3.1.9 Antibodies

Monoclonal anti-poly Histidine-Peroxidase antibody from mouse	Sigma-Aldrich

3.1.10 Crystallization screens

JBScreen Basics	Jena Bioscience
JBScreen Classic	Jena Bioscience
JBScreen JCSG++	Jena Bioscience
JBScreen PEG/Salt	Jena Bioscience
Anions suite	Qiagen
$AmSO_4$ suite	Qiagen
Classic I suite	Qiagen
Classic II suite	Qiagen
PACT suite	Qiagen
PEG suite	Qiagen
PEG II suite	Qiagen
pH Clear I suite	Qiagen

pH Clear II suite	Qiagen
Protein complex suite	Qiagen

3.1.11 Software and algorithms

Biacore T200 Evaluation Software 3.0	GE Healthcare
BioEdit	www.mbio.ncsu.edu/BioEdit/bioedit.html
CCP4 software package 7.0	Winn et al. 2011
ConSurf	Ashkenazy et al. 2016
Coot 0.8.3	Emsley et al. 2010
GraphPad Prism 7.05	GraphPad Software, Inc.
ImageJ	Schneider, Rasband, and Eliceiri 2012
MolProbity	Davis et al. 2007
OmniSec 5.0	Malvern Panalytics
PDBeFold	Krissinel and Henrick 2004
PHENIX 1.14	Adams et al. 2010
PISA	Krissinel and Henrick 2007
ProtParam	Gasteiger et al. 2005
PsiPred	Buchan et al. 2013
PyMOL 2.0	DeLano 2014
RockMaker 3.10.2.2	Formulatrix
SnapGene Viewer	GSL Biotech; snapgene.com
VasCo	Steinkellner et al. 2009
XDS	Kabsch 2010
XDSapp	Krug et al. 2012

3.2 Molecular biology methods

3.2.1 Agarose gel electrophoresis

1 % agarose gels were run at 80 V for 30 min to 50 min in TBE buffer.

3.2.2 DNA purification

Plasmid DNA was purified from bacterial cell lysates using the innuPREP plasmid mini kit according to the manufacturer's instructions. DNA was eluted in 30 µl ddH_2O and submitted to sequencing with the primer of interest.

DNA purification from agarose gels was performed using the QIAquick gel extraction kit according to the manufacturer's instructions.

3.2.3 Polymerase chain reaction (PCR)

DNA fragments were amplified using the KOD polymerase according to manufacturer's instructions. PCR products were separated on an agarose gel and purified using the QIAquick gel extraction kit.

3.2.4 Restriction digest

DNA was digested using enzymes from New England Bioscience according to the manufacturer's instructions in Cut Smart buffer. The digestion mix was supplemented with alkaline phosphatase (CIP) to prevent re-ligation.

3.2.5 Ligation

Prior to ligation, digested PCR products were treated with T4 polynucleotide kinase (PNK) according to the manufacturer's instructions. However, T4 ligase buffer was used instead of the PNK buffer. After DNA clean-up using the QIAquick gel extraction kit, ligation was performed with T4 DNA ligase according to the manufacturer's instructions. In brief, 0.06 pmol insert and 0.02 pmol of digested plasmid were incubated for 15 to 30 min at room temperature with T4 Ligase in T4 DNA ligase buffer.

3.2.6 Preparation of chemically competent *E. coli* cells

Preparation of chemically competent *E. coli* cells was performed according to Seidman and Struhl (1998) with minor modifications. In brief, 100 ml LB medium were inoculated with 1 ml of an overnight *E. coli* culture and grown until OD_{600} = 0.6 to 0.8. The cell suspension was transferred to two 50 ml falcon tubes and incubated on ice for 10 min. Cells were pelleted by centrifugation at 3,500 rpm for 10 min and resuspended in 5 ml ice cold 0.1 M $CaCl_2$, 10 % glycerol. After incubation on ice for 15 min, the cells were pelleted again and resuspended in 1 ml ice cold 0.1 M $CaCl_2$, 10 % glycerol. Aliquots were flash-frozen in liquid nitrogen and stored at -80°C. All consumables like tubes, tips or falcons were ice cold upon usage.

3.2.7 Transformation of chemically competent *E. coli* cells

25 µl of chemically competent *E. coli* cells were incubated with 1 µl (1 - 50 ng) of plasmid for 5 min on ice followed by a heat shock for 45 s at 42 °C. The cells were chilled on ice for 2 min before 200 µl of LB medium was added. After an incubation for 50 min at 37 °C and 800 rpm, cells were pelleted, resuspended in 80 µl LB medium and plated on agar plates containing the required antibiotics. For plasmid propagation, the cell lines *E. coli* DH5α or *E. coli* TG1 were used. For protein expression, plasmids were transformed into *E. coli* BL21 (DE3) or *E. coli* Rosetta2 (DE3).

3.2.8 Bacteria Storage

1 ml of a bacterial culture was supplemented with 50 % glycerol and stored at -80 °C.

3.2.9 Site-directed mutagenesis

Site-directed mutagenesis was carried out using the KOD polymerase according to manufacturer's instructions. Methylated template was subsequently digested with *Dpn*I at 37 °C for 1 h followed by heat inactivation. Occasionally, overlap extension PCR was employed for site-directed mutagenesis.

3.2.10 DNA sequencing

DNA sequencing was carried out by Source Bioscience (Berlin) or by LGC Genomics (Berlin) according to their respective protocols.

3.2.11 Constructs

Constructs used in this thesis are listed in Appendix A.

3.3 Biochemical methods

3.3.1 Sequence alignment

DNA sequences were aligned using ClustalW (Sievers et al., 2011).

3.3.2 Sodium dodecyl sulfate polyacrylamide gel electrophoresis (SDS-PAGE)

Proteins were subjected to SDS-PAGE on NuPAGE® Novex 4-12 % Bis-Tris gels with 1X MES running buffer in the Xcell Sure Lock system at 160 V for 40 to 50 min.

3.3.3 Protein expression

The plasmid of interest was transformed into chemically competent *E. coli* Rosetta2 (DE3) cells. 12 ml of a preculture grown in lysogeny broth (LB) supplemented with 100 µg/ml ampicillin and 34 µg/ml chloramphenicol containing the expression plasmid was used to inoculate 1 l of terrific broth (TB) with the required antibiotics and grown at 37 °C and 110 rpm until OD_{600} reached 0.5. Cultures were cooled to 18 °C before protein expression was induced using 200 µM isopropyl-ß-D-1-thiogalactopyranoside (IPTG). Cultures were grown for another 20 h at 18 °C and 110 rpm. Cells were sedimented by centrifugation for 20 min at 5,000 *g* and 4 °C, resuspended in 30 ml lysis buffer (50 mM HEPES pH 7.5, 300 mM NaCl, 10 mM imidazole, 1 mM $MgCl_2$) and stored at -20 °C until further use.

3.3.4 Purification of His_6-tagged proteins

All protein purification steps were performed on ice or at 4 °C. Resuspended cell pellets were thawed and incubated with 10 µg/ml DNase and 1 mM protease inhibitor 4-(2-aminoethyl)benzenesulfonyl fluoride hydrochloride (AEBSF) for 15 min before being mechanically disrupted using a microfluidizer. Cell debris was removed by centrifugation at 140,000 *g* for 45 min, the supernatant filtered (0.45 µm) and applied on a column packed with 1 ml to 5 ml Ni-NTA agarose previously equilibrated with 10 column volumes (CV) lysis buffer. The column was washed with 5 CV of lysis buffer

followed by 20 CV wash buffer (50 mM HEPES pH 7.5, 500 mM NaCl, 75 mM imidazole, 10 mM $MgCl_2$, 10 mM KCl, 1 mM ATP). Protein elution was performed using elution buffer 1 (50 mM HEPES pH 7.5, 300 mM NaCl, 500 mM imidazole). For over-night dialysis into size exclusion buffer (25 mM HEPES pH 7.5, 150 mM NaCl, 1 mM DTT), the protein was concentrated to 10 ml using an Amicon ultra centrifugal filter (30 KDa MWCO) and incubated at a molar ratio of 1:10 with TEV protease. On the next day, the protein solution was transferred to a 50 ml falcon tube and centrifuged at 5,000 *g* for 10 min to remove precipitates and applied on the Ni-NTA affinity chromatography column again. Elution was performed stepwise with elution buffers 2 and 3 (25 mM HEPES pH 7.5, 150 mM NaCl, 75 mM imidazole (2) or 125 mM imidazole (3)). Fractions containing untagged protein were pooled, concentrated to 0.5 - 1 ml and subjected to size exclusion chromatography on a Superdex S75 column. Peak fractions containing the pure protein of interest, as judged by SDS-PAGE, were pooled and concentrated, flash-frozen in liquid nitrogen and stored at -80 °C.

3.3.5 Purification of GST fusion proteins

All protein purification steps up to loading of the affinity column were performed as for His_6-tagged proteins. However, the cell pellet was initially resuspended in GST lysis buffer (50 mM HEPES pH 7.5, 300 mM NaCl). The filtered supernatant was loaded on a column packed with 5 ml Glutathione Sepharose 4B and equilibrated with 10 CV GST lysis buffer. After washing the column with 20 CV of GST wash buffer (50 mM HEPES pH 7.5, 500 mM NaCl, 10 mM $MgCl_2$, 10 mM KCl, 1 mM ATP), the protein was eluted with freshly prepared GST elution buffer (50 mM HEPES pH 7.5, 300 mM NaCl, 10 mM reduced glutathione). As no tag cleavage was required, the protein was directly concentrated to 0.5 – 1 ml and applied on a Superdex S200 column. Peak fractions containing the pure protein of interest, as judged by SDS-PAGE, were pooled and concentrated, flash-frozen in liquid nitrogen and stored at -80 °C.

3.3.6 Expression and purification of seleno-L-methionine labelled protein for crystallization

The expression of seleno-L-methionine labelled protein was adapted from a previously published protocol (Doublié, 1997). 250 ml LB supplemented with

100 µg/ml ampicillin and 34 µg/ml chloramphenicol were inoculated with the expression clone and incubated overnight at 30 °C and 180 rpm. Cells were harvested by centrifugation for 20 min at 5000 *g* and washed with minimal medium three times before inoculation of 1 l minimal medium containing the respective antibiotics. Cells were incubated at 37 °C and 115 rpm until the OD_{600} reached 0.6. The culture was supplemented with an amino acid cocktail comprising the L-amino acids 100 mg/l lysine, 100 mg/l phenylalanine, 100 mg/l threonine, 50 mg/l isoleucine, 50 mg/l leucine, 50 mg/l valine and 50 mg/l seleno-L-methionine and incubated an additional 15 min before expression was induced using 200 µM IPTG. Cultures were grown for 20 h at 18 °C and 115 rpm.

3.3.7 Determination of protein concentration

Protein concentrations were determined at λ = 280 nm using the NanoDrop 2000 or NanoDrop One. Molecular weights and extinction coefficients ε were calculated using ProtParam (Gasteiger et al., 2005).

3.3.8 Right-angle light scattering

100 µl of a 3 mg/ml FIP200 CTR solution were applied on a Superdex S75 10/300 size exclusion chromatography column coupled to a right-angle light scattering (RALS) refractive index detector. The running buffer contained 25 mM HEPES pH 7.5 and 150 mM NaCl. Data were analyzed with the OmniSec Software.

3.3.9 Isothermal titration calorimetry (ITC)

Isothermal titration calorimetry was carried out at 10 °C, except for the titration of hexathymidine (dT_6) into FIP200 CTR, which was performed at 20 °C. Proteins were dialyzed into 25 mM HEPES pH 7.5, 150 mM NaCl overnight before running ITC experiments. Titrations comprised 19 injections of 2 µl. Details on concentrations used can be found in the respective figures. Data were collected using MicroCal PEAQ ITC and analyzed with the MicroCal PEAQ ITC Analysis Software.

3.3.10 Surface plasmon resonance spectroscopy (SPR)

All SPR experiments were performed on a Biacore T200 instrument at 25 °C in 50 mM Tris HCl pH 7.5, 150 mM NaCl. GST, GST-p62 FIR wt, GST-p62 FIR LIRmut, and GST-p62 FIR 4P were diluted in 10 mM acetate buffer pH 3.8, 10 mM NaCl and

immobilized on a CM 5 Series S sensor chip using the Amine Coupling Kit and 50 mM HEPES pH 7.5, 150 mM NaCl as the immobilization buffer. By coupling the proteins to a theoretical R_{max} of approximately 6,000 RU, high density immobilization was achieved. After three conditioning cycles with 30 µM FIP200 CTR and regeneration in 10 mM glycine pH 2.1, FIP200 CTR was passed over the four flow channels at a flow rate of 30 µl/min. Single-cycle data were recorded for a three-fold dilution series of FIP200 CTR (0.4 µM – 30 µM) with GST-p62 FIR wt: n=3, GST-p62 FIR 4P: n=5, and GST-p62 FIR LIRmut: n=3; and two technical replicates for each run. Association of FIP200 CTR was monitored for 180 s, followed by dissociation in buffer for 70 s. After each cycle, remaining FIP200 CTR was stripped off the surface with two 60 s injections of 10 mM glycine pH 2.1. A new chip was used for each of the independent experiments. The same procedure was applied in experiments involving FIP200 R1573D or FIP200 Claw. Evaluation was performed using the Biacore T200 Evaluation Software 3.0. Data were double referenced by subtracting the GST and buffer control signals. Data points at equilibrium were fitted globally with a one site binding model (Response = R_{max} x [protein]/($K_D$app + [protein]), where R_{max} is the fitted maximal binding capacity and $K_D$app the apparent dissociation constant, using GraphPad Prism.

3.3.11 Liposome preparation

Lipid extract from bovine brain (Folch Fraction I, Sigma Aldrich) was dissolved to 500 mg/ml in chloroform and stored at -80°C (Folch lipids). 500 µg of Folch lipids were dissolved in a chloroform:methanol mix (1:0.3 v/v), subsequently dried under an argon stream and stored in a desiccator overnight. The next day, 250 µl of liposome buffer (25 mM HEPES pH 7.5, 150 mM NaCl) was added to the dried liposomes to reach a final concentration of 2 mg/ml. Liposomes were incubated at room temperature for 90 – 120 min to allow for swelling before use. Extrusion was performed by passing the liposome suspension 13 times through a 0.1, 0.4 or 1.0 µm filter membrane.

3.3.12 Liposome co-sedimentation assay

1 mg/ml Folch liposomes were incubated with 10 µM protein for 10 min at room temperature in a 50 µl reaction volume. To sediment liposomes and bound protein,

ultracentrifugation was performed for 30 min at 214,000 *g* in a TLA-100 rotor. The supernatant was mixed with 5X SDS-PAGE sample buffer and the pellets dissolved in 1X SDS-PAGE sample buffer. 6 µl of each sample were applied on a 15-well SDS-PAGE gel. For quantification, data from multiple independent experiments were analyzed using ImageJ (FIP200 CTR wt: n=9, FIP200 CTR R1514D/ K1541D/ R1551D/ R1573D n=6, FIP200 CTR K1575D, FIP200 Claw wt or R1573D n=3).

3.3.13 Peptide array

Peptide SPOT synthesis was performed on an Intavis ResPep-SL device by Kerstin Zühlke (Max Delbrück Center, Berlin) according to Hundsrucker et al. 2006. The PVDF membrane was briefly activated in ethanol and rinsed with water and TBS-T (50 mM Tris HCl pH 7.5, 150 mM NaCl, 0.05 % (v/v) Tween20) before blocking with TBS-T containing 5 % (w/v) skim milk powder (SMP) for 1 h at room temperature. The membrane was then incubated overnight with 56 µM His_6-tagged FIP200 CTR in 5 % (w/v) SMP/TBS-T or with buffer lacking protein (control) at 4°C. The next day, the membrane was washed with 3 times for 5 min in TBS-T before being incubated with a monoclonal anti-polyHistidine-peroxidase antibody from mouse (1:2000 in 5 % (w/v) SMP/TBS-T) for 1 h at room temperature. Chemiluminescence detection was performed after washing the membrane 3 times 5 min in TBS-T.

3.3.14 Microscopy-based protein-protein interaction assays

The following protocol was established and performed by Eleonora Turco and Sascha Martens (MFPL, Vienna) and has been published in Turco et al. 2019.
GST-p62 FIR mutants (4 mg/ml) were incubated for 30 min at 4 °C with Glutathione Sepharose 4B beads. The beads were washed two times with washing buffer (25 mM HEPES pH7.5, 150 mM NaCl, 1 mM DTT) in 10X beads volume and subsequently resuspended in washing buffer (1:1). 10 µL of a 2-5 µM solution of GFP-FIP200 CTR and mutants were added to the beads suspension and incubated for 30 min to 1 h at room temperature or at 4 °C before imaging with a Zeiss LSM700 confocal microscope or a Visitron spinning disk microscope with a 20X magnification. Data of three independent experiments were quantified with ImageJ. For each sample, the GFP intensity was normalized to the signal of GFP-FIP200 CTR wt on GST-p62 FIR 4P coated beads.

3.3.15 p62 aggregation assay

The p62 aggregation assay and quantification were performed by Eleonora Turco as described previously (Zaffagnini et al., 2018) and have been published in Turco et al. 2019. 20 µM GST-4x ubiquitin was added to a protein mixture of 20 µM GFP-FIP200 CTR (wt or R1573D, F1574A, F1574W and R1584A mutants) and 2 µM mCherry-p62 wt. Aggregate formation was monitored over time using a Visitron inverse spinning disk microscope equipped with a Yokogawa CSU-X1 spinning disk, a standard CCD camera (CoolSNAP HQ^2), 561nm DPSS laser (100mW, AOTF-controlled) and LD Achroplan 20x/0.4 Corr objective. Images were taken every 30 s for 30 min. For the GFP-FIP200 CTR recruitment to preformed aggregates, mCherry-p62 (2 µM) and GST-4x ubiquitin (10 µM) were incubated for 30 min at room temperature to allow aggregate formation. 1 µM GFP-FIP200 CTR (wt or mutants) was added and images were taken after 30 min incubation at room temperature with a Zeiss LSM 700 confocal microscope with 63x magnification.

3.4 Protein crystallization and structure determination

3.4.1 Crystallization of FIP200 CTR

Initial crystallization screening was carried out in the 96-well sitting drop setup using the vapor-diffusion method. 200 nl of protein were mixed with 200 nl of reservoir solution by a Gryphon dispensing robot and equilibrated against 80 µl of reservoir at 4 °C and 20 °C in the Rock Imager storage system. Commercial screens utilized for initial screening are listed in Section 3.1.10. The initial crystallization condition for native protein was identified using the Qiagen pHClear II suite. Rod-shaped crystals grew within 7 days in 0.1 M MES pH 6.0, 1.0 M LiCl and 10 % PEG 6000. Optimization of native protein crystals was performed in hanging drops on 24-well plates. The reservoir contained a volume of 1 ml and the drops were composed of 1 µl or 2 µl protein (27 mg/ml) and 1 µl reservoir (see Table 2, page 48). Rod-shaped single crystals grew within 24 h to 72 h at 20 °C in 0.1 M MES pH 6.0, 13-15% PEG 6000, 0.8 – 1.2 M LiCl.

Crystals with seleno-L-methionine labelled protein were grown in the 96-well sitting drop setup at 20 °C and similar crystallization conditions (0.1 M MES pH 6.0,

8-11% PEG 6000, 1.0 – 1.2 M LiCl, 10 mM DTT). Crystals were cryo-protected in reservoir supplemented with 10 % glycerol and cryo-cooled in liquid nitrogen.

3.4.2 Data collection and processing

Data sets were collected at beamline BL14.1, BESSY II, Berlin, Germany (Mueller et al., 2015) equipped with a Pilatus 6M detector. 1,000 images were collected at 2 s exposure time and a rotation increment of 0.1° at -173 °C for native protein crystals. For seleno-L-methionine labelled protein crystals, 14,400 images were collected at 0.3 s exposure time and a rotation increment of 0.1° at -173 °C. Data for crystals of native protein were collected at a wavelength of 0.9184 Å and for seleno-L-methionine labelled protein crystals at 0.9796 Å. Data was indexed, integrated and scaled using XDS (Kabsch, 2010) or XDSAPP (Krug et al., 2012). Data collection and processing was performed by Tobias Bock-Bierbaum (Max Delbrück Center, Berlin).

3.4.3 Phase determination and refinement

The phase problem was solved using single-wavelength anomalous diffraction (SAD) data collected at the Se-K-edge. Location of anomalous scatterers, generation of experimental phases and density modification was performed using the *Autosol* routine of PHENIX (Adams et al., 2010). Iterative model building and refinement were done with Coot (Emsley et al., 2010) and PHENIX. Initial rigid body refinement was followed by cartesian refinement using the maximum likelihood function. Secondary structure restraints and group B-factors with two groups per residue were employed. Non-crystallographic symmetry (NCS) and translation-libration-screw-rotation (TLS) were applied with two groups per chain (helix and Claw domain, linker excluded).
The final structure was obtained from data of a native protein crystal that diffracted better compared to the seleno-L-methionine crystal. To this end, molecular replacement with the initial structure model from the seleno-L-methionine data was employed. Refinement was performed as described above.

3.4.4 Structure analysis and figure preparation

Structure validation was carried out using MolProbity (Davis et al., 2007). The lipophilic surface potential was calculated with the PyMol-plugin VASCo (Steinkellner et al., 2009) and the conservation plot using ConSurf (Ashkenazy et al., 2016).

The dimer interface was analyzed with the PISA server (Krissinel and Henrick, 2007). Figures were prepared with PyMol 2.0 (DeLano, 2014) and Adobe Illustrator. Coordinates and diffraction data have been deposited in the Protein Data Bank (PDB) with accession code 6GMA.

3.5 Cell biology methods

The following cell biology protocols were designed and performed by Eleonora Turco and colleagues (MFPL, Vienna) and have been published in Turco et al. 2019.

3.5.1 Pull-downs from HeLa and HAP1 cell lysates

HeLa or HAP1 cells were seeded into four 10 cm dishes and grown until confluence. Cells were harvested with trypsin and washed with PBS. The cell pellet was resuspended in 100 µl of 20 mM HEPES pH 7.5, 250 mM sorbitol, 0.5 mM EGTA, 5 mM Mg-Acetate, 0.3 mM DTT, cOmplete EDTA-free protease inhibitor cocktail and cells were lysed by one freeze and thaw cycle. After 10 min centrifugation at 1,000 *g* protein concentration in the supernatant (lysate) was measured by Bradford protein assay. 10 µl of Glutathione Sepharose 4B or GFP-Trap®_A beads (GE-Healthcare and Chromotek, respectively) were incubated with 4 mg/ml of bait protein (GST-FIP200 CTR or GFP-FIP200 CTR wt/mut) for 30 min at 4 °C. Beads were washed 2 times with 10X beads volume in 25 mM HEPES pH 7.5, 150 mM NaCl, 1 mM DTT and subsequently resuspended in 10 µl of that buffer. 200 µg (300 µg for HAP1) of cell lysate were added to the beads and incubated for 1 h at 4 °C. Beads were washed 3 times in 10X beads volume of wash buffer and resuspended in 10 µl wash buffer. Proteins bound to the beads were eluted by boiling for 5 min at 98 °C in SDS-PAGE buffer. 5 µl of each sample were analyzed by Western blotting with mouse anti-p62 (1:3000, BD Bioscience). Other 5 µl of the samples were analyzed by SDS-PAGE followed by Coomassie staining or Western blot with mouse anti-GST (1:1000, Sigma Aldrich) to visualize the bait protein input. For the pull-down with HAP1 cells lysates, the entire eluate was analyzed by Western blot and Ponceau staining of the membrane was used to visualize the bait protein input.

3.5.2 Co-immunoprecipitation from HeLa cells

HeLa cells were seeded in 10 cm dishes and let grow until 80% confluency. Cells were transfected with pME18s vectors (Addgene) containing HA-FIP200 (wt, point mutants or truncation) using Fugene transfection reagent (Promega). A vector:Fugene ratio of 1:6 was used for transfection. 24 h after transfection, cells were harvested with trypsin. The cell pellet was washed in PBS and resuspended in 100 µl of 20 mM HEPES pH 7.5, 250 mM Sorbitol, 0.5 mM EGTA, 5 mM Mg-Acetate, 0.3 mM DTT, cOmplete EDTA-free protease inhibitor cocktail (Roche). After 1 freeze and thaw cycle, the lysate was clarified by spinning at 1,000 *g* for 10 min at 4 °C. Protein concentration in the lysates was measured by Bradford assay (BioRad) and all samples were adjusted to the same final concentration in 300 µl IP buffer (25 mM HEPES pH 7.5, 125 mM NaCl, 0.05% Triton X-100). Anti-HA magnetic beads (Pierce – Thermo Scientific) were washed 3 times in IP buffer and 1.5 µl of beads slurry were incubated with each sample for 1 h at 4 °C on rotating wheel (9 rpm). After 3 x 5 min washed in IP buffer, beads were resuspended in 10 µl of 2X non-reducing protein loading dye and heated for 10 min at 95 °C. Samples were analyzed by Western blot with mouse anti-p62 (1:500 – BD Bioscience) and rabbit anti-FIP200 (1:1000 – Atlas antibodies).

3.5.3 Generation of HeLa FIP200ΔClaw cell line

To generate HeLa FIP200ΔClaw cells, sgRNA targeting the region around R1591 of FIP200 were cloned into pSpCas9(BB)-2A-GFP (PX458) vector (Addgene). HeLa cells were transfected with the vector containing the sgRNA and after 48 h, GFP-Cas9 expressing cells were sorted by FACS into 96-well plates. Deletion of the Claw domain in the selected clones was confirmed by Western blotting and sequencing of the genomic region.

3.5.4 Immunocytochemistry

For immunocytochemistry analysis, cells were grown on glass cover slips (Ø 12 mm, high precision, Marienfeld-superior) and fixed with 4 % (w/v) paraformaldehyde in PBS for 20 min at room temperature. Cells were permeabilized in 0.25% Triton-X100 for 15 min at room temperature. After two washes in PBS, cover slips were incubated for 30 min at room temperature in blocking buffer (1% BSA in PBS), transferred into

a humid chamber and incubated with primary antibodies diluted in 1% BSA in PBS for 1 h at 37°C (FIP200-p62 immunostaining) or 16 h at 4°C (rabbit anti-FIP200 1:200 – Cell Signaling, mouse anti-p62 1:200 – BD Bioscience). Coverslips were then washed 3 times for 5 min in PBS and incubated with secondary antibodies (goat anti-mouse Alexa Fluor 488 1:1000 – Invitrogen, goat anti-rabbit Alexa Fluor 647 1:500 – Jackson Immunoresearch). After 3 x 5 min washes in PBS, coverslips were mounted on glass slides using DAPI Fluoromont-G™ (Southern Biotech). Imaging was performed on an inverted confocal laser scanning microscope Zeiss LSM 700, Plan-Apochromat 63x/1.4 Oil DIC or Plan-Apochromat 40x/1.3 Oil DIC. To prevent cross-contamination between fluorochromes, each channel was imaged sequentially using the multitrack recording module before merging. Images from fluorescence and confocal acquisitions were processed and analyzed with ImageJ software.

4. Results

4.1 Protein expression and purification

4.1.1 Expression and purification of FIP200 CTR

Sascha Martens and his team (MFPL, Vienna) showed that a C-terminal fragment of FIP200 comprising residues 1458 - 1594 (FIP200 CTR) was sufficient to bind to p62. For structural characterization of this fragment, a purification protocol was established. His_6-tagged FIP200 CTR was expressed in *E. coli* and purified via affinity chromatography (section 3.3.3 and 3.3.4). Following elution, the protein was cleaved with TEV protease. Since cleavage was not always complete, tagged protein as well as the His_6-tag itself and the TEV-protease were eliminated via a reverse Ni-NTA chromatography step. Size exclusion chromatography yielded homogenous and pure protein, as confirmed by SDS-PAGE and UV-absorption at 254 nm and 280 nm (Figure 14A, B). Expression and purification of other FIP200 constructs and mutants were performed similarly (see Appendix A - Constructs). Typical yields were around 5 mg per liter of bacterial culture.

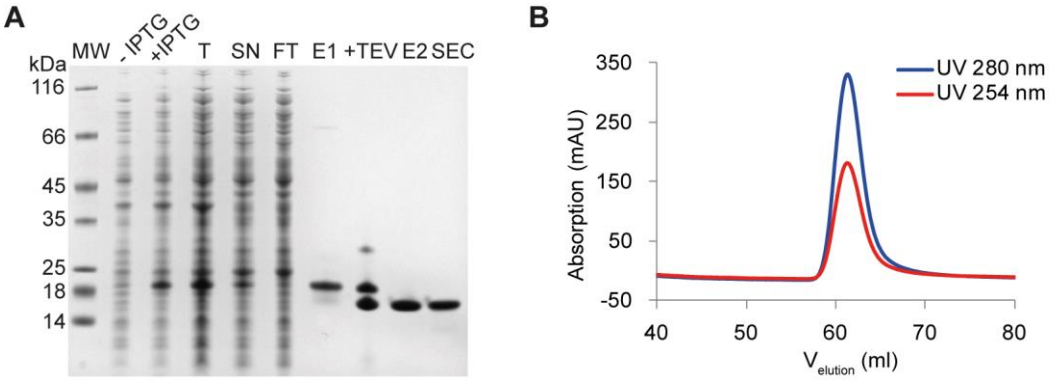

Figure 14. Purification of FIP200 CTR. (A) SDS-PAGE showing expression (-IPTG/+IPTG), solubility (T - Total, SN – supernatant) and purification of FIP200 CTR. FT – Flow Through, E1 – Elution from Ni-NTA resin, +TEV – sample after TEV protease cleavage, E2 – reverse Ni-NTA elution, SEC – final protein after size exclusion chromatography; MW – molecular weight (B) Size exclusion chromatography elution profile of FIP200 CTR on a Superdex S75 16/600 column.

4.1.2 Expression and purification of GST-p62 FIR variants

In addition to FIP200 CTR, the p62 cargo receptor was purified to study the interaction with FIP200 CTR *in vitro*. GST-fused p62 FIR wildtype (wt) and variants thereof (see section 1.7) were expressed in *E. coli* and purified via a glutathione sepharose column followed by size exclusion chromatography (SEC) as described in sections 3.3.3 and 3.3.5. This purification protocol yielded pure protein for all GST-p62 constructs, as shown for GST-p62 FIR 4P in Figure 15. Typical yields were 30 mg per liter of bacterial culture.

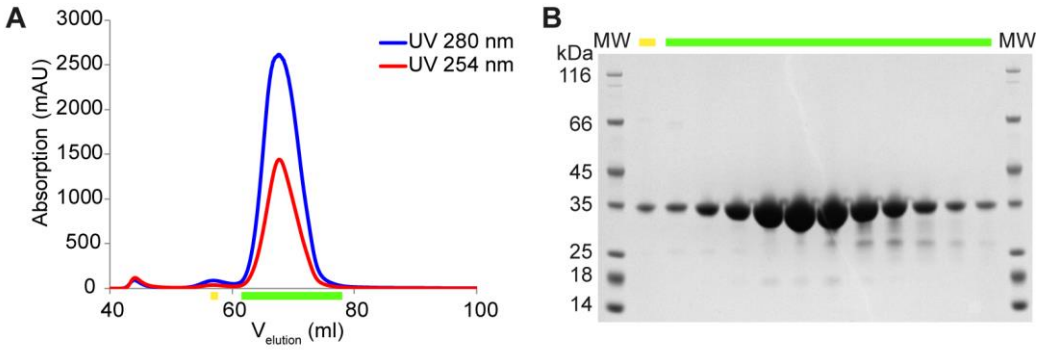

Figure 15. Size exclusion chromatography of GST-p62 FIR 4P on a Superdex S200 16/600 column. A) Elution profile and B) SDS-PAGE of indicated fractions (yellow and green bars, MW – molecular weight).

4.2 Crystallization and structure determination of FIP200 CTR

4.2.1 Crystallization of FIP200 CTR

To obtain structural insights into FIP200 CTR, crystallization was carried out according to section 3.4.1. Crystallization of a FIP200-p62 complex was also attempted and is described in more detail in section 4.9.1. A single crystal of FIP200 CTR grew after two weeks in 0.1 M MES pH 6.0, 10 % PEG 6000, 1.0 M LiCl (pHClear screen). Optimization of the initial hit yielded crystal clusters of native FIP200 CTR that grew within 12 to 36 h at 20 °C. Single crystals with sizes ranging from 50 µm to 250 µm were obtained by further optimization of precipitant and salt concentration, protein concentration, drop volume and protein - reservoir drop ratio.

Native crystals diffracted to a resolution of 3.2 Å and belonged to space group $P2_12_12$ with cell dimensions of a = 92.0, b = 187.2, c =55.3 Å, α = ß = γ =90° (Figure 16A, B; Table 3). An overview of the crystallization conditions is given in Table 2.

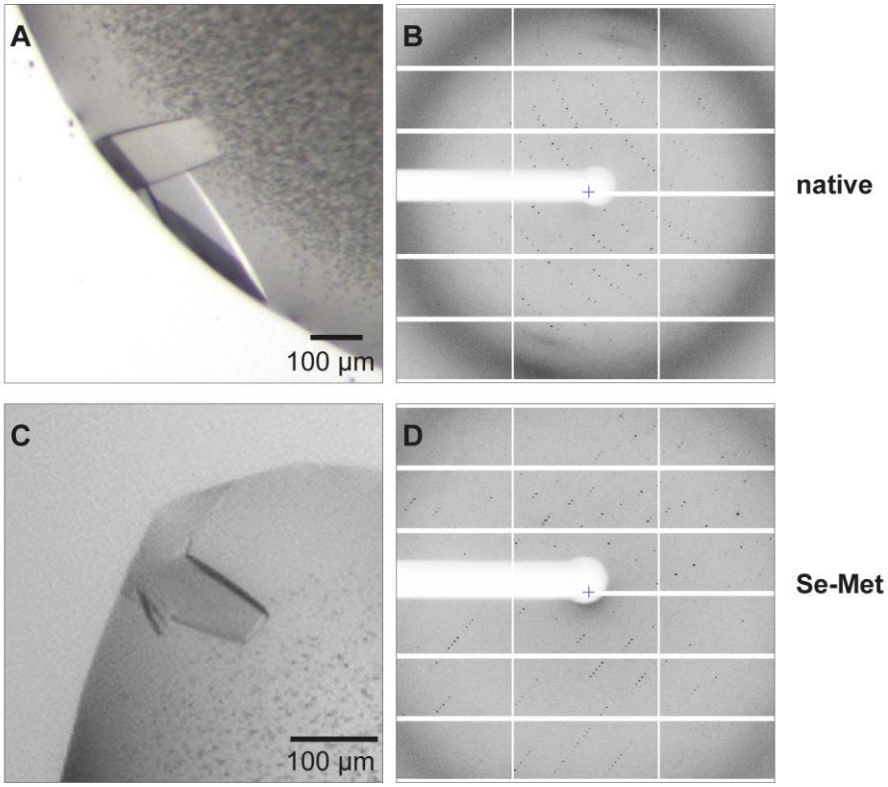

Figure 16. FIP200 CTR crystals and selected diffraction images. (A) Native protein crystals grown in 0.1 M MES pH 6.0, 13-15% PEG 6000, 0.8 – 1.2 M LiCl and (B) diffraction image for one of those crystals. (C) Se-Met protein crystals grown in 0.1 MES pH 6, 1.2 M LiCl, 7% PEG 6000, 1 mM DTT and (D) diffraction image for that crystal. Experiments were performed by Tobias Bock-Bierbaum (Max Delbrück Center, Berlin) with constructs and purification protocols from me.

As no molecular model was available allowing for structure solution by molecular replacement, seleno-L-methionine labelled (Se-Met) protein was expressed and purified to homogeneity (see section 3.3.6) to apply experimental phasing by single anomalous diffraction (SAD). Se-Met protein crystals grew in similar conditions to the native crystals. However, DTT improved crystallization and only half of the precipitant concentration was required to grow crystals of 30 µm to 150 µm (Figure 16C). These derivatized crystals were isomorphous to the native ones, belonging to space group $P2_12_12$ with cell dimensions of

a = 92.5, b = 188.7, c = 55.7 Å, $\alpha = ß = \gamma = 90°$ (Figure 16D). Crystallization was performed by me and Tobias Bock-Bierbaum (Max Delbrück Center, Berlin).

Table 2. Crystallization conditions

	native	**Se-Met**
Method	Hanging drop vapor diffusion	Sitting drop vapor diffusion
Plate type	24-well	96-well
Temperature	20 °C	20 °C
Protein concentration	27 mg/ml	27 mg/ml
Buffer composition of protein solution	25 mM HEPES pH 7.5, 150 mM NaCl	25 mM HEPES pH 7.5, 150 mM NaCl
Composition of reservoir solution	0.1 M MES pH 6.0, 13-15% PEG 6000, 0.8 – 1.2 M LiCl	0.1 MES pH 6.0, 1.2 M LiCl, 7% PEG 6000, 1 mM DTT
Volume and ratio of drop	3 µl, 2:1	0.4 µl, 1:1
Volume of reservoir	1000 µl	80 µl

4.2.2 Data collection and phasing

In order to obtain anomalous differences for structure determination, low dose and high redundant data were collected at the Se-K-edge (12.6565 keV) (Table 3) by Tobias Bock-Bierbaum (Max Delbrück Center, Berlin) according to section 3.4.2. Two datasets with a total rotation range of 720° were merged with XSCALE (Kabsch, 2010), resulting in a redundancy of 25. Although the crystals only diffracted to 3.5 Å, they showed a significant anomalous signal up to 4.1 Å. Analysis of the crystal content revealed a high probability for six molecules per asymmetric unit (solvent content of 51.3 % and Matthews coefficient $V_M = 2.5$), resulting in a total of 24 selenium sites per asymmetric unit. Using *AutoSol* from the PHENIX package (Adams et al., 2010),

22 of these sites were successfully located (see section 3.4.3). An interpretable experimental electron density was obtained, allowing for model building and refinement (Figure 17). Additionally, data for a native protein crystal diffracting to a higher resolution were collected.

Table 3. Data collection and processing statistics

	native	**Se-Met**
Diffraction source	BESSY II BL14.1	BESSY II BL14.1
Wavelength (Å)	0.9184	0.9796
Temperature (K)	100	100
Detector	Pilatus 6M	Pilatus 6M
Detector distance (mm)	421	505
Rotation range per image (°)	0.1	0.1
Total rotation range (°)	100	1440
Exposure time per image (s)	2	0.3
Space group	P 2_12_12	P 2_12_12
a, *b*, *c* (Å)	92.05 187.17 55.34	92.46 188.68 55.74
α, β, γ (°)	90 90 90	90 90 90
Mosaicity (°)	0.103	0.095
Resolution range (Å)	47.64-3.17 (3.36-3.17)	50.00 – 3.45 (3.54 -3.45)
Total No. of reflections	60,256 (9914)	692,962 (46,434)
No. of unique reflections	16,476 (2,667)	24,784 (1,820)
Completeness (%)	97.1 (98.4)	100 (99.9)
Redundancy	3.7 (3.8)	24.9 (25.5)
$\langle I/\sigma(I)\rangle^{\#}$	11.02 (0.56)	19.74 (1.88)
$R_{\text{meas.}}$	8.1 (230.3)	12.6 (209.7)
$CC_{1/2}$	99.9 (23.9)	99.9 (81.2)
Overall *B* factor (Å^2)	119.7	120.6

Values for the outer shell are given in parentheses.
$CC_{1/2}$ was used as a cutting criterion for the native data set and included reflections until 3.17 Å. $\langle I/\sigma(I)\rangle$ of 2 would be reached at a resolution of 3.40 Å.

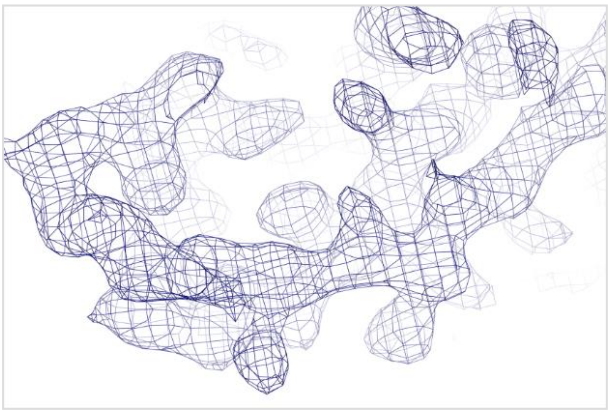

Figure 17. SAD-phased density modified electron density map ($2mF_o$-DF_c) of Se-Met FIP200 CTR contoured at 1 σ.

4.2.3 Model building and refinement

The protein model was built and refined according to section 3.4.3. Because of significant differences in the quality of the electron density map among the six molecules in the asymmetric unit, only the model for the best-defined molecule was built. This model was applied as a search model for molecular replacement and successfully placed five times in the remaining density of the asymmetric unit by rigid body refinement. Secondary structure restraints and group B-factors with two groups per residue were employed. For NCS and TLS, two groups per chain were used. The final structure was obtained from data of a native protein crystal that diffracted better compared to the Se-Met protein crystal. To this end, molecular replacement with the initial structure model from the seleno-L-methionine data was employed.

The final model shows reasonable R_{work}/R_{free} values of 26.7%/29.5%. Validation of the structure using MolProbity (Davis et al. 2007, implemented in PHENIX) confirmed the overall correct geometry. For example, backbone torsion angle analysis, for example, showed 95.3 % of the amino acids in the favored and 0 % in the outlier region of the Ramachandran plot (Figure 18). Refinement statistics are summarized in Table 4.

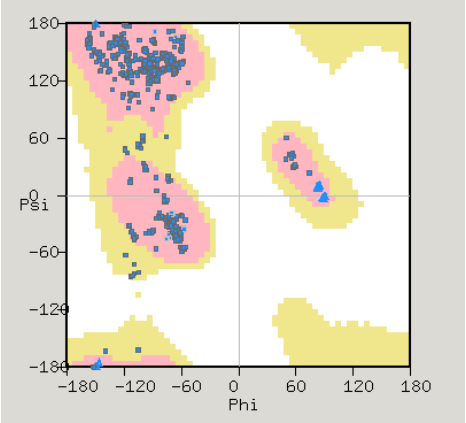

Figure 18. Ramachandran plot of the FIP200 CTR structure. 95.2 % of the residues have favored psi and phi angles (red region), while 4.8 % have allowed angles (yellow region). There are no psi and phi angle outliers (white region) Plot from Coot (Emsley et al., 2010).

Table 4. Refinement statistics

	native
Resolution (Å)	37.76 – 3.20
No. of reflections	15,973
R_{work}/R_{free} (%)	26.7/29.5
Mol/asymmetric unit	6
No. of protein atoms	5,956
B factors protein (Å^2)	154
Ramachandran plot	
favoured (%)	95.2
allowed (%)	4.8
outliers (%)	0
rms deviations	
Bond lengths (Å)	0.004
Bond angles (°)	0.820

4.3 The crystal structure of FIP200-CTR

4.3.1 Overall structure of FIP200 CTR

The FIP200 CTR monomer is composed of an N-terminal helix that is connected to a C-terminal ß-sheet via a flexible linker (Figure 19A). The ß-sheet contains three loops located on one side of the sheet in such a way, that the globular domain resembles a hand with flexed fingers. Therefore, it was termed the "Claw domain" (Figure 19B). The topology plot of the FIP200 CTR structure shows that the Claw domain features, besides its mostly antiparallel six-stranded ß-sheet, also a short α-helix located between ß-strand 3 and ß-strand 4 (Figure 19C). For analysis of the Claw domain fold, please refer to section 4.4.

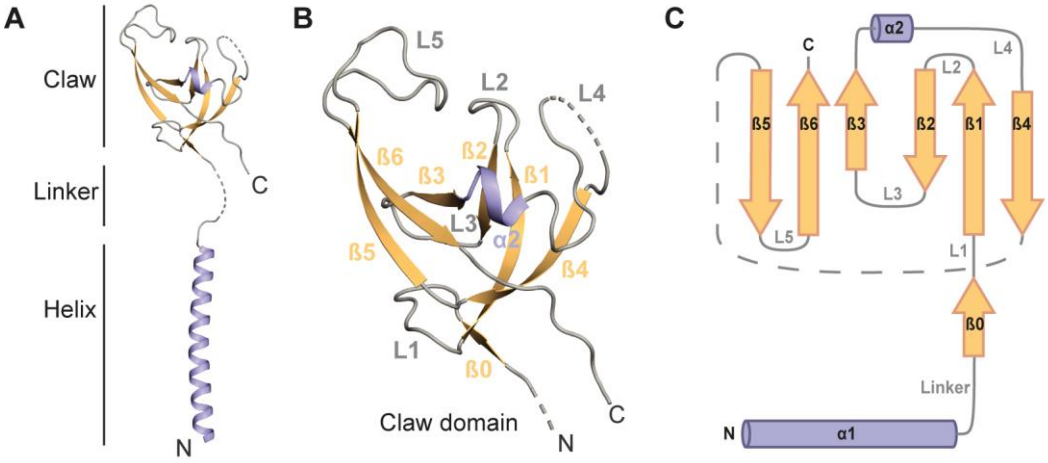

Figure 19. Structure of monomeric FIP200 CTR. A) Crystal structure of the FIP200 CTR monomer. The molecule is composed of a helix, a linker and a globular Claw domain. The structure is colored according to its secondary structure elements (helix – purple, ß-strands - orange, loops - gray). B) Close-up of the globular Claw domain. The fold resembles a Claw with the ß-sheet being the palm of the Claw and loops L2, L4 and L5 flexed fingers. Same view as in A), with labeled secondary structure elements. C) Topology plot of monomeric FIP200 CTR with α-helices shown as purple cylinders and ß-strands as orange arrows.

4.3.2 FIP200 CTR assembly in the crystal lattice

To identify possible multimeric species of FIP200, the assembly of the molecule in the crystal lattice was analyzed. The asymmetric unit (asu) of the crystal contains six molecules of FIP200 CTR that form three dimers (Figure 20A). The dimers interact with each other via their N-terminal α-helices. Dimer 2 and dimer 3 also form closer contacts via their Claw domains and hence assemble as crystallographic tetramers.

In the crystal lattice, the Claw domains of dimer 1 (chain A and B) interact with the helices of dimer 2 (Figure 20B, red circle). Especially chain A is further stabilized by crystal contacts with the N-terminal part of dimers 2 and 3 (Figure 20B, black circle). In contrast, the Claw domains of dimer 2 and 3 are stabilized only by crystal contacts with the helices of another dimer, which makes them more flexible. The different levels of Claw domain flexibility are reflected in the quality of the respective electron density maps (Figure 20C). While for chain A (dimer 1, top left), secondary structure elements as well as side chains are well defined, chain C (dimer 2, top right) lacks information on individual side chains; for chain E (dimer 3, bottom), backbone density is not continuous. Due to the unstructured linker, the globular Claw domain also shows flexibility with respect to the helices (Figure 20D). Still, there is a high structural similarity within the six different Claw domains with a root mean square deviation (RMSD, C-alpha atoms only) of 0.33 Å (Figure 20E). Taken together, FIP200 assembles as a dimer, consistent with the single species seen in size exclusion chromatography profiles (compare to Figure 14B). Flexibility of the molecules within the crystal lattice probably caused rather weak diffraction and varying quality of the electron density among the six different molecules of the asu.

The electron density of the linkers is missing for dimer 1 (Figure 21A) and dimer 3. However, it is defined for dimer 2 (Figure 21B) because of crystal contacts between the helix of chain C in dimer 2 and the Claw domains of dimer 1 (Figure 21C). This crystal contact has already been described above in stabilizing the Claw domains of dimer 1 (red circle). According to the helix-Claw connectivity in dimer 2, the Claw domains are arranged in a criss-cross manner with respect to the helices in all of the three dimers.

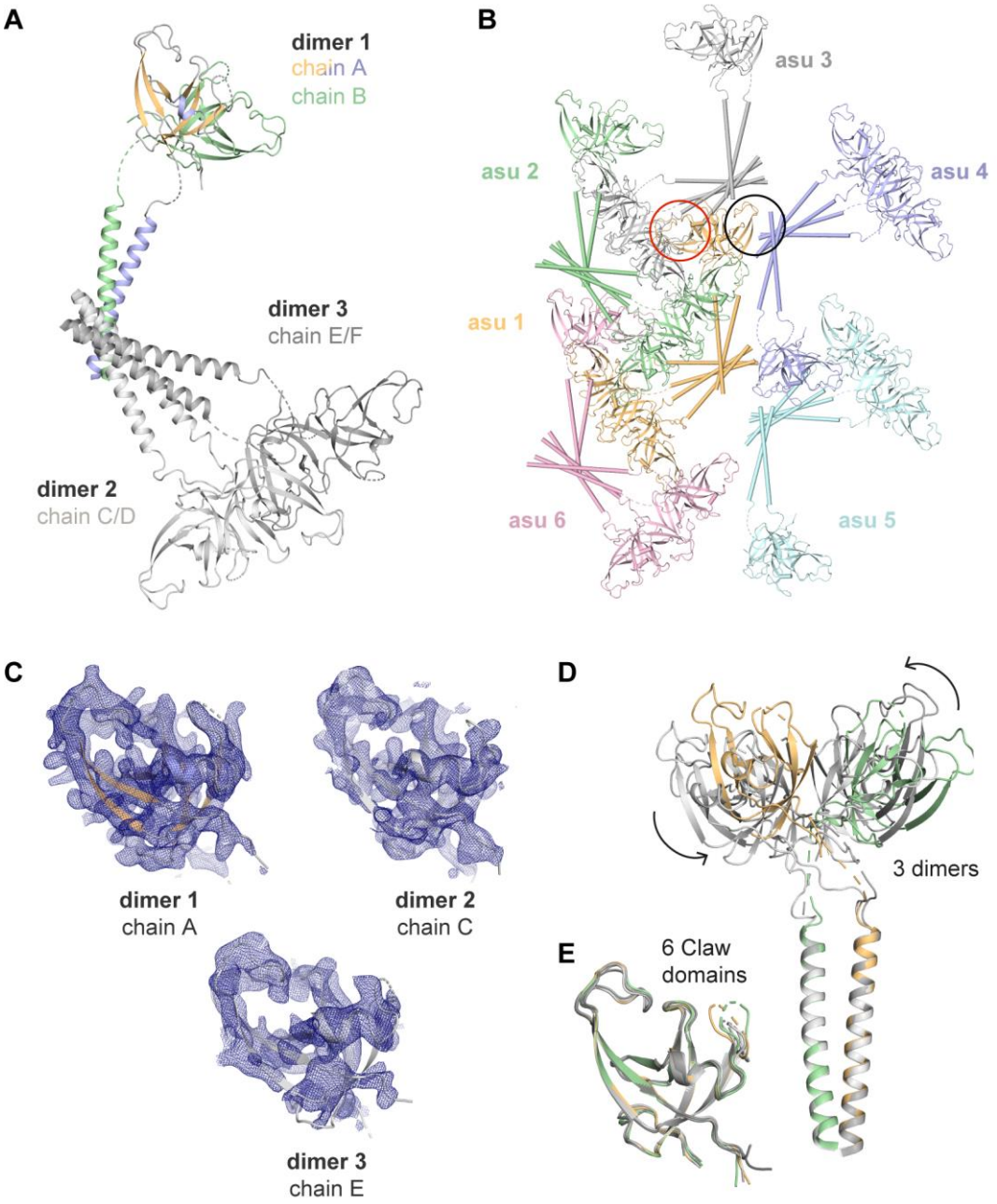

Figure 20. Organization of FIP200 CTR within the crystal. A) The asymmetric unit (asu) contains three dimers of FIP200 CTR, of which two form a crystallographic tetramer. Assembly is mediated via their N-terminal helices. B) Assembly of FIP200 CTR in the crystal lattice. Molecules belonging to the same asu are colored identically. Red circle describes a close crystal contact between dimer 1 (asu 1) and dimer 2 of the neigbouring asu 3. Black circle describes further stabilization of dimer 1 (asu 1) by the N-terminal helices of dimer 2 and 3 in neighboring asu 4. C) Electron density ($2mF_o$-DF_c) of the Claw domains of chain A, chain C and chain E contoured at 1 σ. D) Superposition of the α-helices of the three dimers in one asu. The helices superimpose well, while the Claw domains show flexibility with respect to the helices. E) Superposition of all six Claw domains in one asu shows only minor divergence. Superposition was performed on the C-alpha atoms only for D) and E).

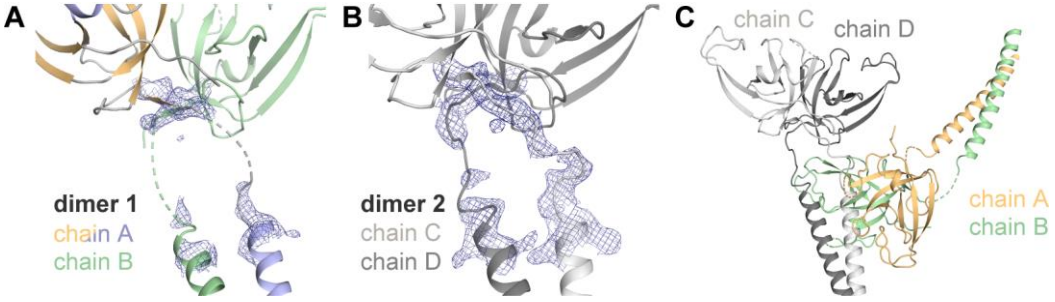

Figure 21. Determination of helix-Claw connectivity by tracking the flexible linker. Linker region of A) dimer 1 (chain A/B) and B) dimer 2 (chain C/D) in cartoon representation with corresponding refined electron density ($2mF_o$-DF_c) contoured at 1 σ. C) Assembly of dimer 1 and dimer 2 in the asymmetric unit cell. The helix of chain C contacts the cleft between the two Claw domains of dimer 1.

4.3.3 FIP200 CTR dimerization is mediated via a conserved and hydrophobic interface

The FIP200 dimers detected in the asymmetric unit were analyzed in more detail to verify a physiologically relevant assembly. Dimerization of FIP200 CTR is mainly mediated via hydrophobic contacts in the Claw domain (interface 1) and the N-terminal helix (interface 2) (Figure 22A, B). The linkers in one dimer cross each other in such a way, that the Claw domain of one monomer sits on the N-terminal helix of the second monomer. Interface 1 is composed of the aromatic residues W1554 and F1521, and bulky hydrophobic residues I1496, I1498, L1508, V1523 and V1556. It is highly conserved among different species (Figure 22B, Appendix: Figure 38), arguing for a physiological relevance. Interface 2 contacts are mediated by L1462, L1466, L1476 and L1480, as well as electrostatic interactions. However, interface 2 conservation is lower compared to interface 1. The surface area covered by dimerization was calculated to be 1444 Å^2 using the PISA server (Krissinel and Henrick, 2007).

FIP200 CTR dimerization was verified by analytical size exclusion chromatography coupled to right angle light scattering (SEC-RALS) (Figure 22C). The molecular weight of the protein was calculated to be 37.5 kDa, in accordance with a dimer. The monomeric FIP200 CTR has a molecular weight of 16 kDa. The physiological importance of dimerization was further undermined by the observation that mutations within the interfaces yielded insoluble protein (data not shown).

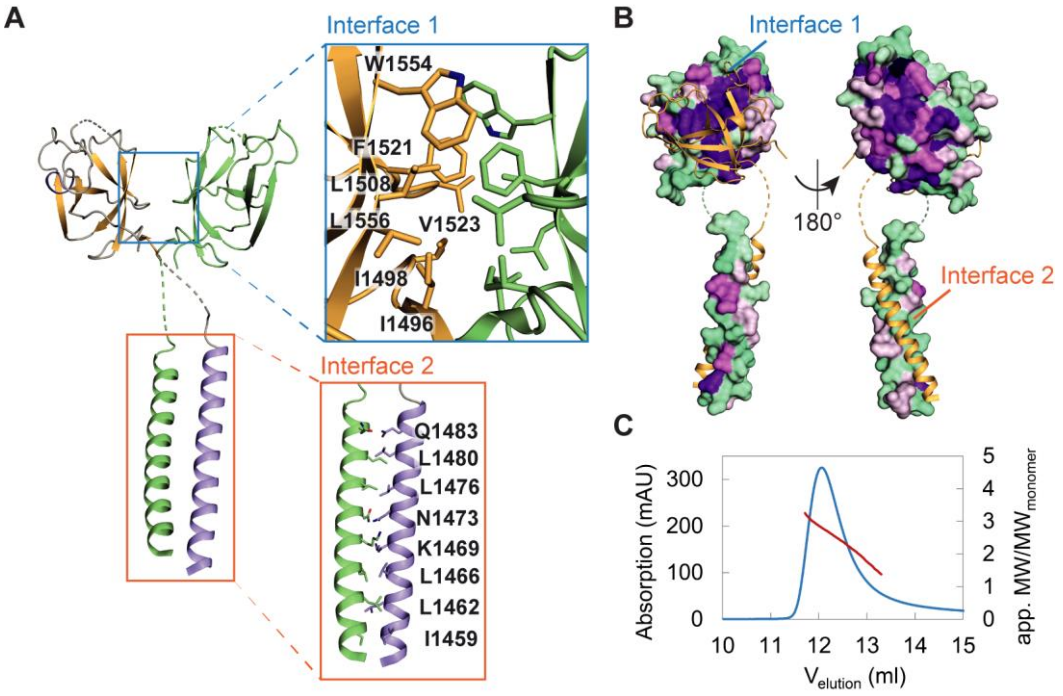

Figure 22. Dimerization of FIP200 CTR. A) The homodimer is formed via two interfaces: Interface 1 (blue box) is located between the two ß-sheets of the Claw domains and mediated mainly by hydrophobic interactions. The N-terminal helices form interface 2 (red box). Monomers are colored in orange/purple and green. Interface residues are shown as sticks and labeled for only one monomer. B) Surface conservation plot of the FIP200 CTR monomer based on the sequence alignment of 11 different species (Appendix, Figure 38). Conserved residues are colored in purple and non-conserved residues in cyan. The second monomer is shown in cartoon representation. C) Analytical size exclusion chromatography on a Superdex S75 10/300 column coupled to right-angle light scattering. Absorption at 280 nm (blue) and oligomeric state (as apparent molecular weight divided by molecular weight of the monomer) (red) are plotted against the elution volume (ml).

4.4 The FIP200 Claw domain adopts an oligonucleotide/ oligosaccharide binding fold

Typical LIR motif binding proteins, such as LC3B and its homologues share a ubiquitin-like fold that consists of a four-stranded ß-sheet flanked by five α-helices (Figure 23A, top and middle panel). Upon binding to the LIR-motif of p62, the peptide is accommodated in a positively charged groove, expanding the ß-sheet (Figure 23A, bottom panel).

The FIP200 Claw domain, however, has a very different architecture compared to LC3B. Its ß-sheet is six-stranded and interrupted by just one short α-helix (Figure 23B, top and middle panel). Analysis of the FIP200 Claw domain structure using

PDBeFold (Krissinel and Henrick, 2004) revealed that the Claw domain belongs to the oligonucleotide/oligosaccharide binding fold (OB-fold) which describes proteins with a five-stranded, mostly closed ß-barrel capped by a short α-helix (Murzin, 1993). Within this family, the FIP200 Claw domain is most similar to cold shock domains (CSDs). In bacteria, CSDs mediate adaptation to cold-shock as well as transcriptional regulation by RNA chaperoning (Bae et al., 2000; Horn et al., 2007). CSD-containing proteins in eukaryotes are often comprised of multiple CSD copies and auxiliary domains resulting in versatile functions in RNA metabolism, differentiation and development (Mihailovich et al., 2010). The Claw domain shares high structural similarity with the *Bacillus subtilis* major cold shock protein B (*bs*CspB) (Schindelin et al., 1993) (Figure 23C). The topologies of FIP200 Claw domain and *bs*CspB are similar with one slight difference: The FIP200 ß-strand corresponding to ß-strand 4 of *bs*CspB is elongated and harbors a ß-kink, leading to its separation into two separate strands. Functionally, *bs*CspB has been described to interact with oligonucleotides, featuring binding constants in the nanomolar range (Max et al., 2006; Sachs et al., 2012; Zeeb et al., 2006).

To test whether FIP200 CTR could also have a nucleotide binding function, isothermal titration calorimetry (ITC) was performed with polythymidines of different lengths (Figure 24). No major heat changes were observed in these experiments upon titration, suggesting that FIP200 CTR cannot bind to oligonucleotides. By comparing the structures of the two proteins, it becomes apparent that the extended loop 5 in the FIP200 Claw domain occupies the position where the oligonucleotide is bound in *bs*CspB (Figure 23B, C, top panels). This supports the ITC results and suggests a different function of the FIP200 CTR compared to cold shock domains.

Interestingly, the electrostatic surface potential of the Claw shows a positively charged pocket that is very different from the positively charged binding groove of the LC3B surface (Figure 23A, B, bottom panels). The question arose whether a LIR motif would be able to bind to this pocket in the Claw domain.

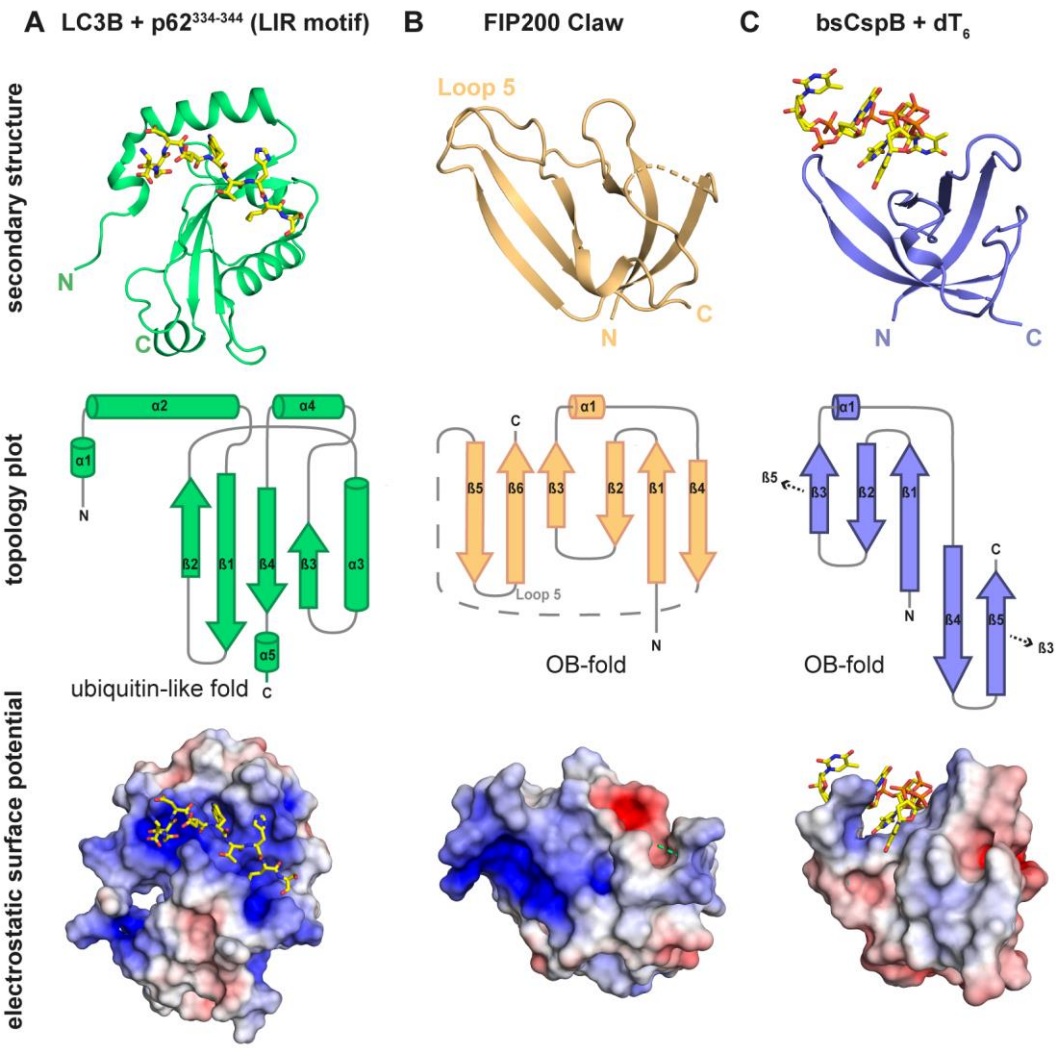

Figure 23. Comparison of FIP200 Claw domain with functionally or structurally similar proteins. Secondary structure in cartoon representation (top), topology plot (middle) and electrostatic surface potential (bottom, - 5 keV (red) to + 5 keV (blue)) for A) LC3B in complex with the p62 LIR-motif (green, PDB code: 2ZJD), B) FIP200 Claw domain (orange) and C) *bs*CspB in complex with dT_6 (purple, PDB code: 2ES2). Ligands are shown as yellow sticks.

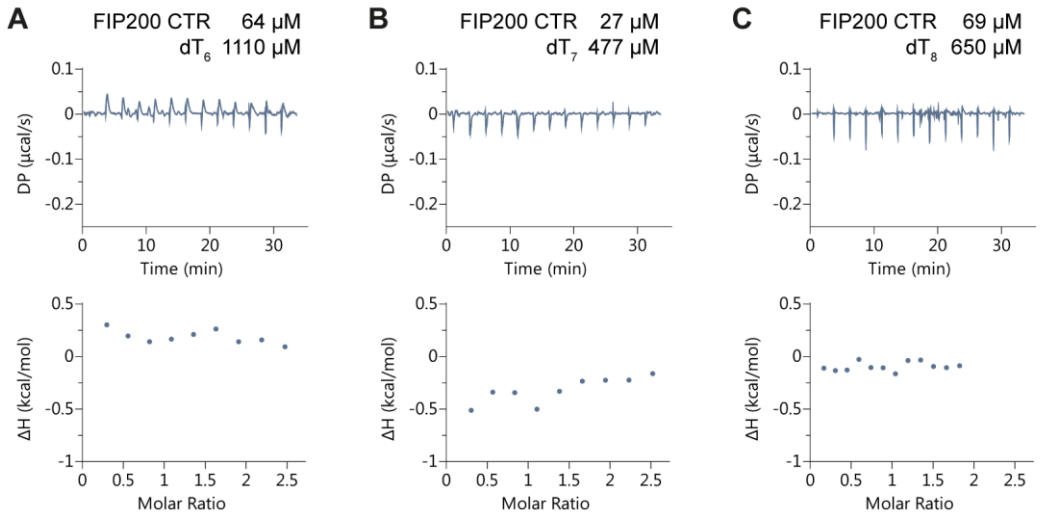

Figure 24. Isothermal titration calorimetry. Polythymidines (A) dT_6, (B) dT_7, (C) dT_8 were titrated into FIP200 CTR using a MicroCal PEAQ-ITC instrument. The temperature was set to 10 °C for dT_7 and dT_8 and to 20 °C for dT_6. No major heat changes were observed.

4.5 Structure-guided identification of a p62 binding site in the FIP200 Claw domain

The FIP200 CTR monomer harbors a prominent highly positively charged pocket in its Claw domain (Figure 25A). Interestingly, the pocket surface, located opposite of interface 1, is conserved among different species (Figure 22B, Appendix Figure 38).

To investigate whether this region could be an interaction site for the p62 LIR motif or phosphorylated residues, the pocket was analyzed in more detail. The positively charged pocket is mainly formed by loop 5 that folds back towards the ß-sheet (Figure 25B). Stacking interactions between aromatic residues F1574 (loop 5), F1582 (strand 6) and F1529 (strand 3) located in the core of the pocket, lock loop 5 in its position. Moreover, N1572 plays a central role in stabilizing loop 5, since its sidechain can form hydrogen bonds with the carboxyl groups of K1569 and V1576, as well as the amide groups of F1574, K1575 and V1576 (Figure 25C). Positively charged amino acids R1573 (loop 5), R1584 (strand 6), K1568 and K1569 (loop 5), as well as H1531 (helix 2) flank the hydrophobic core of the pocket. Interestingly, R1573,

R1584 and H1531 are conserved in metazoans but not among fungi (see sequence alignment, Appendix B, Figure 38) and might therefore possess a functional role.

Several mutations were introduced in the putative binding pocket and neighboring regions of FIP200 CTR to test for interference with p62 interaction. The mutants were designed by me and the experiments were performed by Eleonora Turco and Christine Abert (MFPL, Vienna).

Equilibrium binding analysis was performed as described in section 3.3.14. In brief, GST-p62 FIR 4P was coupled to glutathione sepharose beads and incubated with different GFP-labelled FIP200 CTR mutants, followed by analysis of the fluorescence intensity at equilibrium. As described in section 1.7, GFP-FIP200 CTR wt efficiently bound to GST-p62 FIR 4P covered glutathione sepharose beads. Mutating residues located in a neighboring groove to the pocket (S1532A, L1535A/L1535F) did not have an influence on the interaction (Figure 25D, E). Mutation of the central N1517 to alanine hardly showed any effect, while a mutation to phenylalanine designed to close the pocket, reduced binding. Mutating R1573 or R1584 to aspartate significantly reduced the interaction of FIP200 CTR with p62. A F1574W mutation, also designed to close the pocket, did not have an effect. Disturbing the stacking interactions of the phenylalanines in the pocket core by introducing an alanine at position 1574, however, decreased binding to a large degree. Possibly, the overall structure was disturbed by this mutation.

Figure 25 (right). Structure-guided identification of the p62 binding site on FIP200 CTR. A) Electrostatic surface potential of FIP200 CTR. Positively (+5keV) and negatively (-5keV) charged surfaces are colored in blue and red, respectively. Putative p62 binding pocket of FIP200 CTR is boxed. B) Putative p62 binding pocket shown in cartoon representation. Amino acids of interest are shown as sticks. C) Loop 5 shown in stick representation. Stabilization of the loop is mediated by N1572 forming hydrogen bonds to several backbone atoms (yellow, distances in Å labeled in gray). D) Equilibrium binding analysis: Glutathione sepharose beads were coated with GST-p62 FIR 4P and incubated with the indicated GFP-FIP200 CTR mutants. The fluorescent signal is proportional to the amount of GFP-FIP200 CTR bound to the beads. E) Quantification of results in D). For each sample the GFP intensity was normalized to the signal of GFP-FIP200 CTR wt on GST-p62 FIR 4P coated beads. Average intensity and standard error for three independent experiments are shown. F) Recruitment of GFP-FIP200 CTR to p62-ubiquitin clusters monitored by confocal microscopy. mCherry-p62 was incubated with GST-4x ubiquitin to form condensates in solution. Pre-formed condensates were incubated with GFP-FIP200 CTR. Scale bar = 5 µm. G) Influence of FIP200 variants on p62-ubiquitin condensate formation as described in F). The formation of p62-ubiquitin condensates was monitored over 30 min. For each sample, the number of particles per field is plotted against time. H) Number of particles per field at t=4 in G). For each sample, the particle number was normalized to the average number of p62-ubiquitin clusters formed in absence of FIP200 CTR. Averages and SEM for n≥3 are shown. Experiments in D) - H) were performed by Eleonora Turco (MFPL, Vienna) with mutants designed by me.

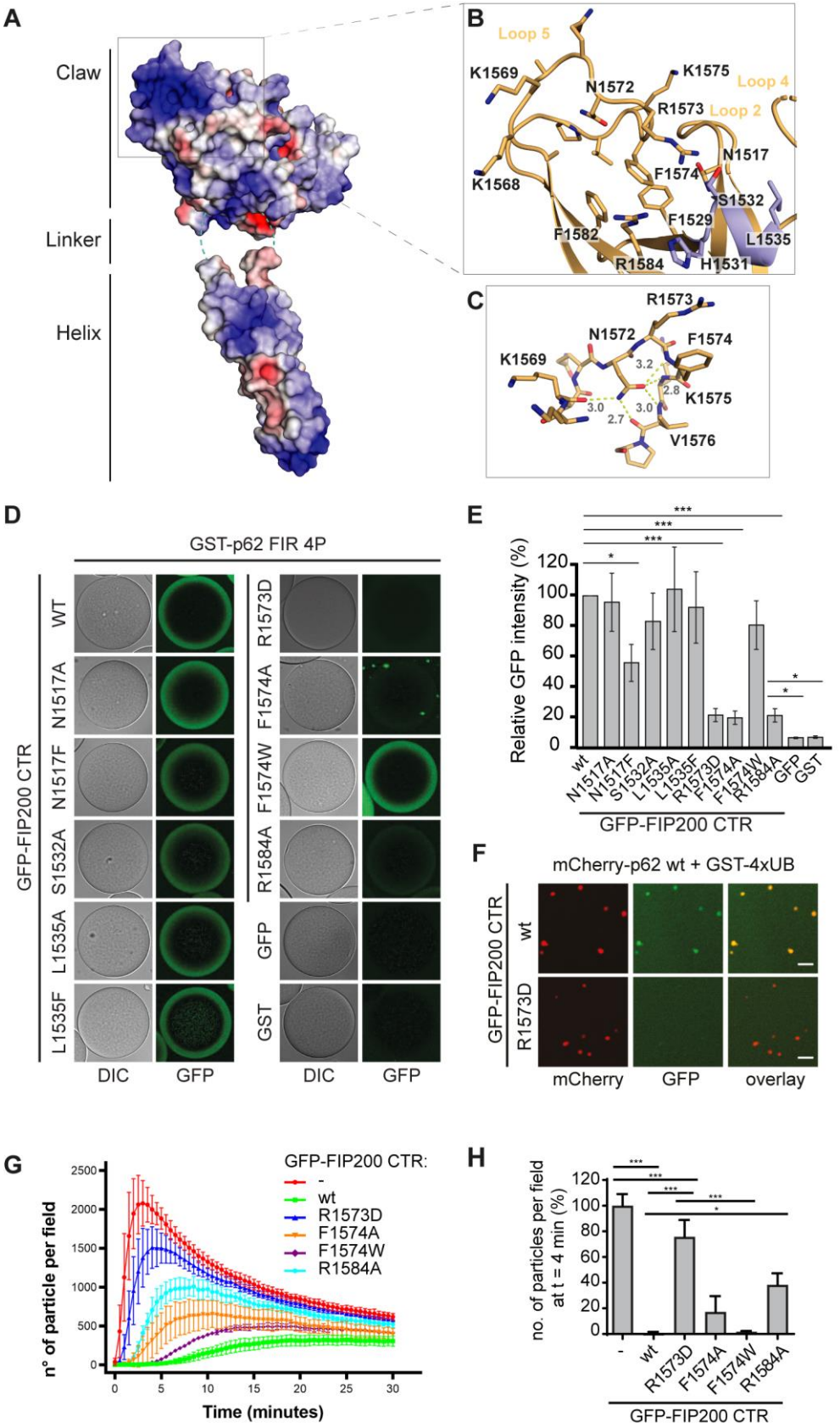
A
Claw
Linker
Helix
B
Loop 5
K1569
N1572
K1575
Loop 4
R1573
Loop 2
N1517
K1568
F1574
S1532
F1529
F1582
L1535
R1584
H1531
C
R1573
N1572
F1574
K1569
3.2
2.8
K1575
3.0
3.0
2.7
V1576
D
GST-p62 FIR 4P
GFP-FIP200 CTR
WT
N1517A
N1517F
S1532A
L1535A
L1535F
R1573D
F1574A
F1574W
R1584A
GFP
GST
DIC
GFP
DIC
GFP
E
Relative GFP intensity (%)
120
100
80
60
40
20
0
wt
N1517A
N1517F
S1532A
L1535A
L1535F
R1573D
F1574A
F1574W
R1584A
GFP
GST
GFP-FIP200 CTR
F
mCherry-p62 wt + GST-4xUB
GFP-FIP200 CTR
wt
R1573D
mCherry
GFP
overlay
G
n° of particle per field
2500
2000
1500
1000
500
0
0
5
10
15
20
25
30
Time (minutes)
GFP-FIP200 CTR:
-
wt
R1573D
F1574A
F1574W
R1584A
H
no. of particles per field at t = 4 min (%)
120
100
80
60
40
20
0
-
wt
R1573D
F1574A
F1574W
R1584A
GFP-FIP200 CTR

Next, the interaction was investigated in the context of self-assembled full-length p62. mCherry-p62 was first incubated with GST-fused ubiquitin chains (GST-4xUb) to allow for p62 condensate formation before GFP-FIP200 CTR wt or R1573D were added (Figure 25F, experimental details in section 3.3.15). In contrast to FIP200 CTR wt, the R1573D mutant was not recruited to pre-formed condensates. Subsequently, it was tested if FIP200 CTR wt or mutants would interfere with the formation of p62-ubiquitin condensates (Figure 25G). To this end, condensate formation was monitored by counting the number of condensates (or particles) at different time points over the course of 30 min. Clearly, addition of FIP200 CTR wt to the mixture delayed condensate formation. Introduction of mutants decreased this effect. In line with previous results, interference with condensate formation was lowest when using the R1573D mutant, as quantified in Figure 25H.

The described structure-function studies led to the identification of two FIP200 CTR point mutations (R1573D and R1584D) that show a strong decrease in p62 FIR interaction *in vitro*. The corresponding positively charged pocket in the FIP200 Claw domain is therefore proposed to be the major p62 binding site.

4.6 Affinity determination of FIP200 CTR and p62 FIR

4.6.1 Isothermal titration calorimetry (ITC)

To gain deeper insight in the formation of the FIP200 CTR – p62 FIR complex, ITC experiments were carried out at varying conditions. Different constructs of the reaction partners at moderate to very high concentrations (low µM to mM) were applied in these measurements. Initially, only a short peptide with the p62 LIR motif was used (DDDWTHL), then a longer peptide comprising the entire p62 FIR. No interaction was observed (data not shown). It was speculated that the GST-mediated dimerization of the GST-fused p62 constructs would be necessary for interaction. However, neither for the GST-p62 FIR wt or 4P mutant an interaction was detectable (Figure 26).

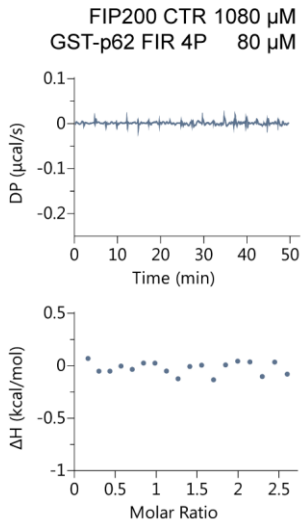

Figure 26. Isothermal titration calorimetry. 1080 µM FIP200 CTR were titrated into 80 µM GST-p62 FIR 4P at 10 °C using a MicroCal PEAQ-ITC instrument. No major heat changes were observed.

Still, the equilibrium binding assay performed by our collaborators (section 4.5, Figure 25) showed a robust interaction between the two proteins, suggesting that this particular experimental setup was critical for monitoring binding. In the equilibrium binding assay, GST-p62 FIR 4P was immobilized on glutathione sepharose beads. This might have led to the formation of an oligomerization-mimicking state of p62 by high local concentration and could be crucial for FIP200 interaction. Requirement for a high-density assembly of p62 could explain why no binding was monitored with solution-based ITC.

4.6.2 Surface plasmon resonance spectroscopy (SPR)

Since SPR allows for ligand immobilization on a surface and is highly sensitive, the technique was chosen next for affinity measurements. Immobilization of GST-p62 variants on a sensor chip surface allowed for monitoring the association and dissociation of FIP200 variants by SPR in real time. GST-p62 FIR wt, LIR mutant and 4P mutant (see section 1.7) were immobilized on different channels of the same sensor chip and a three-fold dilution series of FIP200 CTR passed over them using a single cycle setup according to section 3.3.10 (Figure 27A).

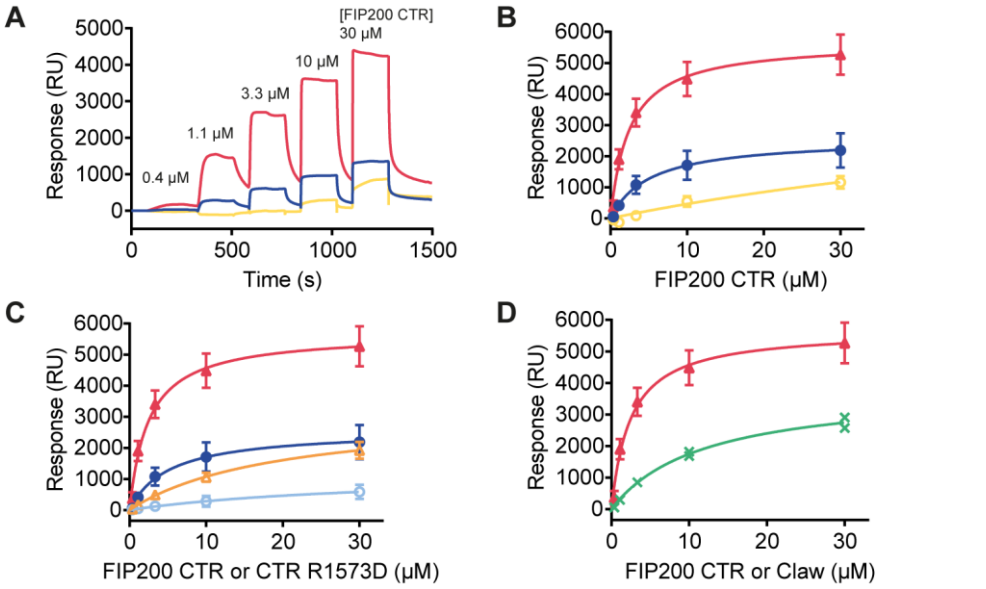

E

Apparent Dissociation Constants

FIP200	GST-p62 FIR	$K_D$app (µM)
CTR	wt	5.1 ± 0.8
CTR	4P	2.4 ± 0.4
CTR	LIRmut	n/d
CTR R1573D	wt	n/d
CTR R1573D	4P	n/d
Claw	4P	11.9 ± 1.5

Figure 27. Interaction of FIP200 CTR and GST-p62 FIR variants monitored by SPR. A) Representative sensorgrams corrected for background by GST binding and buffer control. FIP200 CTR was passed over four flow channels with immobilized GST-p62 FIR wt, GST-p62 FIR LIRmut, and GST-p62 FIR 4P using a single-cycle setup. B) Equilibrium analysis to determine the apparent equilibrium dissociation constant $K_D$app. Response signals at equilibrium were plotted against the concentration of FIP200 CTR and fitted globally with a one site binding model. Independent experiments with two technical replicates each were recorded for a three-fold dilution series of FIP200 CTR (0.4 µM – 30 µM). GST-p62 FIR wt: n=3, GST-p62 FIR 4P: n=5, GST-p62 FIR LIRmut: n=3. C) Equilibrium analysis of FIP200 CTR and FIP200 CTR R1573D binding to GST-p62 wt or GST-p62 4P mutant. D) Equilibrium analysis of FIP200 CTR or FIP200 Claw domain binding to GST-p62 4P. E) Table showing $K_D$app derived from B)-D).

Steep association and dissociation curves made it difficult to determine the association and dissociation rates. Instead, equilibrium analysis (Figure 27B-D) was chosen to obtain apparent dissociation constants ($K_D$app) (Figure 27E). Under the chosen conditions, FIP200 CTR bound to p62 FIR wt with an affinity in the low micromolar range ($K_D$app = 5.1 ± 0.8 µM, Figure 27B, blue curve). As expected, binding to p62 4P mutant was about twice as strong ($K_D$app = 2.4 ± 0.4 µM) (Figure

27B, red curve), while the interaction with the LIR mutant (Figure 27B, yellow curve) was not saturating under these conditions, not allowing $K_D$app determination.

To assess the relevance of the p62 binding pocket for FIP200 CTR interaction, the FIP200 CTR R1573D mutant was also tested in SPR analysis (Figure 27C). Binding to p62 FIR wt (light blue curve) and 4P mutant (orange curve) was strongly reduced compared to FIP200 CTR. Moreover, it was shown that the FIP200 Claw domain alone (Figure 27D, green curve) was capable of binding to p62 FIR 4P mutant ($K_D$app = 11.9 ± 1.5 µM), albeit five times weaker than FIP200 CTR, suggesting a contribution of the helices to the interaction. Hence, binding is most likely mediated by the postulated p62-binding pocket and further enhanced by other interaction sites on the linkers or helices.

Interestingly, high levels of GST-p62 had to be immobilized to receive a positive binding signal. When using 10 times the immobilization level recommended for kinetic analysis, no signal was observed (Figure 28, purple curves). When using 100 times more, a robust signal was detected (Figure 28, green curves), indicating that the FIP200 CTR interaction with p62 is multivalent and governed by avidity.

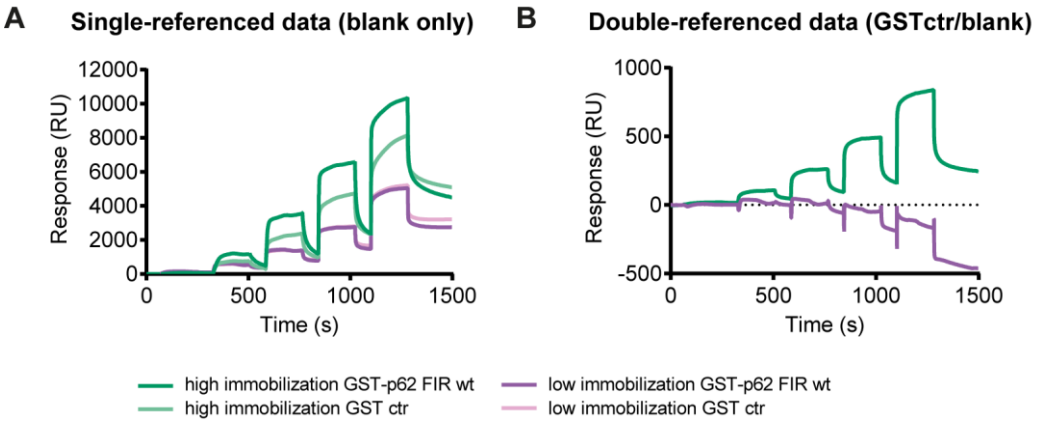

Figure 28. High-density immobilization of p62 required for generation of SPR signal. A) Sensorgrams for the interactions of FIP200 CTR with GST-p62 FIR wt at low immobilization levels (violet) and high immobilization levels (green), corrected for buffer control. B) Sensorgrams shown in A) corrected for GST control.

4.7 FIP200 interacts with p62 via the Claw domain pocket *in vivo*

Structure determination of FIP200 CTR helped to identify the p62 binding pocket in the FIP200 Claw domain. In order to analyze if this pocket would also be of relevance for p62 binding *in vivo*, several experiments were designed and performed by Eleonora Turco (MFPL, Vienna). Results relevant for this thesis are shown in the following section. Further experiments and controls concerning the FIP200 – p62 interaction *in vivo* and its implications in aggrephagy have been published in Turco et al. 2019.

To test if mutations in the Claw domain pocket would interfere with binding to p62 in cells, GFP-tagged FIP200 CTR variants were used to pull down p62 from cell lysate according to section 3.5.1. While an interaction with p62 was detectable for FIP200 CTR wt and the F1574W mutant, no interaction was seen for the R1573D mutant, consistent with the previous *in vitro* results (Figure 29A). The influence of these mutations introduced in endogenous full length FIP200 was subsequently addressed. Co-immunoprecipitation with HA-tagged FIP200 variants as described in section 3.5.2 showed a significant decrease in p62 interaction for the ΔClaw and R1573D constructs compared to wt (Figure 29B). Interestingly, binding was also decreased for the F1574W mutant in this assay.

Additionally, an immunofluorescence assay was performed to directly assess the role of the Claw domain in FIP200 - p62 interaction. The Claw was removed endogenously using CRISPR/Cas9 (FIP200ΔClaw, aa 1493-1594) (see Method sections 3.5.3 and 3.5.4). Colocalization of FIP200 wt or FIP200ΔClaw with p62 was monitored in HeLa cells treated with wortmannin, a PI3K inhibitor that blocks autophagy before isolation membrane elongation (Figure 29C). Colocalization was significantly reduced in cells expressing FIP200ΔClaw compared to cells expressing FIP200 wt, suggesting that the recruitment of FIP200ΔClaw to p62 condensates is impaired.

Taken together, the *in vivo* studies corroborate the findings that the positively charged pocket in the FIP200 Claw domain is a physiologically relevant p62 binding site and that the p62 LIR motif is of major importance for this interaction.

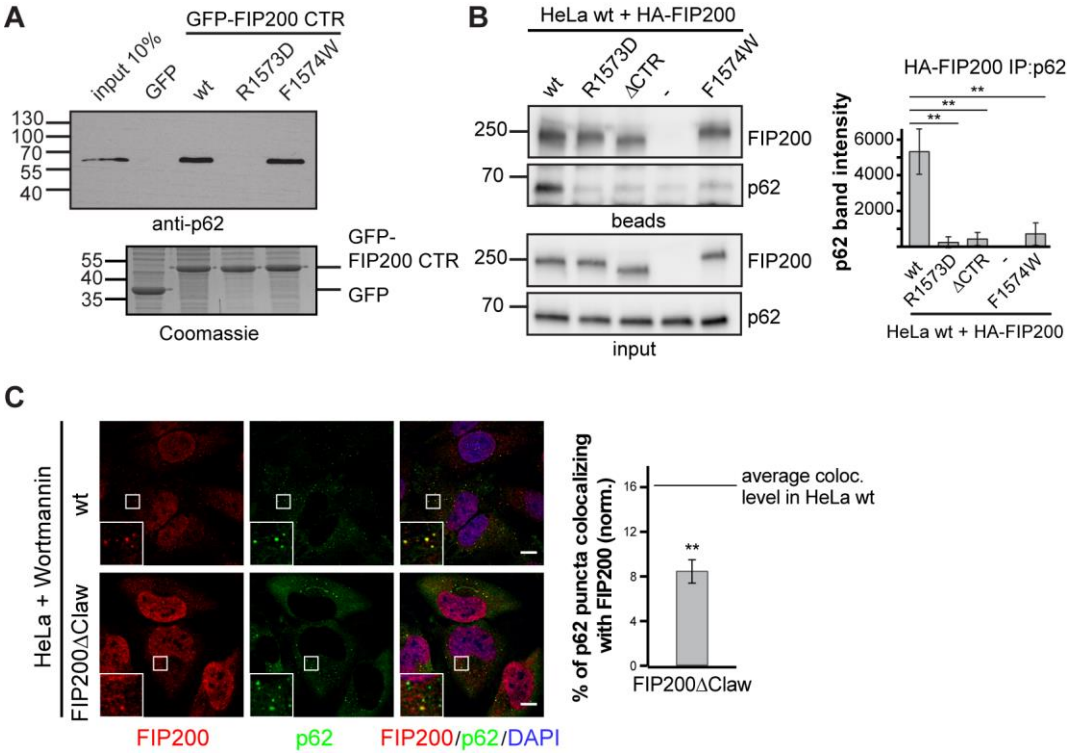

Figure 29. FIP200 – p62 interaction in cells. A) Pull down with GFP or GFP-FIP200 CTR variants as bait. GFP-Trap beads were coated with protein, incubated with cell lysates and analyzed by Western blotting. Loading control of the bait proteins is shown below the blot. B) Anti-HA co-immunoprecipitation in HeLa cells transfected with HA-FIP200. The intensities of the p62 bands were normalized to the amount of the respective bait (HA-FIP200). Average band intensities and SEM (n=3) are shown. C) The Claw domain of endogenous FIP200 was deleted in HeLa cells by CRISPR/Cas9 (FIP200ΔClaw). Cells were treated with wortmannin (1 µM) for 3 h and p62 and FIP200 were detected by immunofluorescence. Scale bar = 10 µm. The percentages of p62 puncta colocalizing with FIP200 in FIP200ΔClaw cells is compared to the average level of colocalization in wt cells. Average colocalization and SEM for n=3 is shown. All experiments were designed and performed in the group of Sascha Martens (MFPL, Vienna), based on the identification of the structure-based mutants by me.

4.8 FIP200 CTR binds to liposomes through its p62 binding pocket

Since FIP200 is part of a cellular process involving membrane recruitment, elongation and shaping, I speculated that it might interact with membranes itself. The overall positive charge of FIP200 CTR (pI = 10.0) would be beneficial for membrane binding. Also, the overall structure of FIP200 CTR resembles other membrane binding regions, like the C-terminus of early endosome antigen 1 (EEA1) involved in endosomal trafficking (Simonsen et al., 1998). Like FIP200 CTR, the EEA1 C-terminus is composed of an N-terminal coiled-coil and a C-terminal globular FYVE domain, that

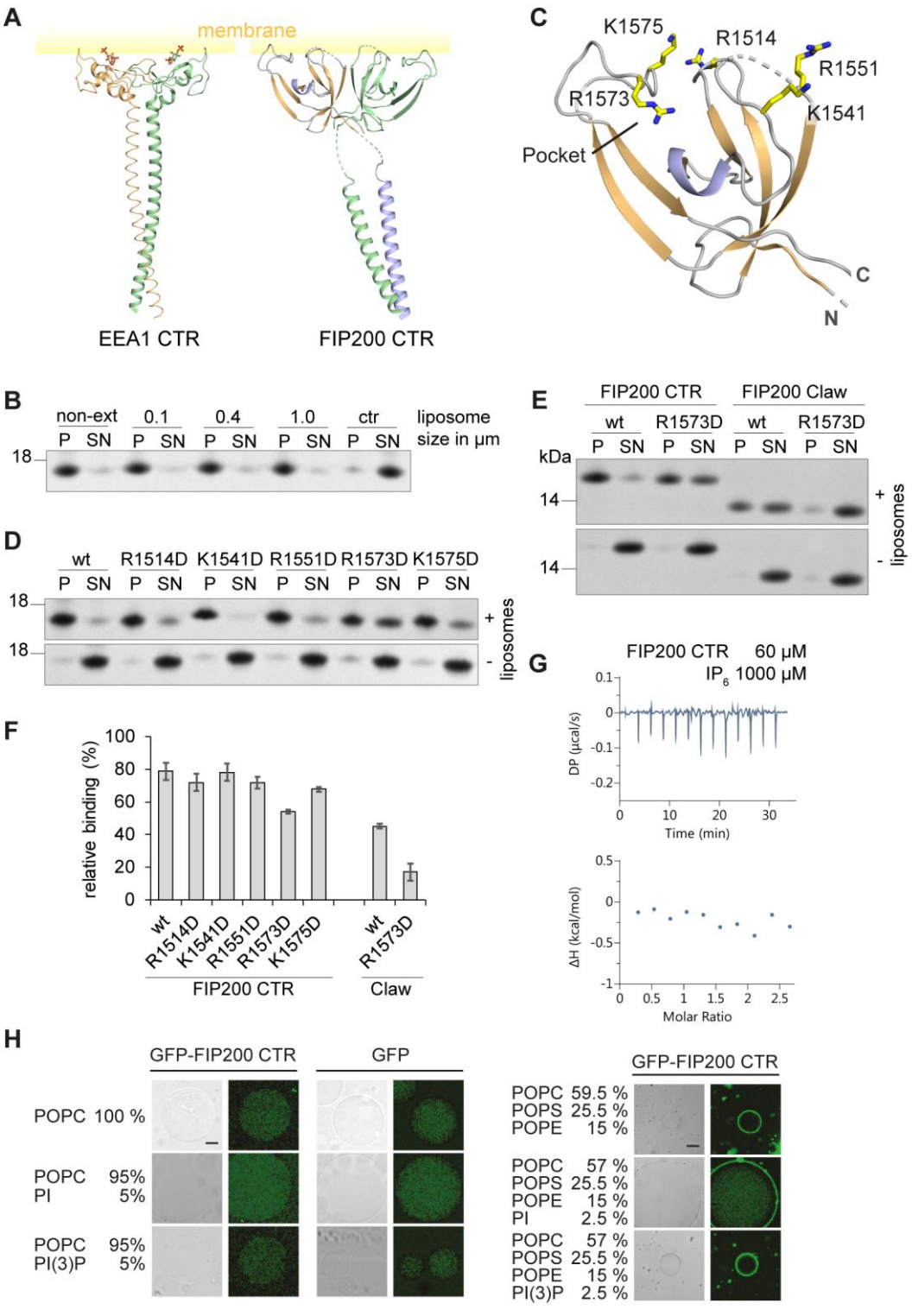
A
membrane
EEA1 CTR
FIP200 CTR
C
K1575
R1514
R1551
R1573
K1541
Pocket
C
N
B
non-ext
0.1
0.4
1.0
ctr
liposome size in µm
P SN P SN P SN P SN P SN
18
D
wt
R1514D
K1541D
R1551D
R1573D
K1575D
P SN P SN P SN P SN P SN P SN
18
18
+ liposomes
- liposomes
E
FIP200 CTR
FIP200 Claw
wt
R1573D
wt
R1573D
P SN P SN P SN P SN
kDa
14
14
+ liposomes
- liposomes
F
relative binding (%)
100
80
60
40
20
0
wt
R1514D
K1541D
R1551D
R1573D
K1575D
wt
R1573D
FIP200 CTR
Claw
G
FIP200 CTR 60 µM
IP6 1000 µM
DP (µcal/s)
0.1
0
-0.1
-0.2
0
10
20
30
Time (min)
ΔH (kcal/mol)
0.5
0
-0.5
-1
0
0.5
1
1.5
2
2.5
Molar Ratio
H
GFP-FIP200 CTR
GFP
POPC 100 %
POPC 95%
PI 5%
POPC 95%
PI(3)P 5%
GFP-FIP200 CTR
POPC 59.5 %
POPS 25.5 %
POPE 15 %
POPC 57 %
POPS 25.5 %
POPE 15 %
PI 2.5 %
POPC 57 %
POPS 25.5 %
POPE 15 %
PI(3)P 2.5 %

binds to PI(3)P (Dumas et al., 2001), the signature lipid of autophagosomes (Figure 30A).

To test if FIP200 CTR binds to membranes, liposomes were prepared as described in section 3.3.11 and co-sedimentation assays performed according to section 3.3.12. FIP200 CTR clearly bound to Folch liposomes without preference for a certain diameter (Figure 30B). In fact, the highest binding level was monitored for a mix of differently sized liposomes. Assuming that FIP200 interacts with membranes in a way similar to EEA1, the Claw loop region would be a promising membrane binding area. Arginines and lysines R1514, K1541, R1551 and K1575 located in this area were mutated to aspartates within the FIP200 CTR construct (Figure 30C). R1514D, K1541D and R1551D did not exhibit a markedly reduction in liposome binding, while the interaction was slightly reduced for K1575D (Figure 30D, F). Because the positively charged pocket might also contribute to membrane interaction, the R1573D mutant deficient in p62 FIR binding was also subjected to liposome co-sedimentation assays. Strikingly, a decrease in binding was monitored for this mutant. Furthermore, liposome interaction was strongly reduced when the FIP200 Claw domain instead of the CTR was applied to co-sedimentation assays (Figure 30E, F). Especially for the Claw R1573D mutant, only very weak membrane binding was detected, suggesting that the p62 binding pocket overlaps with the membrane interaction site.

Figure 30 (left). FIP200 interaction with liposomes. A) Structural comparison of the C-terminal regions of EEA1 containing a coiled-coil and a FYVE domain and FIP200 CTR containing a helical region and the Claw domain. Inositol headgroups crystallized with EEA1 CTR are shown as sticks. Putative membrane location is depicted as a yellow box. B) Liposome size dependency of FIP200 CTR - liposome interaction monitored by co-sedimentation assay. Liposomes with different diameters were generated by extrusion (Non-ext – non-extruded, ctr – protein only control). SDS-PAGE results show the soluble fraction in the supernatant (SN), and the bound fraction in the pellet (P). SDS-PAGEs are representative for three independent experiments. C) Structure of the monomeric Claw domain in cartoon representation with amino acids putatively involved in liposome binding depicted as sticks. D) – E) Folch liposome co-sedimentation assays as in B). D) Interaction of FIP200 CTR wt or mutants with liposomes. E) Interaction of FIP200 CTR or FIP200 Claw (with or without R1573D mutation) with liposomes. F) Quantification of results from D) and E). Shown is the percentage of protein found in the pellet with respect to the total amount of protein applied on the gel. FIP200 CTR wt: n=9, for FIP200 CTR R1514D/ K1541D/ R1551D/ R1573D n=6, for FIP200 CTR K1575D, FIP200 Claw wt or R1573D: n=3. Error bars represent the standard deviation. G) Isothermal titration calorimetry. 1000 µM IP_6 were titrated into 60 µM FIP200 CTR at 10 °C. No major heat changes were observed. H) Binding of GFP-FIP200 CTR to GUVs of different lipid composition. This experiment has been performed by Christine Abert (MFPL, Vienna).

To test for a direct interaction of FIP200 CTR with inositol phosphates, an ITC experiment was performed with inositol hexaphosphate (IP_6), a fully phosphorylated, soluble headgroup of phosphatidylinositol (see Methods section 3.3.9). No major heat changes were detected during the experiment, indicating that IP_6 does not bind to FIP200 CTR (Figure 30G). Also, binding of GFP-tagged FIP200 CTR to giant unilammelar vesicles (GUV) of different lipid compositions was not dependent on PI or PI(3)P, but rather on negatively charged lipids like phosphatidylserine (PS) (Figure 30H, experiment performed by Christine Abert, MFPL).

To sum up, this data indicate that FIP200 CTR does interact with membranes via its positively charged pocket in the Claw domain and the helices. The binding mechanism seems to be different from that of EEA1, due to distinct membrane-protein interfaces and lipid specificity.

4.9 Towards the structure of a FIP200 - p62 complex

4.9.1 Crystallization attempts of FIP200 CTR - p62 complex

Solving the crystal structure of FIP200 CTR was important for mapping the p62-binding region on FIP200. Still, dissecting the exact binding mode of the two proteins, and to what extent the interaction is mediated by the p62 LIR-motif and/or p62 phosphorylation, needs to be addressed to fully understand this interaction. To this end, I attempted to crystallize a FIP200-p62 complex.

Neither co-crystallization or soaking of FIP200 CTR with a peptide comprising only the p62 LIR-motif (DDDWTHL) was successful. Also, co-crystallization with FIP200 CTR and the GST-p62 FIR 1P mutant did not yield any crystals. With growing evidence that the interaction might be of low affinity and governed by avidity effects, fusion constructs were designed to increase the local concentration of the binding partners and chances of interaction. These constructs comprised either the FIP200 CTR (aa 1458-1594) or Claw domain (aa 1494-1595) fused N- or C-terminally to p62. For p62, either the entire FIP200 interaction region (aa 326-380), a shortened region containing just one phosphorylation site or all four phosphorylation sites (aa 332-372 and 332-357, respectively) were designed. Linkers of different lengths, composed of

glycine and serine, have been chosen to maximize crystallization chances. An overview of the fusion constructs can be found in Figure 31. All constructs have been cloned and expressed according to the procedures described in Methods section 3.2 and 3.3.3. Purification according to section 3.3.4 and initial crystallization trials using commercial screens (3.1.10) have been performed on selected constructs and are still in progress. So far, no crystals have been obtained.

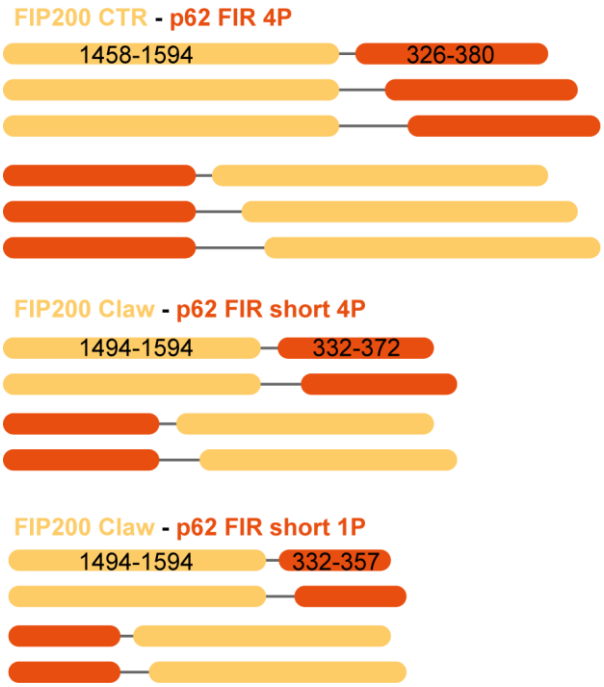

Figure 31. Scheme of FIP200 – p62 fusion constructs designed for crystallization trials.

4.9.2 Identification of key interaction residues by a peptide SPOT array

To design optimal crystallization constructs, it is critical to further narrow down the FIP200 binding region on p62 and identify key interacting amino acids. Therefore, a peptide SPOT array with 25-mer p62 peptides was designed and probed with FIP200 CTR as described in section 3.3.13 (Figure 32A, B).

An overlap scan using peptides with an offset of 3 amino acids between consecutive peptides (covering p62 amino acids 294–399, LIR motif: 335-341) (spots 1A-2I, green box,) showed that the intact LIR motif is required for the interaction with FIP200. When the LIR motif was disrupted, almost no binding signal

could be observed (1H,1I). The strongest signal was observed for peptides also containing the S349 phosphorylation site (1M-N). Interestingly, the interaction was lost when amino acids N330+C331+N332 were omitted from the peptide, suggesting a functional relevance.

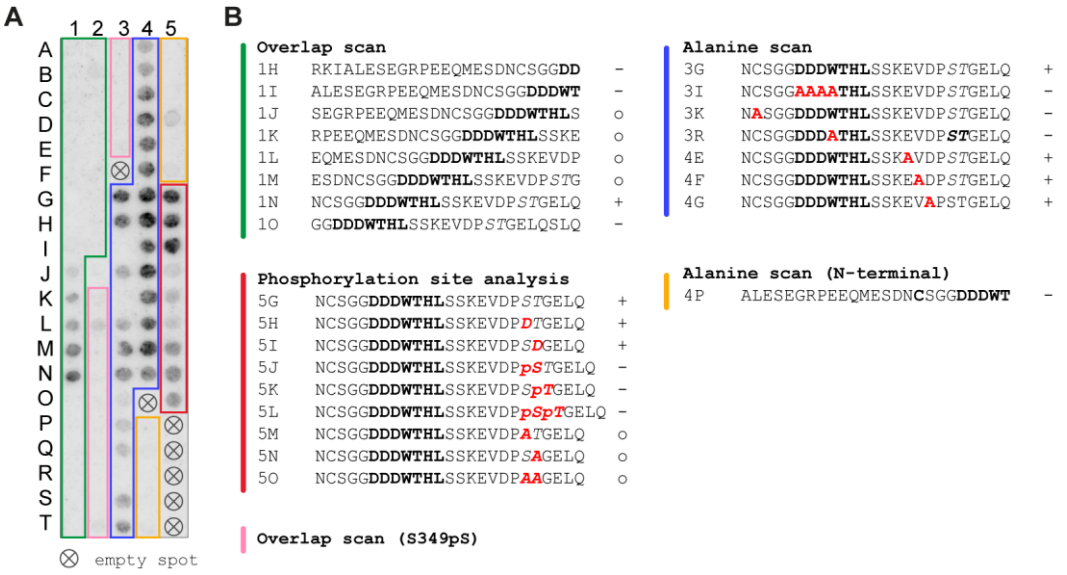

Figure 32. Peptide array. A) 25-mers of p62 peptides have been spotted on a membrane and incubated with 80 µM of His-FIP200 CTR. Binding signal was detected by chemiluminescence of an anti-polyHistidine-peroxidase antibody. Boxes represent different peptide array analyses – overlap screen (green), alanine scan (blue), N-terminal alanine scar (yellow), phosphorylation site analysis (red), overlap screen including S349pS (pink). B) Selected 25-mer peptides in one-letter code. The LIR motif (aa 335-341) is depicted in bold and the phosphorylation site S349/T350 in italics. Mutations are bold and colored in red. The level of chemiluminescence signal was judged by eye: + strong signal, o medium signal, - weak or no signal.

Alanine scanning (spots 3G-4N, blue box) revealed that peptides with mutations N-terminal to the p62 LIR motif (3J-N) or within the LIR motif (3I, 3O-4A) showed a decreased binding signal compared to p62 wt (3G) while peptides with C-terminal mutations (4D-H) showed a strong binding signal. In particular, the amino acids C331 and W338 are of major importance for binding, as their mutation results in a complete loss of signal (3K, 3R, respectively). This also explains the loss of signal for peptide 1O in the overlap scan. Mutation of the phosphorylation sites S349A or T350A only slightly reduced the interaction with FIP200 CTR. Introducing a phospho-mimicking mutation S349D did not result in stronger binding compared to wt, but rather similar levels (3H).

An alanine scan based on a peptide N-terminal to the LIR motif (4P-5F, 4P – wt, yellow box) showed that the complete LIR motif is required for p62-peptide - FIP200 CTR interaction, as none of the spots showed a binding signal.

Next, the importance of the phosphorylation sites S349/T350 was analyzed in more detail (spots 5G-O, red box). Unexpectedly, the peptides containing phosphorylated amino acids (5J-L) bound to FIP200 CTR much weaker compared to peptides with phospho-mimicking mutations to aspartate (3H,5H-I) or even alanine mutations (5M-O). In line with this, mapping the binding region with peptides including phosphorylated S349 did not yield any result as almost no signal was observed (spots 2K-3E, pink box).

The peptide array confirmed the importance of the LIR motif for the interaction of FIP200 and p62. Contradictory to the previous results, phosphorylation does not seem to be crucial. This discrepancy is further discussed in section 5.3.

5. Discussion

In this study, a missing link between autophagosomal cargo recognition and isolation membrane formation has been established by elucidating the molecular basis of FIP200 recruitment to p62 condensates. Solving the FIP200 CTR crystal structure allowed for a structure-function study that ultimately led to identification of the p62 binding site on FIP200 CTR. Importantly, key residues required for p62 condensate processing were identified. Binding studies contributed to a more thorough understanding of the interaction. Furthermore, membrane interaction was monitored for FIP200 CTR, suggesting an additional function in autophagy. In the following, the structural model as well as putative interaction modes of FIP200 with p62 will be discussed. In particular, considerations on the role of receptor oligomerization and FIP200 full length function, as well as possible membrane interaction ultimately led me to propose a mechanism for selective autophagy progression mediated by p62 and FIP200.

5.1 Physiological relevance of the FIP200 CTR crystal structure

Protein crystal structures are models and have their limitations (DePristo et al., 2004). The arrangement of molecules in the crystal lattice might bear important information on oligomer assembly, but it can also lead to wrong assumptions due to non-physiological interactions. In the case of FIP200 CTR, for example, the N-terminal helix of one dimer in the asymmetric unit intercalates into the Claw dimer interface of another dimer (Figure 21C). This raises the question if the proposed model is physiologically relevant. Here, it was shown that FIP200 CTR assembles as a dimer in solution using SEC-RALS. Mutations in the dimerization interface rendered the protein insoluble (data not shown). Structure-function studies in cells also verified the proposed p62 binding pocket, indicating the overall correctness of the structural model. Interestingly, another crystal structure comprising the FIP200 Claw only, without the helix, was recently solved to 1.6 Å resolution in the laboratory of James Hurley (UC Berkeley) and has been published together with the FIP200 CTR structure (Turco et al., 2019). With an RMSD of 0.62 Å, this Claw domain structure is almost

identical to the Claw domain of the CTR structure (Figure 33A). Although the dimerization interface is very similar, FIP200 CTR chain B is displaced by roughly 8 Å due to an intercalating helix from a symmetry related molecule, resulting in an RMSD of 2.16 Å for the entire dimer. The sidechain orientations in the p62 binding pocket are remarkably similar, except for R1573. Interestingly, this key amino acid, identified as crucial for p62 interaction, moves about 4 Å and engages in sulfate interactions (Figure 33B).

Biochemical and cell biology data as well as the comparison with the Claw domain structure that was crystallized under different conditions, verify that the FIP200 CTR structure model resembles a physiological state of the protein.

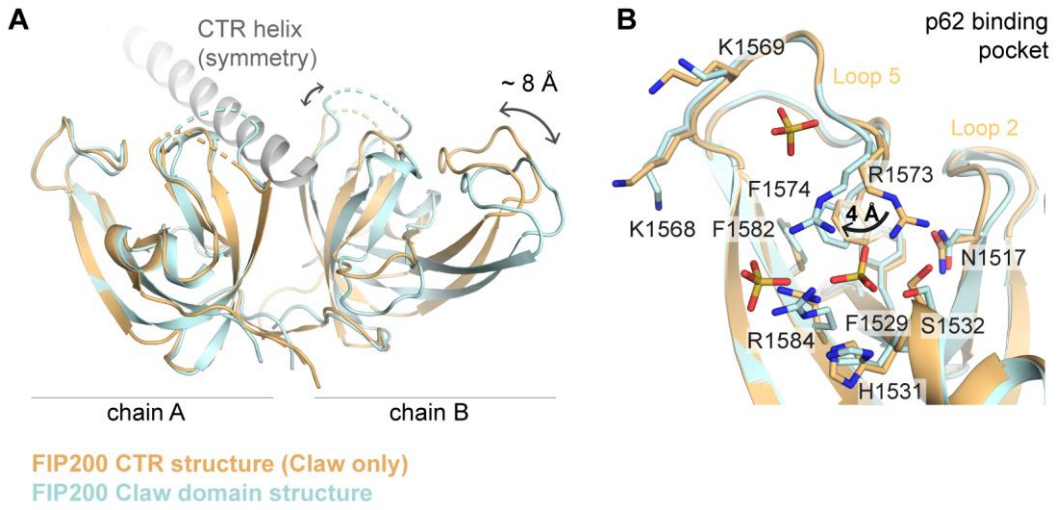

Figure 33. Comparison of FIP200 CTR structure (orange) with FIP200 Claw structure (light blue). A) Superposition of the Claw domains. Only chain A was used for alignment. FIP200 CTR chain B is displaced by approximately 8 Å compared to the FIP200 Claw structure due to the intercalating helix from a CTR symmetry related molecule. B) p62 binding pockets of FIP200 CTR and Claw structure. Binding of sulfate ions to the pocket in the Claw structure is mainly mediated by R1573 and leads to its displacement by 4 Å compared to the CTR structure.

5.2 Functional versatility of the OB-fold

The FIP200 Claw domain adopts an OB-fold and is, among this family, structurally very close to bacterial CSDs that mediate adaptation to cold-shock by transcriptional regulation through RNA interaction (Bae et al. 2000; Horn et al. 2007). Despite the high structural similarity with CSDs, the FIP200 Claw does not bind to oligonucleotides (Figure 24). Occlusion of the canonical nucleotide binding site by Claw loop 5 impedes an interaction similar to that of bacterial CSDs.

However, OB-domains are not restricted to oligonucleotide binding (reviewed in Arcus 2002). According to the structural classification of proteins - extended (eSCOP) database (Fox et al., 2014), the OB-fold includes 17 superfamilies of which only one is referred to as nucleic acid binding. Although this superfamily is by far the largest one within the OB-folds, functions of other superfamilies range from catalytic activity as pyrophosphatases (Samygina et al., 2001) over oligosaccharide binding of bacterial toxins (Ling et al., 1998) to protein-protein interactions. In the trimeric cell-puncturing device of bacteriophage T4, for example, the OB-fold mediates intersubunit contacts (Kanamaru et al., 2002). Moreover, bacterial superantigens bind to the major histocompatibility complex II via an OB-fold domain and stimulate immune response by simultaneous T-cell receptor interaction (Jardetzky et al., 1994; Roussel et al., 1997). These are just a few examples that shall illustrate the functional versatility of OB-fold containing domains.

As shown in this thesis, the FIP200 Claw domain directly binds to liposomes (Figure 30). To my knowledge, no lipid interaction has been monitored for OB-folds so far. If lipid binding turns out to be physiologically relevant, this might open up a new and broad field of OB-fold domain functions.

In addition, the FIP200 Claw is the first domain described that binds to LIR motifs without adopting a ubiquitin-like fold. This implicates that the LIR-motif interactome might be larger than estimated up to date.

5.3 FIP200 Claw pocket as a binding interface for phosphorylated receptors

The fundamental relevance of the p62 LIR motif for the interaction with FIP200 CTR has been shown *in vitro* and *in vivo* in Turco et al. 2019. Without a structure of the FIP200 – p62 complex, however, only assumptions can be made on the atomic details of this interaction. The FIP200 Claw pocket provides the requirements for a LIR motif binding site: It combines a hydrophobic core with flanking positively charged amino acids (see section 1.4.2). Still, the proposed binding site rather resembles a pocket and not a stretched binding groove, as it is seen in typical LIR-binding proteins (Figure 34). This suggests a slightly different mode of interaction for p62 LIR or a binding site distinct from the pocket. As determined by SPR, the Claw domain is sufficient for the p62 FIR interaction (Figure 27D), indicating that the LIR binding site is located within the Claw. However, affinity is reduced, pointing towards a role of the FIP200 CTR linkers and helices in mediating the interaction.

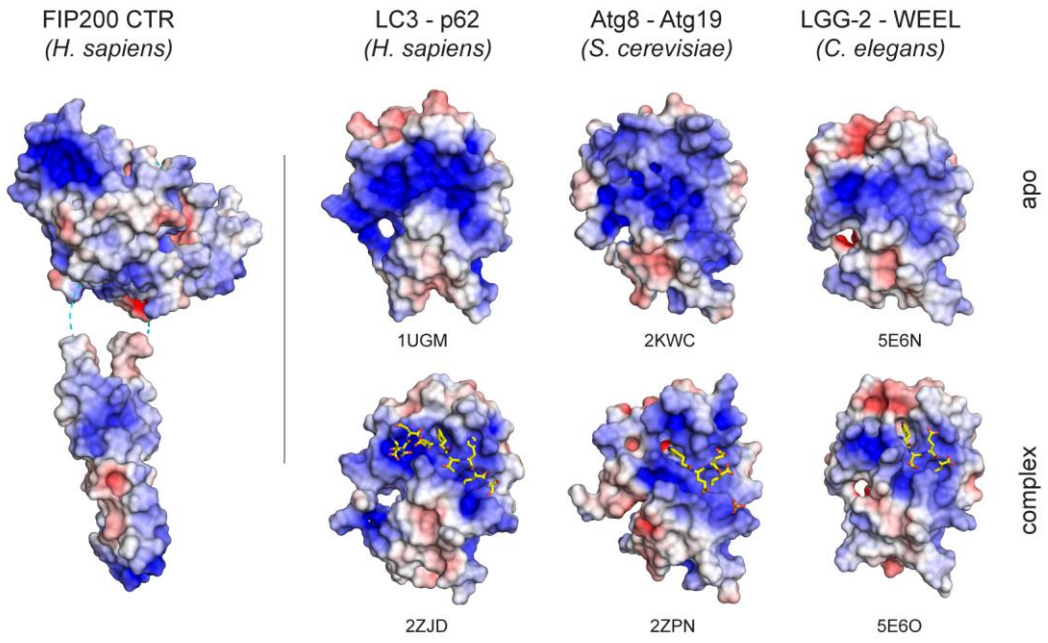

Figure 34. Binding site comparison of FIP200 CTR with Atg8 family proteins. Proteins in surface representation colored according to the electrostatic surface potential; +5 keV (blue) to -5 keV (red). For Atg8 family proteins, apo structure and complex structures with LIR motif as yellow sticks are shown. PDB codes are stated below the respective structure.

If the LIR motif did not bind to the FIP200 CTR pocket, what part of p62 FIR would? Here, it was shown that p62 FIR phosphorylation enhanced binding to FIP200 CTR (see section 1.7 and 4.6.2). The positively charged FIP200 CTR pocket contains two arginines (R1573, R1584) that directly point into and two lysines (K1568, K1569) that flank the pocket. Arginines have been shown to form very stable, covalent-like interactions with phosphates (Woods and Ferré, 2005), making the pocket a possible binding site for phosphorylated residues. Interestingly, the high-resolution Claw domain crystal structure shows three sulfate ions bound to the pocket (Figure 33B). Since the FIP200 CTR interaction with phosphomimetic variants of p62 FIR was enhanced (Figure 27), I speculate that the positively charged pocket might actually bind phosphorylated serines instead of the LIR motif.

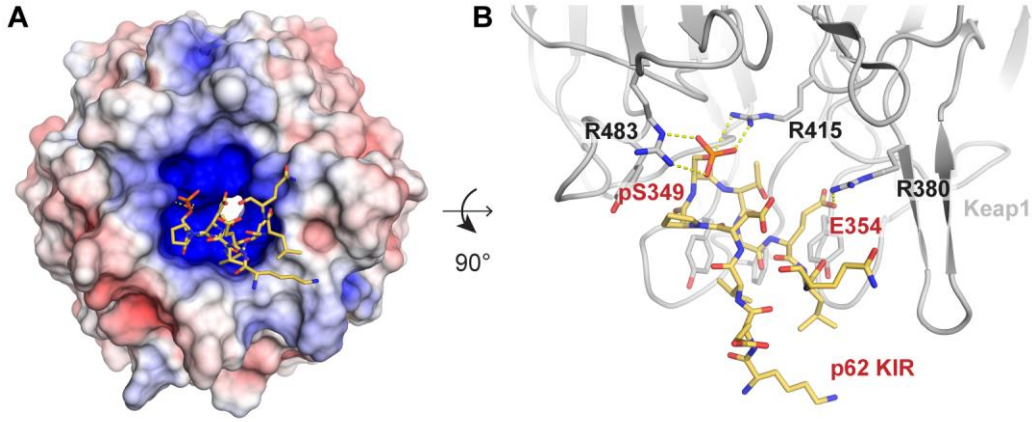

Figure 35. Interaction of phosphorylated p62 KIR motif with Keap1. A) Complex of Keap1 and p62 KIR, shown as surface representation colored by electrostatic surface potential and as yellow sticks, respectively. B) Close-up of the interaction. Keap1 shown in cartoon representation with selected residues as gray sticks (black labels). p62 KIR peptide in yellow stick representation (red labels). Hydrogen bonds in yellow. PDB code: 3WDZ.

One of the proposed p62 phosphorylation sites has been shown to be relevant in activation of oxidative stress response through the Nrf pathway by p62 - Keap1 interaction (Ichimura et al. 2013, see section 1.4.3). Binding of the p62 KIR motif to a positively charged cavity in Keap1 is enhanced by phosphorylation of p62 serine S349 (Figure 35A). The same residue also enhances p62 - FIP200 interaction upon phosphorylation (section 1.7). The phospho-serine binds to two arginines (R483, R415) (Figure 35B), while glutamate E354 interacts with another arginine (R380) in

the Keap1 binding site. Furthermore, several aromatic amino acids engage in peptide accommodation. Analysis of the p62 interaction with Keap1 leads towards the hypothesis that S349, located in the p62 KIR motif, binds to the FIP200 CTR pocket in a phosphorylation-dependent manner.

The peptide array conducted in this study did not confirm the FIP200 – p62 interaction upon phosphorylation of S349 (Figure 32). This could be due to the proximity of peptides on the array, where peptides with phospho-serines might have repelled each other in a way that FIP200 CTR interaction was hindered. Nevertheless, there is a body of evidence for enhancement of receptor-scaffold protein interaction upon receptor phosphorylation in the literature. In fact, the importance of receptor phosphorylation has been well described in yeast. Phosphorylation of the Cvt pathway receptor Atg19 stimulates Atg11 interaction (Pfaffenwimmer et al., 2014). Pexophagy receptors *pp*Atg30, *sc*Atg36 and mitophagy receptor *sc*Atg32 also bind to Atg11 in a phosphorylation-dependent manner (Aoki et al., 2011; Farré et al., 2008, 2013). Similar to the situation in p62, the phosphorylation sites are located downstream of the AIM motifs and contribute to the interaction with Atg8 (Farré et al., 2013). The identified consensus sequence for the yeast receptor phosphorylation site (D/S)ILSSS (Farré et al., 2013) is not conserved in humans. However, also mammalian OPTN was reported to become active upon phosphorylation of a residue adjacent to the LIR motif (Wild et al., 2011). Considerable similarities between the phosphorylation-based regulation of the p62 - FIP200 interaction reported in this study and the receptor activation in yeast suggest that metazoan and yeast cargo sequestration employ the same regulatory principles.

Taken together, how p62 exactly binds to FIP200 CTR is not entirely understood. Claw pocket interactions with either p62 LIR or KIR motif are both possible. Maybe, both regions act in concert to engage with FIP200 CTR. Most likely, additional interfaces are located in the FIP200 CTR helices. Further experiments will be required to elucidate the exact binding mechanism of p62 to FIP200. Importantly, both LIR- and KIR-binding scenarios are compatible with the finding that LC3B can displace FIP200 CTR from p62 (Turco et al., 2019) because LIR and KIR are in very close proximity, making the interaction mutually exclusive with LC3B.

Interestingly, the FIP200 CTR linker region contains one proposed phosphorylation site at S1484 that might be highly relevant for processes involving Claw domain function. The question if FIP200 CTR itself is phosphorylated at S1484 and how this would affect autophagy and p62 interaction remains to be solved.

5.4 Interaction of FIP200 with other cargo receptors

FIP200 has been shown to bind to p62 via its CTR that is homologous to the C-terminus of Atg11. This interaction of cargo receptor and scaffold protein has been described for a number of different cargo receptors in yeast, while almost no information on the mammalian receptor – scaffold protein interaction is available. Except for this study, binding of FIP200 to a cargo receptor has recently been described for ER-phagy (Smith et al., 2018). The ER membrane protein cell-cycle progression gene 1 (CCPG1) was shown to interact with FIP200 via two distinct regions (FIR1 and FIR2) that resemble yeast Atg11 binding regions (see section 5.3). Interestingly, CCPG1 binds to Atg8-like GABARAP via a LIR motif that is not required for interaction with FIP200. This is in contrast to the yeast Atg30-Atg11 (Farré et al. 2013) and the human FIP200-p62 (Turco et al., 2019) systems, where binding to the receptor LIR and FIR has been shown to be mutually exclusive and proposed to drive the progression from cargo sequestration towards membrane engulfment. For CCPG1-mediated ER-phagy, this step must be accomplished differently. How this process could be regulated through CCPG1 remains unclear. Unfortunately, no information on CCPG1 phosphorylation and its implications in receptor function is available yet. However, S104 located in the FIR motif is a putative phosphorylation site possibly relevant for regulation.

Two studies published in parallel to Turco et al. (2019) describe the interaction of cargo receptor NDP52 with FIP200. Ravenhill et al. (2019) showed that FIP200 forms a trimeric complex with cargo receptor NDP52 and TANK-binding kinase 1 (TBK1) adaptors SINTBAD or NAP1 during selective autophagy of *Salmonella* Typhimurium. SINTBAD specifically interacts with residues 1568 - 1582 located in FIP200 CTR loop 5 that was also identified as a crucial determinant for p62 interaction in this study. Remarkably, SINTBAD binds to FIP200 through residues that resemble the yeast Atg11 binding region (see section 5.3), similar to the

CCPG1 – FIP200 interaction. Vargas et al. (2019) described that NDP52, in contrast to p62, binds a FIP200 leucine zipper motif upstream of the CTR during mitophagy. Both studies suggest that the NDP52 LIR motif is not required for binding to FIP200, but that the NDP52 SKICH domain mediates the interaction.

Despite some similarities, there are notable differences in the interaction modes of the cargo receptors p62, CCPG1 and NDP52 with FIP200 that might reflect the requirement for specificity. However, further information on the described interactions and on interactions of FIP200 with different receptors will help to understand mammalian cargo recognition better.

5.5 Regulatory role of receptor oligomerization

Recent investigations showed that ubiquitin-bound p62 assembles in biomolecular condensates generated by liquid-liquid phase separation (Sun et al., 2018; Zaffagnini et al., 2018). Biomolecular condensates can be described as liquid-like sub-cellular compartments that serve specific functions and contain up to hundreds of different proteins (Banani et al., 2017). Their formation is driven by cooperative low-affinity contacts between static scaffold and mobile client proteins. Polymerization and post-translational modifications positively influence interactions within these dynamic networks (Wu and Fuxreiter, 2016). Phase transition of the cellular liquid droplets, however, can also lead to cluster or aggregate formation as seen in amyloid fibers (Wu and Fuxreiter, 2016). p62 condensates have been shown to accumulate under defective autophagy conditions and are linked to various neurodegenerative diseases (Ma et al., 2019).

Its oligomerization mode makes p62 a perfect filamentous scaffold for biomolecular condensates. The polymerizing N-terminal PB1 domain is located at the core of the p62 filament, while the C-terminal domains are accessible for different binding partners like ubiquitin, LC3B or FIP200 (Ciuffa et al. 2015, see section 1.4.3).

Oligomerization of p62 has been shown to be necessary for tight binding to LC3B-coated surfaces and membrane bending (Itakura and Mizushima, 2011; Wurzer et al., 2015). Furthermore, simultaneous binding of multiple LIR motifs on the p62 filament to LC3B stabilizes the interaction on the phagophore due to low off-rates (Wurzer et

al., 2015). p62 variants incapable of oligomerizing still bind to LC3B, however, they dissociate quickly, resulting in unstable aggregates. Similarly, the yeast Atg19 receptor interacts with Atg8 via multiple LIR motifs located at the protein's C-terminus (Abert et al., 2016; Sawa-Makarska et al., 2014). p62 oligomerization has also been described as an important feature during clustering of mitochondria in mitophagy (Narendra et al., 2010; Okatsu et al., 2010). Other selective autophagy receptors, like OPTN or NBR1, polymerize as well (Kirkin et al., 2009b; Ying et al., 2010). Notably, a recent study showed that receptor oligomerization is crucial for the pathway choice between ubiquitin-proteasome and autophagy degradation systems (Lu et al., 2017). Taken together, autophagy receptors are not only scaffolds for cargo proteins, but also act as multivalent binding partners for downstream autophagy effectors.

In line with this, the present study shows that FIP200 CTR can only bind to p62 FIR that is arranged in an oligomerization-like state. No binding was detectable employing solution-based interaction studies like ITC (Figure 26). However, assays where p62 FIR was adhered to a surface, like equilibrium binding analysis on sepharose beads (Figure 25D) or SPR (Figure 27), showed a robust interaction of the two proteins. Still, p62 FIR immobilization alone was not sufficient for the interaction, but it had to be concentrated to high densities as shown by SPR (Figure 28). Close spatial availability of p62 binding sites enhanced avidity-driven interaction of FIP200 CTR and p62 FIR.

This study supports the emerging view that oligomerization, as a mean to promote multivalent interactions, is a recurring regulatory mechanism in selective autophagy.

5.6 Structural model of full-length FIP200 suggests role as a tethering factor

5.6.1 Developing a model for full-length FIP200

In this study, the function of the C-terminal FIP200 Claw domain has been determined to be cargo receptor recognition during selective autophagy. As part of the ULK complex, FIP200 probably plays a crucial role in signaling to the kinase and initiating isolation membrane formation. How is the signal mediated and what is the role of the remaining 1450 N-terminal amino acids of FIP200?

As shown in Figure 36A, several predicted coiled-coil regions comprise the C-terminal half of FIP200, up to the Atg11 homolog domain. The N-terminal part harbors an Atg17-like and several unstructured regions. Although Atg17 is not conserved among eukaryotes, the Atg17-like region, comprising roughly 170 amino acids, shares weak sequence similarity in different species, suggesting a common functional role (Figure 36B; Li, Chung, and Vierstra 2014). The crystal structure of Atg17 can help in proposing a structural model for full length FIP200. Interestingly, Atg17 and FIP200 CTR reveal distinct dimerization modes. While Atg17 forms an anti-parallel dimer (Figure 36C, top), FIP200 CTR adopts a parallel dimerization mode (Figure 36D). At first, combining those in one assembly seems counterintuitive. A closer look on Atg17, however, reveals that the C-termini of the Atg17 dimer are in close proximity to each other (Figure 36C, bottom) and could easily be extended C-terminally by a linker into a dimeric coiled-coil protein. Importantly, the conserved residues of the Atg17-like region are located in the dimerization interface (Figure 36C, middle). A similar homotypic interaction is hence very likely for FIP200 and leads me to proposing a structural model for full length FIP200 (Figure 36E).

In this model, FIP200 forms a homodimeric extended coiled-coil. The N-terminal part harbors a binding site for the remaining components of the ULK1 complex and possibly ATG9-vesicles, similar to the situation in Atg17. The globular C-terminus interacts with selective autophagy cargo receptors, while the central coiled-coil region has been shown to bind to ATG16L1, a component of the E3 conjugation enzyme required for attaching LC3B to the isolation membrane (Gammoh et al., 2013; Nishimura et al., 2013).

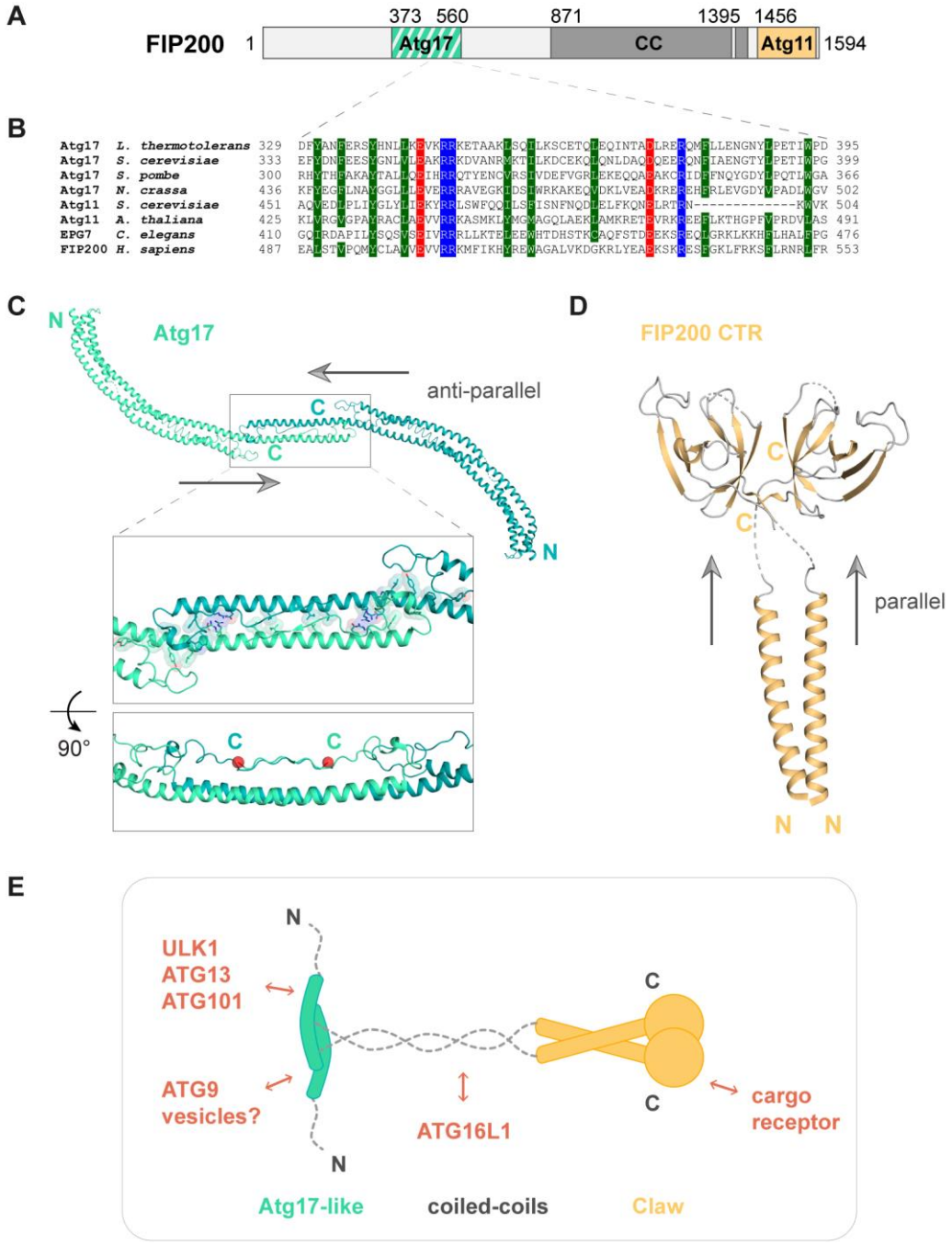

Figure 36. Developing a structural model for full-length FIP200. A) Schematic view of FIP200 sequence indicating conserved and structural motifs. B) Sequence alignment of Atg17-like regions from following species (UniProt accession code in parentheses). *L. thermotolerans* Atg17 (C5DFJ6), *S. cerevisiae* Atg17 (Q06410), *S. pombe* Atg17 (O42651), *N. crassa* Atg17 (Q872W1), *S. cerevisiae* Atg11 (Q12527), *A. thalania* Atg11 (Q9SUG7), *C. elegans* EPG7 (Q22342), *H. sapiens* FIP200 (Q8TDY2), Residues with a conservation greater than 80% are color-coded (D, E in red; R, K, H in blue N, Q, S, T, G, P in gray; A, L, I, V, F, Y, W, M, C in green) C) Structure of Atg17 (PDB code: 4HPQ) highlighting its antiparallel dimeric arrangement (top). Close-up of the C-terminal dimerization interface with conserved residues from the Atg17-like region alignment in B) shown as sticks and spheres (top view, middle). Side view of the dimerization interface with C-terminal C-alpha atoms depicted as red spheres (bottom). C) Structure of FIP200 CTR highlighting its parallel dimeric arrangement. E) Schematic model of full-length FIP200. Binding partners indicated in red.

The described model would allow FIP200 to simultaneously bind to cargo receptors, membrane vesicles and the autophagy core machinery. How exactly crosstalk between the Claw and the spatially distant ULK1 kinase is accomplished remains to be investigated. A recent report indicates that proximity of several copies of ULK1 would allow the kinase to autophosphorylate itself *in trans* and initiate isolation membrane formation (Kamber et al., 2015). p62 oligomers could thereby indirectly mediate clustering and activation of ULK1 via FIP200 bridging.

5.6.2 FIP200 - a membrane tethering factor?

The model of FIP200 described here is reminiscent to that of vesicle tethering factors, for example, from endocytic transport. Tethering factors mediate vesicle transport and localization by bridging vesicle and target membranes. Examples are p115 (Striegl et al., 2009) or EEA1 (Dumas et al., 2001), that form long dimeric coiled-coiled structures and use globular head domains to interact with the membrane either directly via lipids (EEA1) or indirectly via membrane-bound receptors (p115).

Strikingly, the FIP200 yeast counterparts Atg11 and Atg17 have been connected to processes involving vesicle transport, in which they recruit Atg9 to the PAS (He et al. 2006; Sekito et al. 2009). Atg17 binds to Atg9-vesicles by direct interaction with Atg9 and accommodation of the membrane vesicles in its dimeric crescent (Ragusa et al., 2012; Rao et al., 2016). For Atg11, Atg9 recruitment could be achieved through the interaction with the GTPase Ypt1 (Rab1 in humans) that is required for membrane trafficking in the Golgi-endosomal system (Lipatova et al., 2015) and, specifically, for Atg9 vesicle transport. Interestingly, PAS formation relies on the Ypt1 - Atg11 interaction (Lipatova et al., 2012). Moreover, Atg11 has been described as a peripheral membrane protein (Kim et al., 2001) and harbors an Atg17-like region. In humans, FIP200-deficient cells lack isolation membrane formation (Kishi-Itakura et al., 2014), suggesting a role for FIP200 in membrane recruitment.

Here, it was shown for the first time that the FIP200 Claw domain binds directly to membranes *in vitro* (Figure 30). Constructs comprising the N-terminal helices in addition to the Claw exhibited an enhanced interaction. This observation is intriguing as it corroborates the concept of FIP200 being involved in membrane tethering. In the model suggested in Figure 36E, I propose that the N-terminal part of FIP200 might

interact with ATG9 vesicles, while the Claw domain engages in cargo receptor interactions. Besides receptor binding, the Claw domain could exert an autoinhibitory function on FIP200 by folding back to the vesicle membrane during recruitment to the p62 condensates.

Direct localization of FIP200 to the isolation membrane might be necessary for autophagy protein recruitment after FIP200 has been replaced by LC3B. In this way, it could further assist in membrane elongation. For example, FIP200 interacts with ATG16L1, a protein that is part of the E3 conjugation enzyme required for attaching LC3B to the isolation membrane (Nishimura et al., 2013). Additional accessory proteins can also be recruited indirectly via FIP200's binding partners in the ULK1 complex.

Up to date, there is no detailed information on how FIP200, Atg11 or Atg17 are attached to the phagophore membrane and what triggers their displacement. Interestingly, Atg17 and Atg11 are also involved in autophagosome fusion with the lysosome in yeast by independently recruiting the SNARE protein Vam7 (Liu et al., 2016) via their coiled-coil regions. They are suggested to have an inhibitory effect on fusion as long as the phagophore is still immature. Upon maturation, Vam7 is probably released from Atg11/Atg17 to engage in interactions with SNAREs located on the lysosome, driving the fusion process. In order to locate Vam7 to the phagophore, Atg11/Atg17 still have to be located at the membrane after cargo recognition. This might be mediated by the Claw domain. However, as Atg17 does not have an Atg11-homology domain, there still must be other factors responsible for phagophore targeting.

To sum up, membrane binding of FIP200 could be required for several processes: (1) Recruitment of ATG9 vesicles or other membrane sources to the isolation membrane. (2) Stabilization of FIP200 on the isolation membrane or phagophore. (3) Involvement in fusion events with the lysosome. Further experiments are necessary to validate the FIP200 membrane interaction. Detailed information on the preferred membrane composition could help to understand the driving forces behind binding. Since no interaction with inositol phosphates has been observed so far (Figure 30), it can be speculated that FIP200 CTR binds to negatively charged phosphatidylserines. To rule out non-specific negative charge interactions, cellular

membrane localization assays are crucial for verification of the observations made here.

5.7 Mechanism for FIP200-mediated selective autophagy cargo sequestration

Based on the structural, biochemical and biophysical data outlined in this thesis, as well as published data on autophagy, I propose a model for selective autophagy initiation mediated by FIP200 cargo receptor recognition (Figure 37).

FIP200 bound to ATG9 vesicles is recruited to p62 condensates upon p62 oligomerization and phosphorylation. Before p62 interaction, FIP200 could adopt an autoinhibitory conformation by folding back the Claw domain to vesicles located at the FIP200 N-terminus or by self-interaction. In case of autoinhibition, structural rearrangements in FIP200 would be necessary to allow Claw domain – p62 FIR interaction (1). Together with FIP200, the remaining members of the ULK1 complex are delivered to the isolation membrane initiation site. Upon binding of FIP200 to phosphorylated p62 filaments, the autophagy core machinery is localized at high local concentrations around the cargo (2). ULK1 autophosphorylation in *trans* induces recruitment of further autophagy components and formation of the isolation membrane. Once LC3B has been linked to the membrane, it displaces FIP200 from p62 (3). FIP200 might then be retained at the membrane rim via the Claw domain to further locate the autophagy core machinery and drive LC3B lipidation and membrane elongation, or it could be recycled for further vesicle recruitment.

The proposed mechanism highlights the importance of FIP200 as a scaffold protein in forming a link between cargo receptor recognition and autophagy machinery recruitment. Additionally, it integrates knowledge on scaffold - membrane interactions. How exactly membrane recruitment by FIP200 is accomplished needs to be addressed in further studies.

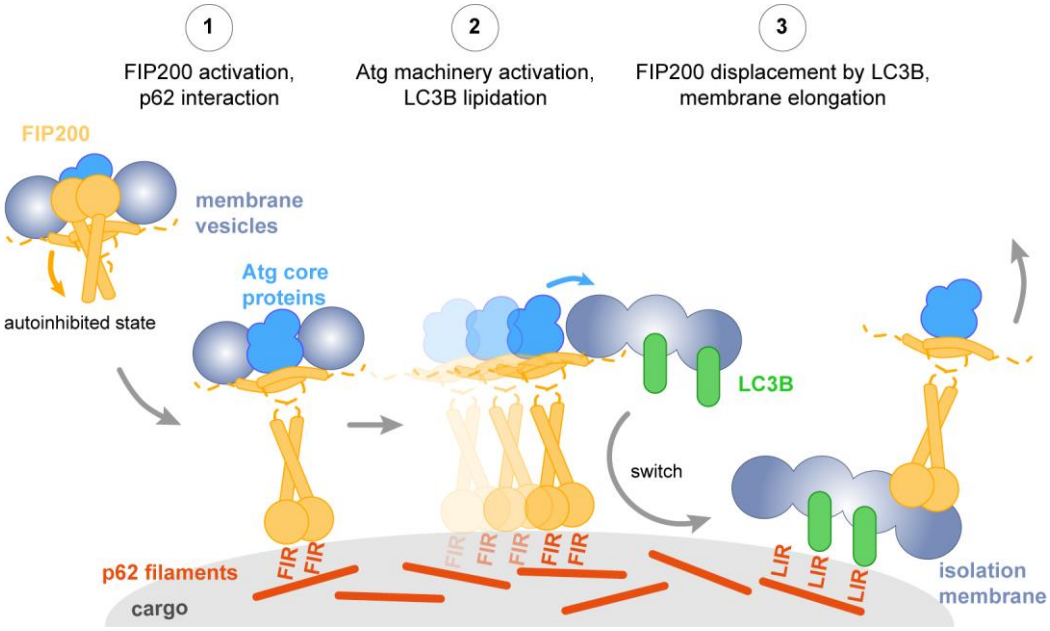

Figure 37. Model for FIP200-mediated selective autophagy initiation. (1) Autoinhibited FIP200 bound to ATG9 vesicles is recruited to p62 condensates upon p62 oligomerization and phosphorylation. Structural rearrangements in FIP200 allow for Claw domain – p62 FIR interaction. (2) Localization of FIP200 at the p62 condensate activates the autophagic core machinery, triggering a cascade of events that culminates in LC3B conjugation to the forming isolation membrane. (3) LC3B displaces FIP200 from p62 and thereby tightly links the growing membrane to the condensate. FIP200 might be recycled or stays at the rim of the phagophore to further promote membrane elongation.

5.8 Concluding remarks

Phosphorylation and oligomerization have been proposed to play critical roles in selective autophagy (Khaminets et al., 2016). The results of this thesis underscore the relevance of these mechanisms for the interaction between cargo receptor and core components of the autophagic machinery.

The requirement of p62 oligomerization for forming an interaction with FIP200 has been complicating biochemical and structural studies so far. However, especially information on higher order assemblies of the macromolecular complexes will be required to understand selective autophagy. The latest advances in high resolution light and (cryo-)electron microscopy will help to shed further light on autophagy by providing time-resolved and near-atomic resolution information. Investigation of the filamentous p62 in complex with FIP200 and ubiquitin by cryo-electron microscopy, for example, could deliver valuable information on condensate structure and recognition. Ubiquitin chains would restrict the filament to small size, making the

sample more homogenous and perhaps suitable for cryo-EM. Moreover, cryo-electron microscopy could help to elucidate how full length FIP200 assembles on membranes or ATG9 vesicles. Finally, the assembly of the entire ULK1 complex would be highly interesting to further understand autophagy initiation.

This work described a molecular link between selective autophagy cargo recognition and autophagy initiation and contributes to understanding evolutionally conserved concepts of cellular waste recycling.

6. References

Abbi, S., Ueda, H., Zheng, C., Cooper, L.A., Zhao, J., Christopher, R., and Guan, J. (2002). Regulation of focal adhesion kinase by a novel protein inhibitor FIP200. Mol. Biol. Cell *13*, 3178–3191.

Abert, C., Kontaxis, G., and Martens, S. (2016). Accessory interaction motifs in the Atg19 cargo receptor enable strong binding to the clustered ubiquitin-related Atg8 protein. J. Biol. Chem. *291*, 18799–18808.

Adams, P.D., Afonine, P. V., Bunkóczi, G., Chen, V.B., Davis, I.W., Echols, N., Headd, J.J., Hung, L.W., Kapral, G.J., Grosse-Kunstleve, R.W., et al. (2010). PHENIX: A comprehensive Python-based system for macromolecular structure solution. Acta Crystallogr. Sect. D Biol. Crystallogr. *66*, 213–221.

Alemu, E.A., Lamark, T., Torgersen, K.M., Birgisdottir, A.B., Larsen, K.B., Jain, A., Olsvik, H., Øvervatn, A., Kirkin, V., and Johansen, T. (2012). ATG8 family proteins act as scaffolds for assembly of the ULK complex: Sequence requirements for LC3-interacting region (LIR) motifs. J. Biol. Chem. *287*, 39275–39290.

Aoki, Y., Kanki, T., Hirota, Y., Kurihara, Y., Saigusa, T., Uchiumi, T., and Kang, D. (2011). Phosphorylation of Serine 114 on Atg32 mediates mitophagy. Mol. Biol. Cell *22*, 3206–3217.

Apel, A., Herr, I., Schwarz, H., Rodemann, H.P., and Mayer, A. (2008). Blocked autophagy sensitizes resistant carcinoma cells to radiation therapy. Cancer Res. *68*, 1485–1494.

Arcus, V. (2002). OB-fold domains: A snapshot of the evolution of sequence, structure and function. Curr. Opin. Struct. Biol. *12*, 794–801.

Ashford, T.P., and Porter, K.R. (1962). Cytoplasmic components in hepatic cell lysosomes. J. Cell Biol. *12*, 198–202.

Ashkenazy, H., Abadi, S., Martz, E., Chay, O., Mayrose, I., Pupko, T., and Ben-Tal, N. (2016). ConSurf 2016: an improved methodology to estimate and visualize evolutionary conservation in macromolecules. Nucleic Acids Res. *44*, W344–W350.

Backer, J.M. (2008). The regulation and function of Class III PI3Ks: novel roles for Vps34. Biochem. J. *410*, 1–17.

Bae, W., Xia, B., Inouye, M., and Severinov, K. (2000). *Escherichia coli* CspA-family RNA chaperones are transcription antiterminators. Proc. Natl. Acad. Sci. U. S. A. *97*, 7784–7789.

Banani, S.F., Lee, H.O., Hyman, A.A., and Rosen, M.K. (2017). Biomolecular condensates: Organizers of cellular biochemistry. Nat. Rev. Mol. Cell Biol. *18*, 285–298.

Bento, C.F., Renna, M., Ghislat, G., Puri, C., Ashkenazi, A., Vicinanza, M., Menzies, F.M., and Rubinsztein, D.C. (2016). Mammalian Autophagy: How Does It Work? Annu. Rev. Biochem. *85*, 685–713.

Birgisdottir, Å.B., Lamark, T., and Johansen, T. (2013). The LIR motif – crucial for selective autophagy. J. Cell Sci. *126*, 3237 LP-3247.

Bjørkøy, G., Lamark, T., Brech, A., Outzen, H., Perander, M., Øvervatn, A., Stenmark, H., and Johansen, T. (2005). p62/SQSTM1 forms protein aggregates degraded by autophagy and has a protective effect on huntingtin-induced cell death. J. Cell Biol. *171*, 603–614.

Boutouja, F., Stiehm, C., Platta, H., Boutouja, F., Stiehm, C.M., and Platta, H.W. (2019). mTOR: A cellular regulator interface in health and disease. Cells *8*, 18.

Buchan, D.W.A., Minneci, F., Nugent, T.C.O., Bryson, K., and Jones, D.T. (2013). Scalable web services for the PSIPRED Protein Analysis Workbench. Nucleic Acids Res. *41*.

Cha-Molstad, H., Yu, J.E., Feng, Z., Lee, S.H., Kim, J.G., Yang, P., Han, B., Sung, K.W., Yoo, Y.D., Hwang, J., et al. (2017). p62/SQSTM1/Sequestosome-1 is an N-recognin of the N-end rule pathway which modulates autophagosome biogenesis. Nat. Commun. *8*, 102.

Chan, E.Y. (2009). MTORC1 phosphorylates the ULK1-mAtg13-FIP200 autophagy regulatory complex. Sci. Signal. *2*, pe51.

Cheong, H., Nair, U., Geng, J., and Klionsky, D.J. (2008). The Atg1 kinase complex is involved in the regulation of protein recruitment to initiate sequestering vesicle formation for nonspecific autophagy in Saccharomyces cerevisiae. Mol. Biol. Cell *19*, 668–681.

Ciuffa, R., Lamark, T., Tarafder, A.K., Guesdon, A., Rybina, S., Hagen, W.J.H., Johansen, T., and Sachse, C. (2015). The selective autophagy receptor p62 forms a flexible filamentous helical scaffold. Cell Rep. *11*, 748–758.

Clarke, A.J., and Simon, A.K. (2019). Autophagy in the renewal, differentiation and homeostasis of immune cells. Nat. Rev. Immunol. *19*, 170–183.

Davis, I.W., Leaver-Fay, A., Chen, V.B., Block, J.N., Kapral, G.J., Wang, X., Murray, L.W., Arendall, W.B., Snoeyink, J., Richardson, J.S., et al. (2007). MolProbity: All-atom contacts and structure validation for proteins and nucleic acids. Nucleic Acids Res. *35*, W375–383.

DeLano, W.L. (2014). The PyMOL Molecular Graphics System, Version 1.8. Schrödinger LLC http://www.pymol.org.

Deosaran, E., Larsen, K.B., Hua, R., Sargent, G., Wang, Y., Kim, S., Lamark, T., Jauregui, M., Law, K., Lippincott-Schwartz, J., et al. (2013). NBR1 acts as an autophagy receptor for peroxisomes. J. Cell Sci. *126*, 939–952.

DePristo, M.A., De Bakker, P.I.W., and Blundell, T.L. (2004). Heterogeneity and inaccuracy in protein structures solved by X-ray crystallography. Structure *12*, 831–838.

Dikic, I. (2017). Proteasomal and autophagic degradation systems. Annu. Rev. Biochem. *86*, 193–224.

Dikic, I., and Elazar, Z. (2018). Mechanism and medical implications of mammalian autophagy. Nat. Rev. Mol. Cell Biol. *19*, 349–364.

Dooley, H.C., Razi, M., Polson, H.E.J., Girardin, S.E., Wilson, M.I., and Tooze, S.A. (2014). WIPI2 links LC3 conjugation with PI3P, autophagosome formation, and pathogen clearance by recruiting Atg12-5-16L1. Mol. Cell *55*, 238–252.

Doublié, S. (1997). Preparation of selenomethionyl proteins for phase determination. In Macromolecular Crystallography Part A, (Academic Press), pp. 523–530.

Dumas, J.J., Merithew, E., Sudharshan, E., Rajamani, D., Hayes, S., Lawe, D., Corvera, S., and Lambright, D.G. (2001). Multivalent endosome targeting by homodimeric EEA1. Mol. Cell *8*, 947–958.

de Duve, C., and Wattiaux, R. (1966). Functions of lysosomes. Annu. Rev. Physiol. *28*, 435–492.

Emsley, P., Lohkamp, B., Scott, W.G., and Cowtan, K. (2010). Features and development of Coot. Acta Crystallogr. Sect. D Biol. Crystallogr. *66*, 486–501.

Farré, J.C., and Subramani, S. (2016). Mechanistic insights into selective autophagy pathways: Lessons from yeast. Nat. Rev. Mol. Cell Biol. *17*, 537–552.

Farré, J.C., Manjithaya, R., Mathewson, R.D., and Subramani, S. (2008). PpAtg30 tags peroxisomes for turnover by selective autophagy. Dev. Cell *14*, 365–376.

Farré, J.C., Burkenroad, A., Burnett, S.F., and Subramani, S. (2013). Phosphorylation of mitophagy and pexophagy receptors coordinates their interaction with Atg8 and Atg11. EMBO Rep. *14*, 441–449.

Fox, N.K., Brenner, S.E., and Chandonia, J.M. (2014). SCOPe: Structural Classification of Proteins - Extended, integrating SCOP and ASTRAL data and classification of new structures. Nucleic Acids Res. *42*.

Gammoh, N., Florey, O., Overholtzer, M., and Jiang, X. (2013). Interaction between FIP200 and ATG16L1 distinguishes ULK1 complex-dependent and -independent autophagy. Nat. Struct. Mol. Biol. *20*, 144–149.

Gan, B., and Guan, J.L. (2008). FIP200, a key signaling node to coordinately regulate various cellular processes. Cell. Signal. *20*, 787–794.

Gan, B., Melkoumian, Z.K., Wu, X., Guan, K.-L., and Guan, J.-L. (2005). Identification of FIP200 interaction with the TSC1-TSC2 complex and its role in regulation of cell size control. J. Cell Biol. *170*, 379–389.

Ganley, I.G., Lam, D.H., Wang, J., Ding, X., Chen, S., and Jiang, X. (2009). ULK1·ATG13·FIP200 complex mediates mTOR signaling and is essential for autophagy. J. Biol. Chem. *284*, 12297–12305.

Gasteiger, E., Hoogland, C., Gattiker, A., Duvaud, S., Wilkins, M.R., Appel, R.D., and Bairoch, A. (2005). Protein Identification and Analysis Tools on the ExPASy Server. In The Proteomics Protocols Handbook, (Humana Press), p.

Gruss, F., Zähringer, F., Jakob, R.P., Burmann, B.M., Hiller, S., and Maier, T. (2013). The structural basis of autotransporter translocation by TamA. Nat. Struct. Mol. Biol. *20*, 1318–1320.

Guo, J.Y., Chen, H.Y., Mathew, R., Fan, J., Strohecker, A.M., Karsli-Uzunbas, G., Kamphorst, J.J., Chen, G., Lemons, J.M.S., Karantza, V., et al. (2011). Activated Ras requires autophagy to maintain oxidative metabolism and tumorigenesis. Genes Dev. *25*, 460–470.

Hara, T., and Mizushima, N. (2009). Role of ULK-FIP200 complex in mammalian autophagy: FIP200, a counterpart of yeast Atg17? Autophagy *5*, 85–87.

Hara, T., Nakamura, K., Matsui, M., Yamamoto, A., Nakahara, Y., Suzuki-Migishima, R., Yokoyama, M., Mishima, K., Saito, I., Okano, H., et al. (2006). Suppression of basal autophagy in neural cells causes neurodegenerative disease in mice. Nature *441*, 885–889.

Hara, T., Takamura, A., Kishi, C., Iemura, S.-I., Natsume, T., Guan, J.-L., and Mizushima, N. (2008). FIP200, a ULK-interacting protein, is required for autophagosome formation in mammalian cells. J. Cell Biol. *181*, 497–510.

He, C., Song, H., Yorimitsu, T., Monastyrska, I., Yen, W.L., Legakis, J.E., and Klionsky, D.J. (2006). Recruitment of Atg9 to the preautophagosomal structure by Atg11 is essential for selective autophagy in budding yeast. J. Cell Biol. *175*, 925–935.

Horn, G., Hofweber, R., Kremer, W., and Kalbitzer, H.R. (2007). Structure and function of bacterial cold shock proteins. Cell. Mol. Life Sci. *64*, 1457–1470.

Horos, R., Büscher, M., Kleinendorst, R., Alleaume, A.-M., Tarafder, A.K., Schwarzl, T., Dziuba, D., Tischer, C., Zielonka, E.M., Adak, A., et al. (2019). The Small Non-coding Vault RNA1-1 Acts as a Riboregulator of Autophagy. Cell *176*, 1054–1067.e12.

Hosokawa, N., Hara, T., Kaizuka, T., Kishi, C., Takamura, A., Miura, Y., Iemura, S., Natsume, T., Takehana, K., Yamada, N., et al. (2009). Nutrient-dependent mTORC1 Association with the ULK1 – Atg13 – FIP200 Complex Required for Autophagy. Mol. Biol. Cell *20*, 1981–1991.

Høyer-Hansen, M., and Jäättelä, M. (2007). AMP-activated protein kinase: A universal regulator of autophagy? Autophagy *3*, 381–383.

Hundsrucker, C., Krause, G., Beyermann, M., Prinz, A., Zimmermann, B., Diekmann, O., Lorenz, D., Stefan, E., Nedvetsky, P., Dathe, M., et al. (2006). High-affinity AKAP7δ–protein kinase A interaction yields novel protein kinase A-anchoring disruptor peptides. Biochem. J. *396*, 297–306.

Hyman, A.A., Weber, C.A., and Jülicher, F. (2014). Liquid-Liquid Phase Separation in Biology. Annu. Rev. Cell Dev. Biol. *30*, 39–58.

Ichimura, Y., Kumanomidou, T., Sou, Y.S., Mizushima, T., Ezaki, J., Ueno, T., Kominami, E., Yamane, T., Tanaka, K., and Komatsu, M. (2008a). Structural basis for sorting mechanism of p62 in selective autophagy. J. Biol. Chem. *283*, 22847–22857.

Ichimura, Y., Kominami, E., Tanaka, K., and Komatsu, M. (2008b). Selective turnover of p62/A170/SQSTM1 by autophagy. Autophagy *4*, 1063–1066.

Ichimura, Y., Waguri, S., Sou, Y. shin, Kageyama, S., Hasegawa, J., Ishimura, R., Saito, T., Yang, Y., Kouno, T., Fukutomi, T., et al. (2013). Phosphorylation of p62 Activates the Keap1-Nrf2 Pathway during Selective Autophagy. Mol. Cell *51*, 618–631.

Itakura, E., and Mizushima, N. (2011). p62 targeting to the autophagosome formation site requires self-oligomerization but not LC3 binding. J. Cell Biol. *192*, 17–27.

Jardetzky, T.S., Brown, J.H., Gorga, J.C., Stern, L.J., Urban, R.G., Chi, Y., Stauffacher, C., Strominger, J.L., and Wiley, D.C. (1994). Three-dimensional structure of a human class II histocompatibility molecule complexed with superantigen. Nature *368*, 711–718.

Johansen, T., and Lamark, T. (2011). Selective autophagy mediated by autophagic adapter proteins. Autophagy *7*, 279–296.

Jung, C.H., Jun, C.B., Ro, S.-H., Kim, Y.-M., Otto, N.M., Cao, J., Kundu, M., and Kim, D.-H. (2009). ULK-Atg13-FIP200 Complexes Mediate mTOR Signaling to the Autophagy Machinery. Mol. Biol. Cell *20*, 1992–2003.

Kabeya, Y. (2004). LC3, GABARAP and GATE16 localize to autophagosomal membrane depending on form-II formation. J. Cell Sci. *117*, 2805–2812.

Kabsch, W. (2010). XDS. Acta Crystallogr. Sect. D Biol. Crystallogr. *66*, 125–132.

Kamada, Y., Funakoshi, T., Shintani, T., Nagano, K., Ohsumi, M., and Ohsumi, Y. (2000). Tor-mediated induction of autophagy via an Apg1 protein kinase complex. J. Cell Biol. *150*, 1507–1513.

Kamber, R.A., Shoemaker, C.J., and Denic, V. (2015). Receptor-Bound Targets of Selective Autophagy Use a Scaffold Protein to Activate the Atg1 Kinase. Mol. Cell *59*, 372–381.

Kanamaru, S., Leiman, P.G., Kostyuchenko, V.A., Chipman, P.R., Mesyanzhinov, V. V., Arisaka, F., and Rossmann, M.G. (2002). Structure of the cell-puncturing device of bacteriophage T4. Nature *415*, 553–557.

Kanki, T., and Klionsky, D.J. (2008). Mitophagy in yeast occurs through a selective mechanism. J. Biol. Chem. *283*, 32386–32393.

Kanki, T., Wang, K., Cao, Y., Baba, M., and Klionsky, D.J. (2009). Atg32 Is a Mitochondrial Protein that Confers Selectivity during Mitophagy. Dev. Cell *17*, 98–109.

Kaur, J., and Debnath, J. (2015). Autophagy at the crossroads of catabolism and anabolism. Nat. Rev. Mol. Cell Biol. *16*, 461–472.

Khaminets, A., Heinrich, T., Mari, M., Grumati, P., Huebner, A.K., Akutsu, M., Liebmann, L., Stolz, A., Nietzsche, S., Koch, N., et al. (2015). Regulation of endoplasmic reticulum turnover by selective autophagy. Nature *522*, 354–358.

Khaminets, A., Behl, C., and Dikic, I. (2016). Ubiquitin-Dependent And Independent Signals In Selective Autophagy. Trends Cell Biol. *26*, 6–16.

Kim, J., Kamada, Y., Stromhaug, P.E., Guan, J., Hefner-Gravink, A., Baba, M., Scott, S. V., Ohsumi, Y., Dunn, W.A., and Klionsky, D.J. (2001). Cvt9/Gsa9 functions in sequestering selective cytosolic cargo destined for the vacuole. J. Cell Biol. *153*, 381–396.

Kirkin, V., McEwan, D.G., Novak, I., and Dikic, I. (2009a). A Role for Ubiquitin in Selective Autophagy. Mol. Cell *34*, 259–269.

Kirkin, V., Lamark, T., Sou, Y.S., Bjørkøy, G., Nunn, J.L., Bruun, J.A., Shvets, E., McEwan, D.G., Clausen, T.H., Wild, P., et al. (2009b). A Role for NBR1 in Autophagosomal Degradation of Ubiquitinated Substrates. Mol. Cell *33*, 505–516.

Kishi-Itakura, C., Koyama-Honda, I., Itakura, E., and Mizushima, N. (2014). Ultrastructural analysis of autophagosome organization using mammalian autophagy-deficient cells. J. Cell Sci. *127*, 4089–4102.

Klionsky, D.J., Abdelmohsen, K., Abe, A., Abedin, M.J., Abeliovich, H., Arozena, A.A., Adachi, H., Adams, C.M., Adams, P.D., Adeli, K., et al. (2016). Guidelines for the use and interpretation of assays for monitoring autophagy (3rd edition). Autophagy *12*, 1–222.

Komatsu, M., Waguri, S., Chiba, T., Murata, S., Iwata, J.I., Tanida, I., Ueno, T., Koike, M., Uchiyama, Y., Kominami, E., et al. (2006). Loss of autophagy in the central nervous system causes neurodegeneration in mice. Nature *441*, 880–884.

Komatsu, M., Waguri, S., Koike, M., Sou, Y. shin, Ueno, T., Hara, T., Mizushima, N., Iwata, J. ichi, Ezaki, J., Murata, S., et al. (2007). Homeostatic Levels of p62 Control Cytoplasmic Inclusion Body Formation in Autophagy-Deficient Mice. Cell *131*, 1149–1163.

Komatsu, M., Kurokawa, H., Waguri, S., Taguchi, K., Kobayashi, A., Ichimura, Y., Sou, Y.S., Ueno, I., Sakamoto, A., Tong, K.I., et al. (2010). The selective autophagy substrate p62 activates the stress responsive transcription factor Nrf2 through inactivation of Keap1. Nat. Cell Biol. *12*, 213–223.

Krick, R., Tolstrup, J., Appelles, A., Henke, S., and Thumm, M. (2006). The relevance of the phosphatidylinositolphosphat-binding motif FRRGT of Atg18 and Atg21 for the Cvt pathway and autophagy. FEBS Lett. *580*, 4632–4638.

Krissinel, E., and Henrick, K. (2004). Secondary-structure matching (SSM), a new tool for fast protein structure alignment in three dimensions. Acta Crystallogr. Sect. D Biol. Crystallogr. *60*, 2256–2268.

Krissinel, E., and Henrick, K. (2007). Inference of macromolecular asssemblies from crystalline state. J. Mol. Biol. *372*, 774–797.

Krug, M., Weiss, M.S., Heinemann, U., and Mueller, U. (2012). XDSAPP: A graphical user interface for the convenient processing of diffraction data using XDS. J. Appl. Crystallogr. *45*, 568–572.

Kuma, A., Hatano, M., Matsui, M., Yamamoto, A., Nakaya, H., Yoshimori, T., Ohsumi, Y., Tokuhisa, T., and Mizushima, N. (2004). The role of autophagy during the early neonatal starvation period. Nature *432*, 1032–1036.

Lamark, T., and Johansen, T. (2012). Aggrephagy: Selective Disposal of Protein Aggregates by Macroautophagy. Int. J. Cell Biol. 1–21.

Lamark, T., Perander, M., Outzen, H., Kristiansen, K., Øvervatn, A., Michaelsen, E., Bjørkoy, G., and Johansen, T. (2003). Interaction Codes within the Family of Mammalian Phox and Bem1p Domain-containing Proteins. J. Biol. Chem. *278*, 34568–34581.

Levine, B., and Kroemer, G. (2019). Biological Functions of Autophagy Genes: A Disease Perspective. Cell *176*, 11–42.

Li, F., Chung, T., and Vierstra, R.D. (2014). AUTOPHAGY-RELATED11 Plays a Critical Role in General Autophagy- and Senescence-Induced Mitophagy in Arabidopsis. Plant Cell *26*, 788–807.

Liang, X.H., Jackson, S., Seaman, M., Brown, K., Kempkes, B., Hibshoosh, H., and Levine, B. (1999). Induction of autophagy and inhibition of tumorigenesis by beclin 1. Nature *402*, 672–676.

Lin, L., Yang, P., Huang, X., Zhang, H., Lu, Q., and Zhang, H. (2013). The scaffold protein EPG-7 links cargo-receptor complexes with the autophagic assembly machinery. J. Cell Biol. *201*, 113–129.

Ling, H., Boodhoo, A., Hazes, B., Cummings, M.D., Armstrong, G.D., Brunton, J.L., and Read, R.J. (1998). Structure of the Shiga-like toxin I B-pentamer complexed with an analogue of its receptor Gb3. Biochemistry *37*, 1777–1788.

Lipatova, Z., Belogortseva, N., Zhang, X.Q., Kim, J., Taussig, D., and Segev, N. (2012). Regulation of selective autophagy onset by a Ypt/Rab GTPase module. Proc. Natl. Acad. Sci. *109*, 6981 LP-6986.

Lipatova, Z., Hain, A.U., Nazarko, V.Y., and Segev, N. (2015). Ypt/Rab GTPases: Principles learned from yeast. Crit. Rev. Biochem. Mol. Biol. *50*, 203–211.

Liu, L., Feng, D., Chen, G., Chen, M., Zheng, Q., Song, P., Ma, Q., Zhu, C., Wang, R., Qi, W., et al. (2012). Mitochondrial outer-membrane protein FUNDC1 mediates hypoxia-induced mitophagy in mammalian cells. Nat. Cell Biol. *14*, 177–185.

Liu, X., Mao, K., Yu, A.Y.H., Omairi-Nasser, A., Austin, J., Glick, B.S., Yip, C.K., and Klionsky, D.J. (2016). The Atg17-Atg31-Atg29 Complex Coordinates with Atg11 to Recruit the Vam7 SNARE and Mediate Autophagosome-Vacuole Fusion. Curr. Biol. *26*, 150–160.

Lock, R., Roy, S., Kenific, C.M., Su, J.S., Salas, E., Ronen, S.M., and Debnath, J. (2011). Autophagy facilitates glycolysis during Ras-mediated oncogenic transformation. Mol. Biol. Cell *22*, 165–178.

Long, J., Gallagher, T.R.A., Cavey, J.R., Sheppard, P.W., Ralston, S.H., Layfield, R., and Searle, M.S. (2008). Ubiquitin recognition by the ubiquitin-associated domain of p62 involves a novel conformational switch. J. Biol. Chem. *283*, 5427–5440.

López-Otín, C., Galluzzi, L., Freije, J.M.P., Madeo, F., and Kroemer, G. (2016). Metabolic Control of Longevity. Cell *166*, 802–821.

Lu, K., Psakhye, I., and Jentsch, S. (2014). Autophagic clearance of PolyQ proteins mediated by ubiquitin-Atg8 adaptors of the conserved CUET protein family. Cell *158*, 549–563.

Lu, K., Den Brave, F., and Jentsch, S. (2017). Receptor oligomerization guides pathway choice between proteasomal and autophagic degradation. Nat. Cell Biol. *19*, 732–739.

Lynch-Day, M.A., and Klionsky, D.J. (2010). The Cvt pathway as a model for selective autophagy. FEBS Lett. *584*, 1359–1366.

Ma, S., Attarwala, I., and Xie, X.-Q. (Sean) (2019). SQSTM1/p62: a potential target for neurodegenerative disease. ACS Chem. Neurosci.

Mari, M., Griffith, J., Rieter, E., Krishnappa, L., Klionsky, D.J., and Reggiori, F. (2010). An Atg9-containing compartment that functions in the early steps of autophagosome biogenesis. J. Cell Biol. *190*, 1005–1022.

Max, K.E.A., Zeeb, M., Bienert, R., Balbach, J., and Heinemann, U. (2006). T-rich DNA Single Strands Bind to a Preformed Site on the Bacterial Cold Shock Protein Bs-CspB. J. Mol. Biol. *360*, 702–714.

Melkoumian, Z.K., Peng, X., Gan, B., Wu, X., and Guan, J.L. (2005). Mechanism of cell cycle regulation by FIP200 in human breast cancer cells. Cancer Res. *65*, 6676–6684.

Méresse, S., Steele-Mortimer, O., Moreno, E., Desjardins, M., Finlay, B., and Gorvel, J.-P. (1999). Controlling the maturation of pathogen-containing vacuoles: a matter of life and death. Nat. Cell Biol. *1*, E183–E188.

Mihailovich, M., Militti, C., Gabaldón, T., and Gebauer, F. (2010). Eukaryotic cold shock domain proteins: Highly versatile regulators of gene expression. BioEssays *32*, 109–118.

Mizushima, N. (2007). Autophagy : process and function. Genes Dev. *21*, 2861–2873.

Mizushima, N., Noda, T., Yoshimori, T., Tanaka, Y., Ishii, T., George, M.D., Klionsky, D.J., Ohsumi, M., and Ohsumi, Y. (1998). A protein conjugation system essential for autophagy. Nature *395*, 395–398.

Mochida, K., Oikawa, Y., Kimura, Y., Kirisako, H., Hirano, H., Ohsumi, Y., and Nakatogawa, H. (2015). Receptor-mediated selective autophagy degrades the endoplasmic reticulum and the nucleus. Nature *522*, 359–362.

Mortimore, G.E., and Schworer, C.M. (1977). Induction of autophagy by amino-acid deprivation in perfused rat liver. Nature *270*, 174–176.

Moscat, J., Diaz-Meco, M.T., and Wooten, M.W. (2007). Signal integration and diversification through the p62 scaffold protein. Trends Biochem. Sci. *32*, 95–100.

Moscat, J., Karin, M., and Diaz-Meco, M.T. (2016). p62 in Cancer: Signaling Adaptor Beyond Autophagy. Cell *167*, 606–609.

Mueller, U., Förster, R., Hellmig, M., Huschmann, F.U., Kastner, A., Malecki, P., Pühringer, S., Röwer, M., Sparta, K., Steffien, M., et al. (2015). The macromolecular crystallography beamlines at BESSY II of the Helmholtz-Zentrum Berlin: Current status and perspectives. Eur. Phys. J. Plus *130*, 141.

Murzin, A.G. (1993). OB(oligonucleotide/oligosaccharide binding)-fold: common structural and functional solution for non-homologous sequences. EMBO J. *12*, 861–867.

Nakamura, S., and Yoshimori, T. (2017). New insights into autophagosome–lysosome fusion. J. Cell Sci. *130*, 1209–1216.

Nakamura, K., Kimple, A.J., Siderovski, D.P., and Johnson, G.L. (2010). PB1 domain interaction of p62/sequestosome 1 and MEKK3 regulates NF-κB activation. J. Biol. Chem. *285*, 2077–2089.

Nakatogawa, H., Suzuki, K., Kamada, Y., and Ohsumi, Y. (2009). Dynamics and diversity in autophagy mechanisms: Lessons from yeast. Nat. Rev. Mol. Cell Biol. *10*, 458–467.

Narendra, D.P., Kane, L.A., Hauser, D.N., Fearnley, I.M., and Youle, R.J. (2010). p62/SQSTM1 is required for Parkin-induced mitochondrial clustering but not mitophagy; VDAC1 is dispensable for both. Autophagy *6*, 1090–1106.

Nascimbeni, A.C., Codogno, P., and Morel, E. (2017). Phosphatidylinositol-3-phosphate in the regulation of autophagy membrane dynamics. FEBS J. *284*, 1267–1278.

Nishimura, T., Kaizuka, T., Cadwell, K., Sahani, M.H., Saitoh, T., Akira, S., Virgin, H.W., and Mizushima, N. (2013). FIP200 regulates targeting of Atg16L1 to the isolation membrane. EMBO Rep. *14*, 284–291.

Noda, N.N., Kumeta, H., Nakatogawa, H., Satoo, K., Adachi, W., Ishii, J., Fujioka, Y., Ohsumi, Y., and Inagaki, F. (2008). Structural basis of target recognition by Atg8/LC3 during selective autophagy. Genes to Cells *13*, 1211–1218.

Novak, I., Kirkin, V., McEwan, D.G., Zhang, J., Wild, P., Rozenknop, A., Rogov, V., Löhr, F., Popovic, D., Occhipinti, A., et al. (2010). Nix is a selective autophagy receptor for mitochondrial clearance. EMBO Rep. *11*, 45–51.

Ogawa, M., Yoshimori, T., Suzuki, T., Sagara, H., Mizushima, N., and Sasakawa, C. (2005). Escape of intracellular Shigella from autophagy. Science (80-.). *307*, 727–731.

Okamoto, K., Kondo-Okamoto, N., and Ohsumi, Y. (2009). Mitochondria-Anchored Receptor Atg32 Mediates Degradation of Mitochondria via Selective Autophagy. Dev. Cell *17*, 87–97.

Okatsu, K., Saisho, K., Shimanuki, M., Nakada, K., Shitara, H., Sou, Y., Kimura, M., Sato, S., Hattori, N., Komatsu, M., et al. (2010). p62/SQSTM1 cooperates with Parkin for perinuclear clustering of depolarized mitochondria. Genes to Cells *15*, 887–900.

Paine, M.G., Babu, J.R., Seibenhener, M.L., and Wooten, M.W. (2005). Evidence for p62 aggregate formation: Role in cell survival. FEBS Lett. *579*, 5029–5034.

Pankiv, S., Clausen, T.H., Lamark, T., Brech, A., Bruun, J.A., Outzen, H., Øvervatn, A., Bjørkøy, G., and Johansen, T. (2007). p62/SQSTM1 binds directly to Atg8/LC3 to facilitate degradation of ubiquitinated protein aggregates by autophagy. J. Biol. Chem. *282*, 24131–24145.

Pankiv, S., Lamark, T., Bruun, J.A., Øvervatn, A., Bjørkøy, G., and Johansen, T. (2010). Nucleocytoplasmic shuttling of p62/SQSTM1 and its role in recruitment of nuclear polyubiquitinated proteins to promyelocytic leukemia bodies. J. Biol. Chem. *285*, 5941–5953.

Papinski, D., and Kraft, C. (2016). Regulation of autophagy by signalling through the Atg1/ULK1 complex. J. Mol. Biol. *428*, 1725–1741.

Papinski, D., Schuschnig, M., Reiter, W., Wilhelm, L., Barnes, C.A., Maiolica, A., Hansmann, I., Pfaffenwimmer, T., Kijanska, M., Stoffel, I., et al. (2014). Early Steps in Autophagy Depend on Direct Phosphorylation of Atg9 by the Atg1 Kinase. Mol. Cell *53*, 471–483.

Pfaffenwimmer, T., Reiter, W., Brach, T., Nogellova, V., Papinski, D., Schuschnig, M., Abert, C., Ammerer, G., Martens, S., and Kraft, C. (2014). Hrr25 kinase promotes selective autophagy by phosphorylating the cargo receptor Atg19. EMBO Rep. *15*, 862–870.

Ragusa, M.J., Stanley, R.E., and Hurley, J.H. (2012). Architecture of the Atg17 complex as a scaffold for autophagosome biogenesis. Cell *151*, 1501–1512.

Rao, Y., Perna, M.G., Hofmann, B., Beier, V., and Wollert, T. (2016). The Atg1-kinase complex tethers Atg9-vesicles to initiate autophagy. Nat. Commun. *7*, 1–13.

Ravenhill, B.J., Boyle, K.B., von Muhlinen, N., Ellison, C.J., Masson, G.R., Otten, E.G., Foeglein, A., Williams, R., and Randow, F. (2019). The Cargo Receptor NDP52 Initiates Selective Autophagy by Recruiting the ULK Complex to Cytosol-Invading Bacteria. Mol. Cell.

Rich, K.A., Burkett, C., and Webster, P. (2003). Cytoplasmic bacteria can be targets for autophagy. Cell. Microbiol. *5*, 455–468.

Roussel, A., Anderson, B.F., Baker, H.M., Fraser, J.D., and Baker, E.N. (1997). Crystal structure of the streptococcal superantigen SPE-C: dimerization and zinc binding suggest a novel mode of interaction with MHC class II molecules. Nat. Struct. Biol. *4*, 635–643.

Rui, Y.N., Xu, Z., Patel, B., Chen, Z., Chen, D., Tito, A., David, G., Sun, Y., Stimming, E.F., Bellen, H.J., et al. (2015). Huntingtin functions as a scaffold for selective macroautophagy. Nat. Cell Biol. *17*, 262–275.

Russell, R.C., Tian, Y., Yuan, H., Park, H.W., Chang, Y.Y., Kim, J., Kim, H., Neufeld, T.P., Dillin, A., and Guan, K.L. (2013). ULK1 induces autophagy by phosphorylating Beclin-1 and activating VPS34 lipid kinase. Nat. Cell Biol. *15*, 741–750.

Sachs, R., Max, K.E.A., Heinemann, U., and Balbach, J. (2012). RNA single strands bind to a conserved surface of the major cold shock protein in crystals and solution. RNA *18*, 65–76.

Samygina, V.R., Popov, A.N., Rodina, E. V., Vorobyeva, N.N., Lamzin, V.S., Polyakov, K.M., Kurilova, S.A., Nazarova, T.I., and Avaeva, S.M. (2001). The structures of Escherichia coli inorganic pyrophosphatase complexed with Ca2+or CaPPi at atomic resolution and their mechanistic implications. J. Mol. Biol. *314*, 633–645.

Sanchez, P., De Carcer, G., Sandoval, I. V, Moscat, J., and Diaz-Meco, M.T. (1998). Localization of Atypical Protein Kinase C Isoforms into Lysosome-Targeted Endosomes through Interaction with p62. Mol. Cell. Biol. *18*, 3069–3080.

Sawa-Makarska, J., Abert, C., Romanov, J., Zens, B., Ibiricu, I., and Martens, S. (2014). Cargo binding to Atg19 unmasks additional Atg8 binding sites to mediate membrane-cargo apposition during selective autophagy. Nat. Cell Biol. *16*, 425–433.

Schindelin, H., Marahiel, M.A., and Heinemann, U. (1993). Universal nucleic acid-binding domain revealed by crystal structure of the B. subtilis major cold-shock protein. Nature *364*, 164–168.

Schneider, C.A., Rasband, W.S., and Eliceiri, K.W. (2012). NIH Image to ImageJ: 25 years of image analysis. Nat. Methods *9*, 671–675.

Seibenhener, M., and Babu, J. (2004). Sequestosome 1 / p62 is a polyubiquitin chain binding protein involved in ubiquitin proteasome degradation. Mol. Cell. Biol. *24*, 8055–8068.

Seidman, C.E., and Struhl, K. (1998). Introduction of plasmid DNA into cells. Curr. Protoc. Protein Sci. *13*, A.4D.1-A.4D.2.

Sekito, T., Kawamata, T., Ichikawa, R., Suzuki, K., and Ohsumi, Y. (2009). Atg17 recruits Atg9 to organize the pre-autophagosomal structure. Genes to Cells *14*, 525–538.

Shintani, T., Huang, W.P., Stromhaug, P.E., and Klionsky, D.J. (2002). Mechanism of cargo selection in the cytoplasm to vacuole targeting pathway. Dev. Cell *3*, 825–837.

Shpilka, T., Weidberg, H., Pietrokovski, S., and Elazar, Z. (2011). Atg8 : an autophagy-related ubiquitin-like protein family. Genome Biol. *12*.

Sievers, F., Wilm, A., Dineen, D., Gibson, T.J., Karplus, K., Li, W., Lopez, R., McWilliam, H., Remmert, M., Söding, J., et al. (2011). Fast, scalable generation of high-quality protein multiple sequence alignments using Clustal Omega. Mol. Syst. Biol. *7*.

Simonsen, A., Lippe, R., Christoforidis, S., Gaullier, J.-M., Brech, A., Callaghan, J., Toh, B.-H., Murphy, C., Zerial, M., and Stenmark, H. (1998). EEA1 links PI(3)K function to Rab5 regulation of endosome fusion. Nature *394*, 494.

Singh, R., and Cuervo, A.M. (2011). Autophagy in the cellular energetic balance. Cell Metab. *13*, 495–504.

Smith, M.D., Harley, M.E., Kemp, A.J., Wills, J., Lee, M., Arends, M., von Kriegsheim, A., Behrends, C., and Wilkinson, S. (2018). CCPG1 is a non-canonical autophagy cargo receptor essential for ER-phagy and pancreatic ER proteostasis. Dev. Cell *44*, 217–232.e11.

Stanley, R.E., Ragusa, M.J., and Hurley, J.H. (2014). The beginning of the end: How scaffolds nucleate autophagosome biogenesis. Trends Cell Biol. *24*, 73–81.

Steinkellner, G., Rader, R., Thallinger, G.G., Kratky, C., and Gruber, K. (2009). VASCo: Computation and visualization of annotated protein surface contacts. BMC Bioinformatics *10*.

Stolz, A., Ernst, A., and Dikic, I. (2014). Cargo recognition and trafficking in selective autophagy. Nat. Cell Biol. *16*, 495–501.

Striegl, H., Roske, Y., Kümmel, D., and Heinemann, U. (2009). Unusual armadillo fold in the human general vesicular transport factor p115. PLoS One *4*, e4656.

Subramani, S., and Malhotra, V. (2013). Non-autophagic roles of autophagy-related proteins. EMBO Rep. *14*, 143–151.

Sun, D., Wu, R., Zheng, J., Li, P., and Yu, L. (2018). Polyubiquitin chain-induced p62 phase separation drives autophagic cargo segregation. Cell Res. *28*, 405–415.

Suzuki, K., Kamada, Y., and Ohsumi, Y. (2002). Studies of cargo delivery to the vacuole mediated by autophagosomes in Saccharomyces cerevisiae. Dev. Cell *3*, 815–824.

Tasaki, T., Sriram, S.M., Park, K.S., and Kwon, Y.T. (2012). The N-End Rule Pathway. Annu. Rev. Biochem. *81*, 261–289.

Till, A., Saito, R., Merkurjev, D., Liu, J.J., Syed, G.H., Kolnik, M., Siddiqui, A., Glas, M., Scheffler, B., Ideker, T., et al. (2015). Evolutionary trends and functional anatomy of the human expanded autophagy network. Autophagy *11*, 1652–1667.

Tsukada, M., and Ohsumi, Y. (1993). Isolation and characterization of autophagy-defective mutants of Saccharomyces cerevisiae. FEBS Lett. *333*, 169–174.

Turco, E., and Martens, S. (2016). Insights into autophagosome biogenesis from in vitro reconstitutions. J. Struct. Biol. *196*, 29–36.

Turco, E., Witt, M., Abert, C., Bock-Bierbaum, T., Su, M.-Y., Trapannone, R., Sztacho, M., Danieli, A., Shi, X., Zaffagnini, G., et al. (2019). FIP200 Claw domain binding to p62 promotes autophagosome formation at ubiquitin condensates. Mol. Cell.

Ueda, H., Abbi, S., Zheng, C., and Guan, J.L. (2000). Suppression of Pyk2 kinase and cellular activities by FIP200. J. Cell Biol. *149*, 423–430.

Umekawa, M., and Klionsky, D.J. (2012). The Cytoplasm-to-Vacuole Targeting Pathway: A Historical Perspective. Int. J. Cell Biol. *2012*, 1–8.

Vargas, J.N.S., Wang, C., Bunker, E., Hao, L., Maric, D., Schiavo, G., Randow, F., and Youle, R.J. (2019). Spatiotemporal Control of ULK1 Activation by NDP52 and TBK1 during Selective Autophagy. Mol. Cell.

Verhoef, L.G., Lindsten, K., Masucci, M.G., and Dantuma, N.P. (2002). Aggregate formation inhibits proteasomal degradation of polyglutamine proteins. Hum. Mol. Genet. *11*, 2689–2700.

Wang, Y., Zhang, N., Zhang, L., Li, R., Fu, W., Ma, K., Li, X., Wang, L., Wang, J., Zhang, H., et al. (2016). Autophagy regulateschromatin ubiquitination in DNA damage response through elimination of SQSTM1/p62. Mol. Cell *63*, 34–48.

Watanabe, R., Chano, T., Inoue, H., Isono, T., Koiwai, O., and Okabe, H. (2005). Rb1cc1 is critical for myoblast differentiation through Rb1 regulation. Virchows Arch. *447*, 643–648.

Wild, P., Farhan, H., McEwan, D.G., Wagner, S., Rogov, V. V., Brady, N.R., Richter, B., Korac, J., Waidmann, O., Choudhary, C., et al. (2011). Phosphorylation of the autophagy receptor optineurin restricts Salmonella growth. Science (80-.). *333*, 228–233.

Wild, P., McEwan, D.G., and Dikic, I. (2014). The LC3 interactome at a glance. J. Cell Sci. *127*, 3–9.

Wilson, M.I., Gill, D.J., Perisic, O., Quinn, M.T., and Williams, R.L. (2003). PB1 domain-mediated heterodimerization in NADPH oxidase and signaling complexes of atypical protein kinase C with Par6 and p62. Mol. Cell *12*, 39–50.

Winn, M.D., Ballard, C.C., Cowtan, K.D., Dodson, E.J., Emsley, P., Evans, P.R., Keegan, R.M., Krissinel, E.B., Leslie, A.G.W., McCoy, A., et al. (2011). Overview of the CCP4 suite and current developments. Acta Crystallogr. Sect. D Biol. Crystallogr. *67*, 235–242.

Wojcik, C., Schroeter, D., Wilk, S., Lamprecht, J., and Paweletz, N. (1996). Ubiquitin-mediated proteolysis centers in HeLa cells: indication from studies of an inhibitor of the chymotrypsin-like activity of the proteasome. Eur J Cell Biol *71*, 311–318.

Woods, A.S., and Ferré, S. (2005). Amazing stability of the arginine-phosphate electrostatic interaction. J. Proteome Res. *4*, 1397–1402.

Wu, H., and Fuxreiter, M. (2016). The Structure and Dynamics of Higher-Order Assemblies: Amyloids, Signalosomes, and Granules. Cell *165*, 1055–1066.

Wurzer, B., Zaffagnini, G., Fracchiolla, D., Turco, E., Abert, C., Romanov, J., and Martens, S. (2015). Oligomerization of p62 allows for selection of ubiquitinated cargo and isolation membrane during selective autophagy. Elife *4*, e08941.

Yamamoto, H., Kakuta, S., Watanabe, T.M., Kitamura, A., Sekito, T., Kondo-Kakuta, C., Ichikawa, R., Kinjo, M., and Ohsumi, Y. (2012). Atg9 vesicles are an important membrane source during early steps of autophagosome formation. J. Cell Biol. *198*, 219–233.

Ying, H., Shen, X., Park, B., and Yue, B.Y.J.T. (2010). Posttranslational modifications, localization, and protein interactions of optineurin, the product of a glaucoma gene. PLoS One *5*.

Yoo, Y.D., Mun, S.R., Ji, C.H., Sung, K.W., Kang, K.Y., Heo, A.J., Lee, S.H., An, J.Y., Hwang, J., Xie, X.-Q., et al. (2018). N-terminal arginylation generates a bimodal degron that modulates autophagic proteolysis. Proc. Natl. Acad. Sci. *115*, e2716–e2724.

Yorimitsu, T., and Klionsky, D.J. (2005). Atg11 links cargo to the vesicle-forming machinery in the cytoplasm to vacuole targeting pathway. Mol. Biol. Cell *16*, 1593–1605.

Zaffagnini, G., Savova, A., Danieli, A., Romanov, J., Tremel, S., Ebner, M., Peterbauer, T., Sztacho, M., Trapannone, R., Tarafder, A.K., et al. (2018). p62 filaments capture and present ubiquitinated cargos for autophagy. EMBO J. e98308.

Zeeb, M., Max, K.E.A., Weininger, U., Löw, C., Sticht, H., and Balbach, J. (2006). Recognition of T-rich single-stranded DNA by the cold shock protein Bs-CspB in solution. Nucleic Acids Res. *34*, 4561–4571.

Zhang, Y., Mun, S.R., Linares, J.F., Ahn, J., Towers, C.G., Ji, C.H., Fitzwalter, B.E., Holden, M.R., Mi, W., Shi, X., et al. (2018). ZZ-dependent regulation of p62/SQSTM1 in autophagy. Nat. Commun. *9*, 4373.

Zhou, J., Wang, J., Cheng, Y., Chi, Y.J., Fan, B., Yu, J.Q., and Chen, Z. (2013). NBR1-mediated selective autophagy targets insoluble ubiquitinated protein aggregates in plant stress responses. PLoS Genet. *9*, e1003196.

IV. Appendix

Appendix A – Constructs

List of constructs*, except fusion constructs

protein	construct name	boundaries	mutation	vector	comment
FIP200	FIP200 CTR	1458 - 1594	wt	pETDuet1	from S. Martens
(Q8TDY2)	putative p62 binding mutants	1458 -1594	N1517A	pETDuet1	from S. Martens
		1458 -1594	N1517F	pETDuet1	from S. Martens
		1458 -1594	S1532A	pETDuet1	from S. Martens
		1458 -1594	L1535A	pETDuet1	from S. Martens
		1458 -1594	L1535F	pETDuet1	from S. Martens
		1458 -1594	R1573D	pETDuet1	from S. Martens
		1458 -1594	F1574A	pETDuet1	from S. Martens
		1458 -1594	F1574W	pETDuet1	from S. Martens
		1458 -1594	R1584D	pETDuet1	from S. Martens
	putative lipid binding mutants	1458 -1594	K1575D	pETDuet1	
		1458 -1594	K1541D	pETDuet1	
		1458 -1594	R1514D	pETDuet1	
		1458 -1594	R1551D	pETDuet1	
		1458 -1594	R1514D/H1515A	pETDuet1	
		1458 -1594	R1573D	pETDuet1	
	dimer interface mutant	1458 -1594	L1476S/I1496S/ F1521S/W1554S	pETDuet1	
	FIP200 Claw	1494 -1594	wt	pSKB_LNB	
		1494 -1594	R1573D	pSKB_LNB	
	GFP-FIP200 CTR	1458 - 1594	wt	pETDuet1	from S. Martens, N-term. GFP tag
p62	p62 FIR	326-380	wt	pGEX4-T3	from S. Martens
(Q13501)	p62 FIR LIRmut	326-380	335-338 > AAAA	pGEX4-T3	from S. Martens
	p62 FIR 1P	326-380	S349D	pGEX4-T3	from S. Martens
	p62 FIR 3P	326-380	S365D/366D/370D	pGEX4-T3	from S. Martens
	p62 FIR 4P	326-380	S349D/S365D/ S366D/S370D	pGEX4-T3	from S. Martens

*For constructs used in cell biology please refer to Section 3.5.

List of fusion constructs for FIP200 – p62 complex crystallization

construct name	boundaries FIP200 (Q8TDY2)	boundaries p62 (Q13501)	FIP 200 location	linker length	vector
FIPCTR-L2-p62FIR	1458 -1590	326-380	N-terminal	2	pSKB_LNB
FIPCTR-L4-p62FIR	1458 -1590	326-380	N-terminal	4	pSKB_LNB
FIPCTR-L8-p62FIR	1458 -1590	326-380	N-terminal	8	pSKB_LNB
p62FIR-L2-FIPCTR	1458 -1594	326-373	C-terminal	2	pSKB_LNB
p62FIR-L6-FIPCTR	1458-1594	326-373	C-terminal	6	pSKB_LNB
p62FIR-L12-FIPCTR	1458-1594	326-373	C-terminal	12	pSKB_LNB
FIPclaw-L4-p62*4D	1494-1594	332-372	N-terminal	4	pSKB_LNB
FIPclaw-L8-p62*4D	1494-1594	332-372	N-terminal	8	pSKB_LNB
FIPclaw-L4-p62*1D	1494-1594	332-357	N-terminal	4	pSKB_LNB
FIPclaw-L8-p62*1D	1494-1594	332-357	N-terminal	8	pSKB_LNB
p62*D4-L4-FIPclaw	1494-1594	332-372	C-terminal	4	pSKB_LNB
p62*D4-L8-FIPclaw	1494-1594	332-372	C-terminal	8	pSKB_LNB
p62*D1-L4-FIPclaw	1494-1594	332-357	C-terminal	4	pSKB_LNB
p62*D1-L8-FIPclaw	1494-1594	332-357	C-terminal	8	pSKB_LNB

Appendix B – Sequence alignment

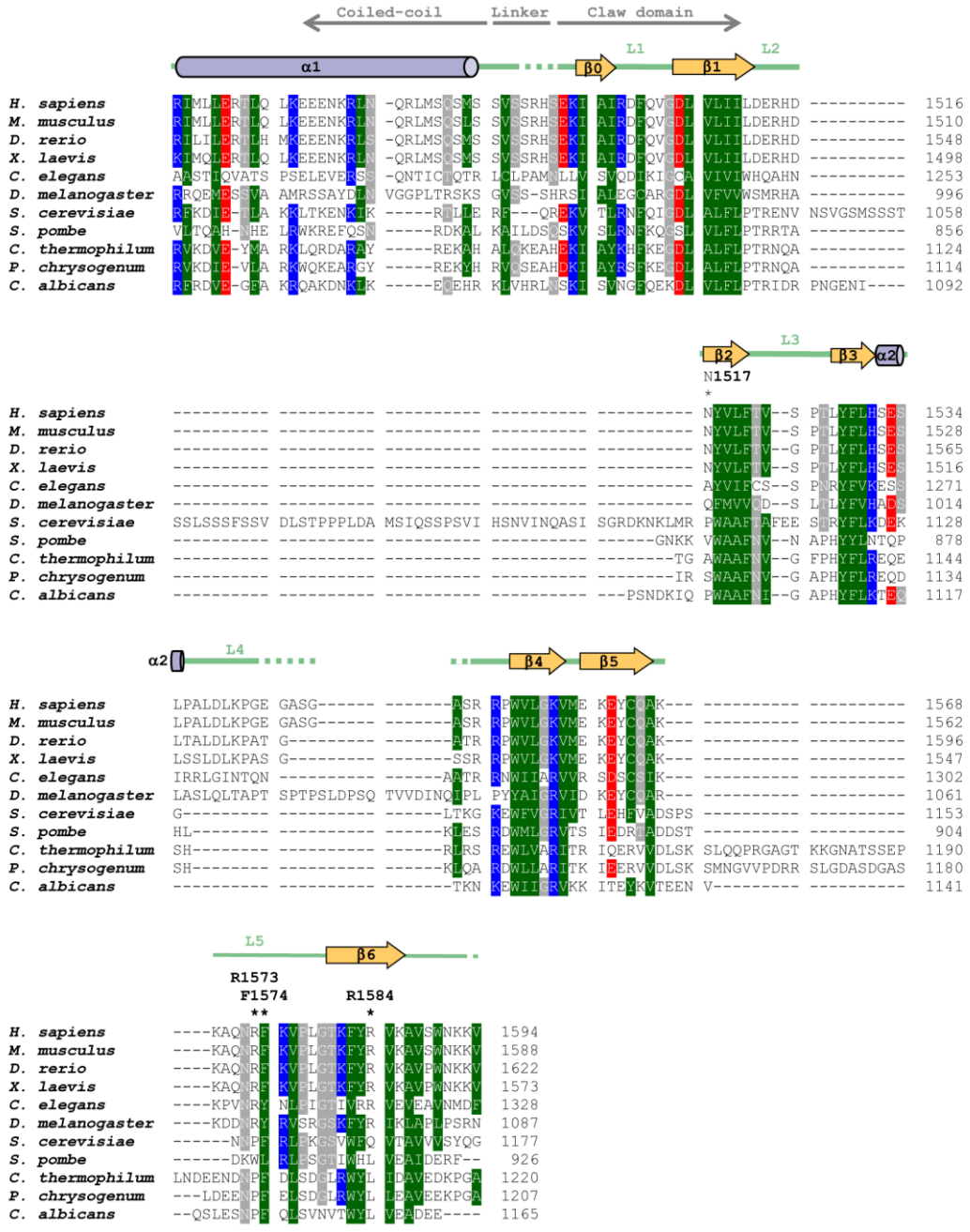

Figure 38. Sequence alignment of the following Atg11 homology regions from different species (UniProt accession code in parentheses). *H. sapiens* (Q8TDY2), *M. musculus*, (Q9ESK9), *D. rerio*, (E7FFM2), *X. laevis* (A0A1L8FYZ6), *C. elegans* (Q22342), *D. melanogaster* (Q7KTS2), *S. cerevisiae* (Q12527), *S. pombe* (O14261), *C. thermophilum*, (G0S0K0), *P. chrysogenum* (A0A167XQU9), *C. albicans* (Q5AMN3). Residues with a conservation greater than 60% are color-coded (D, E in red; R, K, H in blue N, Q, S, T, G, P in gray; A, L, I, V, F, Y, W, M, C in green). FIP200 CTR secondary structure is displayed on top of the alignment. α-helices are shown as cylinders and β-strands as arrows. Mutated residues in this study are indicated with an asterisk (*).

Appendix C - Instruments

Instrument	Manufacturer
Hampton VDX greased plates, 24-well	Hampton Research
CrystalQuick plates, 96-well	Greiner Bio-One
Agarose Gel Electrophoresis System	OLS
Amicon centrifugal filter device	Merck
Rock Imager storage system	Formulatrix
Biacore T200	GE Healthcare
BioPhotometer	Eppendorf
Centrifuge 5415 R (benchtop)	Eppendorf
Centrifuge 5810 R (benchtop)	Eppendorf
Centrifuge 5424 R (benchtop)	Eppendorf
HLC Cooling-Thermomixer MKR13	Ditabis
Centrifuge Avanti J-26 XP	Beckman Coulter
Chromatography columns Superdex200 16/600, 26/600	GE Healthcare
Chromatography columns Superdex75 16/600, 26/600	GE Healthcare
Cryo-Fridge VIP Series -86°C	Sanyo
CryoLoops, various sizes	Hampton Research
Fluidizer M-110 L Pneumatic	Microfluidics
FPLC Äkta Prime Plus / Purifier	GE Healthcare
Imaging system LAS4000 mini	FujiFilm
Imaging system GelDoc XR+	Bio-Rad
Isothermal Titration Calorimeter MicroCal peaqITC / ITC_{200} / VP-ITC	Malvern Panalytical
Rotor type 45 Ti	Beckman Coulter
Rotor type JA 25.50	Beckman Coulter
Rotor type JLA 8.100	Beckman Coulter
Rotor type TLA 100	Beckman Coulter
Halogen light source KL2500 LCD	Schott
Microscope Leica MZ75	Leica
Microscope LSM700 confocal	Zeiss
Microscope Visitron spinning disk	Visitron Systems
Milli-Q reference system	Merck
NanoDrop 2000	Thermo Scientific
NanoDrop One	Thermo Scientific
Optima MAX-XP ultracentrifuge (benchtop)	Beckman Coulter
Thermocycler C1000 Touch	Bio-Rad
Peptide Spotter Intavis ResPep-SL	Intavis, Bioanalytical Instruments
Peristaltic pump ISM 827 B	Ismatec
pH-Meter Seven Compact	Mettler-Toledo
Pilatus 6M detector	Dectris

Pipettes Eppendorf Research vario	Eppendorf
Pipetting robot Gryphon	Art Robins Instruments
Precision scales	Sartorius
RALS 270 dual detector	Malvern Panalytical
Refractive index detector VE 3580	Malvern Panalytical
SDS PAGE System Xcell Sure Lock	Life Techologies
Shaker Incubator Innova 44 R	New Brunswick Scientific
Shaker Incubator Excella E24	New Brunswick Scientific
Ultracentrifuge Optima L-100 K	Beckman Coulter
Vacuum pump	Vacuubrand

Appendix D - Chemicals

Chemical	**Manufacturer**	**Cat. No.**
2-propanol	Roth	9866.5
acetic acid	Roth	3783.5
AEBSF hydrochlorid	PanReacAppliChem	A1421
agarose	Serva	11404
ammonium chloride	Sigma-Aldrich	31107
ampicillin	Roth	K029.2
brain extract from bovine brain, Type 1, Folch Fraction 1	Sigma-Aldrich	B1502
brilliant blue R250	Roth	3862.2
calcium chloride ($CaCl_2$)	Fluka	21097
chloramphenicol	Roth	3886.3
chloroform	Honeywell	C2432
DTT	Roth	6908.2
ethanol Rotipuran	Roth	6065.4
ethidium bromide	Roth	2218.2
glutathione sepharose 4B	VWR	6382.2
glutathione, reduced	Roth	6382.2
glycerol	Roth	3790.3
glycine	Roth	3790.3
guanidine hydrochloride	Roth	0037.1
HEPES	Roth	9105.3
imidazole	Roth	3899.3
IPTG	Roth	CN08.3
isoleucine	Sigma-Aldrich	I2752
kanamycinsulfate	Roth	T832.2

leucine	Sigma-Aldrich	61819
lithium chloride (LiCl)	Sigma-Aldrich	62476
lysine	Sigma-Aldrich	62840
magnesium chloride	Sigma-Aldrich	M2670
MES buffer	Sigma-Aldrich	69892
methanol	Honeywell	41467
PEG 6000	Sigma-Aldrich	81255
phenylalanine	Sigma-Aldrich	78019
phytic acid sodium salt hydrate (IP_6)	Sigma-Aldrich	P8810
potassium chloride	Roth	6781.3
reduced glutathione	Roth	6382.2
seleno-L-methionine	Merck	561505
Series S Sensor Chip CM5	GE Healthcare	BR100530
skim milk powder	Sigma-Aldrich	70166
sodium acetate	Sigma-Aldrich	71188
sodium chloride	Roth	HN00.3
TB medium	Melford	T1702
threonine	Sigma-Aldrich	89180
Tris HCl	Roth	5429.2
Tween20	Roth	9127.1
valine	Sigma-Aldrich	94620

Appendix E - Abbreviations

aa	amino acids
AEBSF	4-(2-aminoethyl)benzenesulfonyl fluoride hydrochloride
AIM	Atg8-interacting motif
Atg	autophagy related gene
Atg16L1	Atg16-like 1
ATP	adenosine triphosphate
BESSY	Berliner Elektronenspeicherring-Gesellschaft für Synchrotronstrahlung
Cas9	CRISPR-associated protein 9
CCPG1	protein cell-cycle progression gene 1
CIP	alkaline phosphatase, calf intestinal
CRISPR	clustered regularly interspaced short palindromic repeats
CSD	cold shock domains
CTR	C-terminal region
CV	column volume
Cvt	cytoplasm to vacuole
DNA	Deoxyribonucleic acid
dT_6	hexathymidine
DTT	dithiothreitol
EAT	early autophagy targeting/tethering
EEA1	early endosome antigen 1
EM	electron microscopy
ER	endoplasmic reticulum
ERK1	mitogen-activated protein kinase 3
FAM134B	family with sequence similarity 134 member B
FIP200	FAK family kinase-interacting protein of 200 kDa
FIR	FIP200 interacting region
FUNDC1	FUN14 Domain Containing 1
FYVE	**F**ab 1, **Y**OTB, **V**ac 1, **E**EA1
GABARAP	γ-amino-butyric acid receptor-associate protein
GATE-16	Golgi-associated ATPase enhancer of 16 kDa
GFP	green fluorescent protein
GST	glutathione S-transferase
GUV	giant unilammelar vesicles
HA-tag	human influenza hemagglutinin tag
HEPES	4-(2-hydroxyethyl)-1-piperazineethanesulfonic acid
IP_6	inositol hexaphosphate
IPTG	isopropyl-ß-D-1-thiogalactopyranoside
ITC	isothermal titration calorimetry
K_D	dissociation constant
$K_D$app	apparent dissociation constant
KIR	Keap1 interacting region

LB	Luria-Bertani
LC3B	microtubule-associated protein 1 light chain 3 B
LIR	LC3-interactiong region
MAP1LC3	microtubule-associated protein 1 light chain 3
MEK5	MAP kinase kinase
MES	2-(N-morpholino)ethanesulfonic acid
MFPL	Max F. Perutz Laboratories
mTORC1	mammalian target of rapamycin complex 1
NBR1	neighbor of BRCA1 gene 1 protein
NCS	non-crystallographic symmetry
NDP52	nuclear dot protein 52
NF-κB	nuclear factor kappa-light-chain-enhancer of activated B cells
Ni-NTA	nickel - nitrilotriacetic acid
NIX	NIP3-like protein X
NMR	nuclear magnetic resonance
Nrf2	nuclear factor (erythroid-derived 2)-like 2
OB-fold	oligonucleotide/oligosaccharide binding fold
OD_{600}	optical density at 600 nm
OPTN	optineurin
p115	general vesicular transport factor p115
p62 FIR	p62 FIP200 interacting region
PAS	phagophore assembly site
PB1	Phox and Bem1p domain
PDB	protein data bank
PE	phosphatidylethanolamine
pI	isoelectric point
PI	phosphatidylinositol
PI(3)P	phosphatidylinositol 3-phosphate
PI3K	class III phosphatidylinositol 3-kinase complex
PKCζ	proteinkinase Cζ
PNK	T4 polynucleotide kinase
PS	phosphatidylserine
PVDF	polyvinylidene fluoride
Rab1	Ras-related protein Rab-1
RALS	right-Angle Light Scattering
RB1CC1	RB1-inducible coiled-coil protein 1
R_{max}	fitted maximal binding capacity
RMSD	root mean square deviation
RNA	ribonucleic acid
RU	response Units
SAD	single-wavelength anomalous diffraction
SDS-PAGE	sodium dodecyl sulfate–polyacrylamide gel electrophoresis
SEC	size exclusion chromatography
SEC-RALS	size exclusion chromatography coupled to right angle light scattering

SEM	standard error of the mean
Se-Met	seleno-L-methionine
SNARE	soluble N-ethylmaleimide sensitive fusion proteins attachment protein receptor
SPR	surface plasmon resonance spectroscopy
SQSTM1	sequestosome 1
STG tag	strep-TEV-GFP tag
TB	terrific Broth
TBK1	TANK-binding kinase 1
TBS	tris-buffered saline
TBS-T	tris-buffered saline with tween
TEV	tobacco etch virus protease
TLS	translation-libration-screw-rotation
TRAF6	TNF receptor associated factor 6
UBA	ubiquitin-binding domain
Vam7	vacuolar morphogenesis protein 7
wt	wildtype
Ypt1	GTP-binding protein YPT1
ZZ	ZZ-type zinc-finger domain

Amino acid abbreviations

one letter code	three letter code	amino acid
A	Ala	alanine
C	Cys	cysteine
D	Asp	aspartate
E	Glu	glutamate
F	Phe	phenylalanine
G	Gly	glycine
H	His	histidine
I	Ile	isoleucine
K	Lys	lysine
L	Leu	leucine
M	Met	methionine
N	Asn	asparagine
P	Pro	proline
Q	Gln	glutamine
R	Arg	arginine
S	Ser	serine
T	Thr	threonine
V	Val	valine
W	Trp	tryptophane
Y	Tyr	tyrosine

V. Acknowledgement

I would like to thank Oliver Daumke for outstanding supervision. His positive and open mindset and his availability for discussions have been making it a pleasure to work together.

Thanks to Sascha Martens, Eleonora Turco and Christine Abert for this wonderful and productive collaboration, especially for all their work regarding the publication.

I am very grateful to Tobias Bock, who took a major part in solving the FIP200 CTR structure. He was exceptionally helpful in the laboratory, always available for discussion and eager to solve (other people's) problems.

Thanks to Oren Moscovitz, Paulina Kaplonek and Amit Koikkarah (MPI for Colloids and Interfaces) for measuring time on the Biacore T200, for technical support and hosting me in their lab for more than one month. Thanks to Enno Klussmann and Kerstin Zühlke (MDC) who provided the peptide SPOT array. Thanks to Manfred Weiss and his colleagues for help and support during data collection experiments at BESSY II electron storage ring. Thanks to Yvette Roske and Katja Fälber for data collection when I was hindered due to pregnancy and for advice on structure determination. Many thanks to Yvette for taking excellent care of the crystallization equipment.

Thanks goes to all former and current members of the Daumke and Heinemann laboratories for advice, protocols, discussions, distractions and laughs. I particularly thank Arthur Melo and Vivian Schulz for creating an open, respectful and happy atmosphere in the lab that carried me through a difficult first year. Also, I would like to thank Carolin Bernert, Franziska Bartelt, Vivian Schulz, Jeanette Schlegel and Sabine Werner for excellent technical support during my PhD. I especially appreciate all the little things they have done on a day to day basis, trying to provide the best working environment for us.

Thanks to my parents for love and encouragement, and particularly to my mum for countless hours of babysitting. Finally, thanks to Paul and Chris for their unconditional love and support.

VI. Erklärung

Ich versichere, dass ich die von mir vorgelegte Dissertation selbstständig angefertigt, die benutzten Quellen und Hilfsmittel vollständig angegeben und die Stellen der Arbeit – einschließlich Tabellen, Karten und Abbildungen – die anderen Werken im Wortlaut oder dem Sinn nach entnommen sind, in jedem Einzelfall als Entlehnung kenntlich gemacht habe; und dass diese Dissertation noch keiner anderen Fakultät oder Universität zur Prüfung vorgelegen hat. Die Bestimmungen der Promotionsordnung sind mir bekannt. Die von mir vorgelegte Dissertation ist von Prof. Dr. Oliver Daumke und Prof. Dr. Udo Heinemann betreut worden.

Berlin, März 2019

Marie Witt